Vol. 3

AIIMS-MAMC-PGI's Comprehensive Textbook of DIAGNOSTIC RADIOLOGY

Volume 3

Vol. 2

AIIMS-MAMC-PGI's Comprehensive Textbook of DIAGNOSTIC RADIOLOGY

Volume 2

Vol. 1

AIIMS-MAMC-PGI's Comprehensive Textbook of DIAGNOSTIC RADIOLOGY

Khandelwal
Chowdhury
Gupta

Volume 1

AIIMS-MAMC-PGI's Comprehensive Textbook of DIAGNOSTIC RADIOLOGY

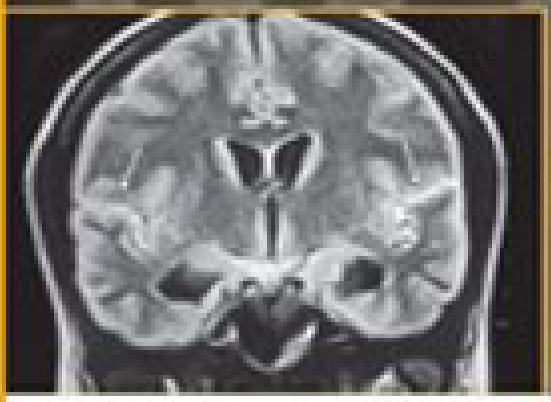

Neuroradiology

Head and Neck

Advances & Applied Physics in Imaging

Niranjan Khandelwal
Veena Chowdhury
Arun Kumar Gupta

AIIMS-MAMC-PGI's
Comprehensive Textbook of

Diagnostic Radiology

AIIMS-MAMC-PGI's Comprehensive Textbook of Diagnostic Radiology

3 VOLUMES

Editors

Niranjan Khandelwal
MD Dip NBE FICR FAMS
Professor and Head
Department of Radiodiagnosis
Postgraduate Institute of Medical Education and Research
Chandigarh, India

Veena Chowdhury
MBBS MD
Professor of Excellence
Department of Radiodiagnosis
Maulana Azad Medical College, New Delhi, India

Arun Kumar Gupta
MD FAMS
Professor and Head
Department of Radiodiagnosis
All India Institute of Medical Sciences, New Delhi, India

The Health Sciences Publisher
New Delhi | London | Philadelphia | Panama

Jaypee Brothers Medical Publishers (P) Ltd.

Headquarters

Jaypee Brothers Medical Publishers (P) Ltd.
4838/24, Ansari Road, Daryaganj
New Delhi 110 002, India
Phone: +91-11-43574357
Fax: +91-11-43574314
E-mail: jaypee@jaypeebrothers.com

Overseas Offices

J.P. Medical Ltd.
83, Victoria Street, London
SW1H 0HW (UK)
Phone: +44-20 3170 8910
Fax: +44(0) 20 3008 6180
E-mail: info@jpmedpub.com

Jaypee Highlights Medical Publishers Inc.
City of Knowledge, Building 235, 2nd Floor
Clayton, Panama City, Panama
Phone: +1 507-301-0496
Fax: +1 507-301-0499
E-mail: cservice@jphmedical.com

Jaypee Medical Inc.
325, Chestnut Street
Suite 412, Philadelphia, PA 19106, USA
Phone: +1 267-519-9789
E-mail: support@jpmedus.com

Jaypee Brothers Medical Publishers (P) Ltd.
17/1-B, Babar Road, Block-B
Shaymali, Mohammadpur
Dhaka-1207, Bangladesh
Mobile: +08801912003485
E-mail: jaypeedhaka@gmail.com

Jaypee Brothers Medical Publishers (P) Ltd.
Bhotahity
Kathmandu, Nepal
Phone: +977-9741283608
E-mail: kathmandu@jaypeebrothers.com

Website: www.jaypeebrothers.com Website:
www.jaypeedigital.com

AIIMS-MAMC-PGI's Comprehensive Textbook of Diagnostic Radiology

First Edition: **Digital Version 2017**

ISBN 978-93-5250-187-8

Dedicated to

THE SUPREME BEING
Who so mercifully helps us to accomplish gigantic tasks
so smoothly, effortlessly and so beautifully

Contributors

Ajay Garg MD
Professor
Department of Neuroradiology
All India Institute of Medical Sciences
New Delhi, India

Ajay Gulati MD
Associate Professor
Department of Radiodiagnosis
Postgraduate Institute of Medical
Education and Research
Chandigarh, India

Ajay Kumar MD
Additional Professor
Department of Radiodiagnosis
Postgraduate Institute of Medical
Education and Research
Chandigarh, India

Akshay Kumar Saxena MD Dip NBE
Professor
Department of Radiodiagnosis
Postgraduate Institute of Medical
Education and Research
Chandigarh, India

Alpana Manchanda MBBS MD
Professor
Department of Radiodiagnosis
Maulana Azad Medical College
New Delhi, India

Amar Mukund MD
Associate Professor
Department of Radiodiagnosis
Institute of Liver and Biliary
Sciences (ILBS)
New Delhi, India

Anil Chauhan MBBS Board Certified in Radiology USA
Fellow, Body Imaging
Department of Radiology
University of Texas MD Anderson
Cancer Center
Houston, USA

Anil K Pandey PhD
Assistant Professor (Medical Physics)
Department of Nuclear Medicine
All India Institute of Medical Sciences
New Delhi, India

Anindita Sinha MD
Associate Professor
Department of Radiodiagnosis
Postgraduate Institute of Medical
Education and Research
Chandigarh, India

Anish Bhattacharya DNB DRM MNAMS
Professor
Department of Nuclear Medicine
Postgraduate Institute of Medical
Education and Research
Chandigarh, India

Anjali Prakash MBBS DMRD DNB
Professor
Department of Radiodiagnosis
Maulana Azad Medical College
New Delhi, India

Anju Garg MBBS MD
Director Professor
Department of Radiodiagnosis
Maulana Azad Medical College
New Delhi, India

Ankur Gadodia MD DNB FRCR
Consultant
Goyal MRI and Diagnostic Centre
New Delhi, India

Anupam Lal MD
Professor
Department of Radiodiagnosis
Postgraduate Institute of Medical
Education and Research
Chandigarh, India

Arun Deep Arora MD
Former Senior Research Associate
Department of Radiodiagnosis
All India Institute of Medical Sciences
New Delhi, India

Arun Kumar Gupta MD FAMS
Professor and Head
Department of Radiodiagnosis
All India Institute of Medical Sciences
New Delhi, India

Arun Malhotra DRM PhD
Former Professor and Head
Department of Nuclear Medicine
All India Institute of Medical Sciences
New Delhi, India

Ashu Seith Bhalla MD MAMS FICR
Professor
Department of Radiodiagnosis
All India Institute of Medical Sciences
New Delhi, India

Atin Kumar MD MNAMS DNB
Additional Professor
Department of Radiodiagnosis
Trauma Centre
All India Institute of Medical Sciences
New Delhi, India

Birinder Nagi MD MNAMS
Ex-Professor (Section of Radiology)
Department of Gastroenterology
Postgraduate Institute of Medical
Education and Research
Chandigarh, India

BR Mittal MD DRM DNB FIC NM FAMS
Professor and Head
Department of Nuclear Medicine
Postgraduate Institute of Medical
Education and Research
Chandigarh, India

Chandan Jyoti Das MD DNB MNAMS
Assistant Professor
Department of Radiodiagnosis
All India Institute of Medical Sciences
New Delhi, India

Chandrashekhara SH MD DNB MNAMS
Assistant Professor
Department of Radiodiagnosis
(BRAIRCH Division)
All India Institute of Medical Sciences
New Delhi, India

Chetan D Patel MBBS DRM DNB
Professor
Department of Nuclear Medicine
All India Institute of Medical Sciences
New Delhi, India

Deep N Srivastava MD FAMS
Professor
Department of Radiodiagnosis
All India Institute of Medical Sciences
New Delhi, India

Devasenathipathy Kandasamy MD DNB FRCR
Assistant Professor
Department of Radiodiagnosis
All India Institute of Medical Sciences
New Delhi, India

Gaurav S Pradhan MBBS DMRD DNB
Director Professor
Department of Radiodiagnosis
Maulana Azad Medical College
New Delhi, India

Gurpreet Singh Gulati MD
Professor
Department of Cardiac Radiology
Cardio-Thoracic Centre
All India Institute of Medical Sciences
Ansari Nagar, New Delhi, India

Harsh Kandpal
Former Pool Officer
Department of Radiodiagnosis
All India Institute of Medical Sciences
New Delhi, India

Hina Arif Mumtaz MD DNB
Senior Research Associate
Department of Radiodiagnosis
Postgraduate Institute of Medical
Education and Research
Chandigarh, India

Jyoti Kumar MBBS MD DNB MNAMS
Professor
Department of Radiodiagnosis
Maulana Azad Medical College
New Delhi, India

Kirti Gupta MD
Additional Professor
Department of Histopathology
Postgraduate Institute of Medical
Education and Research
Chandigarh, India

Kushaljit Singh Sodhi MD MNAMS FICR
Additional Professor
Department of Radiodiagnosis
Postgraduate Institute of Medical
Education and Research
Chandigarh, India

Kusum Joshi MD PhD
Professor and Ex-Head
Department of Histopathology
Postgraduate Institute of Medical
Education and Research
Chandigarh, India

Madhavi Chawla
Consultant
Max Hospital, Saket
New Delhi, India

Madhu Gulati MD
Ex-Additional Professor
Department of Radiodiagnosis
Postgraduate Institute of Medical
Education and Research
Chandigarh, India

Madhusudhan KS MD MAMS FRCR
Assistant Professor
Department of Radiodiagnosis
All India Institute of Medical Sciences
New Delhi, India

Mahesh Prakash MD FICR
Additional Professor
Department of Radiodiagnosis
Postgraduate Institute of Medical
Education and Research
Chandigarh, India

Manavjit Singh Sandhu MD FICR
Professor
Department of Radiodiagnosis
Postgraduate Institute of Medical
Education and Research
Chandigarh, India

Mandeep Kang MD DNB MAMS FICR
Professor
Department of Radiodiagnosis
Postgraduate Institute of Medical
Education and Research
Chandigarh, India

Mandeep Kumar Garg MD FRCR
Additional Professor
Department of Radiodiagnosis
Postgraduate Institute of Medical
Education and Research
Chandigarh, India

Manisha Jana MD DNB FRCR
Assistant Professor
Department of Radiodiagnosis
All India Institute of Medical Sciences
New Delhi, India

Manish Modi MD
Additional Professor
Department of Neurology
Postgraduate Institute of Medical
Education and Research
Chandigarh, India

Manphool Singhal MD DNB MNAMS
Associate Professor
Department of Radiodiagnosis
Postgraduate Institute of Medical
Education and Research
Chandigarh, India

Mukesh Kumar Yadav MD
Assistant Professor
Department of Radiodiagnosis (BRAIRCH)
All India Institute of Medical Sciences
New Delhi, India

Naveen Kalra MD MAMS FICR
Professor
Department of Radiodiagnosis
Postgraduate Institute of Medical
Education and Research
Chandigarh, India

Niranjan Khandelwal MD DNB NBE FICR FAMS
Professor and Head
Department of Radiodiagnosis
Postgraduate Institute of Medical
Education and Research
Chandigarh, India

NK Mishra MD
Professor and Head
Department of Neuroradiology
All India Institute of Medical Sciences
Ansari Nagar, New Delhi, India

Paramjeet Singh MD
Professor
Department of Radiodiagnosis
Postgraduate Institute of Medical
Education and Research
Chandigarh, India

Pratik Kumar PhD DABMP
Professor
Medical Physics Unit (BRAIRCH)
All India Institute of Medical Sciences
New Delhi, India

Priya Jagia MD DNB
Professor
Department of Cardiac Radiology
Cardio-Thoracic Centre
All India Institute of Medical Sciences
New Delhi, India

Punit Sharma MD
Former Senior Resident
Department of Nuclear Medicine
All India Institute of Medical Sciences
New Delhi, India

Radhika Srinivasan MD PhD
Professor
Department of Cytology and Gynaec-pathology
Postgraduate Institute of Medical Education and Research
Chandigarh, India

Rajat Jain MD
Senior Resident
Department of Radiodiagnosis
Maulana Azad Medical College
New Delhi, India

Raju Sharma MD MAMS
Professor
Department of Radiodiagnosis
All India Institute of Medical Sciences
New Delhi, India

Rakesh Kumar MD PhD
Professor
Department of Nuclear Medicine
All India Institute of Medical Sciences
New Delhi, India

Rakesh Kumar Vasishta MD
Professor and Head
Department of Histopathology
Postgraduate Institute of Medical Education and Research
Chandigarh, India

Rama Mohan Reddy MD (Nuclear Medicine)
Former Senior Resident
Department of Nuclear Medicine
All India Institute of Medical Sciences
New Delhi, India

Rashmi Dixit MBBS MD
Professor
Department of Radiodiagnosis
Maulana Azad Medical College
New Delhi, India

Sameer Vyas MD
Associate Professor
Department of Radiodiagnosis
Postgraduate Institute of Medical Education and Research
Chandigarh, India

Sanjay Sharma MD DNB FRCR
Professor
Department of Radiodiagnosis (RPC Division)
All India Institute of Medical Sciences
New Delhi, India

Sanjay Thulkar MD
Professor
Department of Radiodiagnosis (BRAIRCH)
All India Institute of Medical Sciences
New Delhi, India

Sanjiv Sharma MD
Professor and Head
Department of Cardiac Radiology
Cardio-Thoracic Centre
All India Institute of Medical Sciences
New Delhi, India

Sapna Singh MBBS MD DNB MNAMS
Professor
Department of Radiodiagnosis
Maulana Azad Medical College
New Delhi, India

SC Bansal MA MSc PhD
Lecturer
Department of Radiodiagnosis
Postgraduate Institute of Medical Education and Research
Chandigarh, India

Shailesh B Gaikwad MD
Professor
Department of Neuroradiology
All India Institute of Medical Sciences
New Delhi, India

Shamim Ahmed Shamim MD (Nuclear Medicine)
Assistant Professor
Department of Nuclear Medicine
All India Institute of Medical Sciences
New Delhi, India

Shashi Bala Paul PhD MAMS
Senior Scientist
Department of Radiodiagnosis
All India Institute of Medical Sciences
New Delhi, India

Shivanand Gamanagatti MD MAMS
Additional Professor
Department of Radiodiagnosis
Trauma Centre
All India Institute of Medical Sciences
New Delhi, India

Smriti Hari MD MAMS
Additional Professor
Department of Radiodiagnosis
All India Institute of Medical Sciences
New Delhi, India

Subrat Kumar Acharya
Professor and Head
Department of Gastroenterology
All India Institute of Medical Sciences
New Delhi, India

Sudesh Prabhakar
Ex-Professor and Head
Department of Neurology
Postgraduate Institute of Medical Education and Research
Chandigarh, India

Sudha Suri MD FAMS FICS
Emeritus Professor and Former Head and Dean
Department of Radiodiagnosis
Postgraduate Institute of Medical Education and Research
Chandigarh, India

Sumedha Pawa MBBS MD
Director Professor
Department of Radiodiagnosis
Maulana Azad Medical College
New Delhi, India

Surabhi Vyas MD
Assistant Professor
Department of Radiodiagnosis
All India Institute of Medical Sciences
New Delhi, India

Tulika Singh MD
Associate Professor
Department of Radiodiagnosis
Postgraduate Institute of Medical Education and Research
Chandigarh, India

Veena Chowdhury MBBS MD
Professor of Excellence
Department of Radiodiagnosis
Maulana Azad Medical College
New Delhi, India

Veenu Singla MD
Additional Professor
Department of Radiodiagnosis
Postgraduate Institute of Medical Education and Research
Chandigarh, India

Vivek Gupta MD DM (Neuroradiology)
Additional Professor
Department of Radiodiagnosis
Postgraduate Institute of Medical Education and Research
Chandigarh, India

Preface

In 1996, a unique venture was jointly initiated by the faculty of radiodiagnosis at All India Institute of Medical Sciences, Maulana Azad Medical College, New Delhi, and Postgraduate Institute of Medical Education and Research, Chandigarh, India, to organize continuing medical education programs based on a series of imaging courses. An integral part of this endeavor was publishing books covering all organ systems. The aim was to provide state of the art knowledge for postgraduate students as well as the practicing radiologists along with establishing a uniform pattern of teaching in radiology across the country.

The first series of seven imaging courses was successfully completed in the year 2000. A second series of these courses was then initiated in the year 2002 and was completed in 2004. This was also highly successful.

With the great success of the second series, we, the current editors, decided to start a third series of these courses in 2008. Seven extremely popular and successful courses covering all the organ systems and advances in physics were completed in 2013.

Every course in each of the three series have resulted in publication of a book. These books have been very popular amongst residents as well as among practicing radiologists.

Considering the popularity of these books, we, the three current editors, along with publishers M/s Jaypee Brothers Medical Publishers (P) Ltd., decided to combine the individual books published so far into a *AIIMS-MAMC-PGI's Comprehensive Textbook of Diagnostic Radiology* with three volumes.

We are very happy to see the end result of this great effort.

We are sure that residents and radiologists will find these comprehensive three volumes easy to handle and very useful in day-to-day practice.

We are once again grateful to all the contributors from the three apex academic institutions of India, i.e. AIIMS, MAMC, New Delhi and PGIMER, Chandigarh, India.

We are thankful to M/s Jaypee Brothers Medical Publishers (P) Ltd., for helping us to make our dream come true.

Niranjan Khandelwal
Veena Chowdhury
Arun Kumar Gupta

Acknowledgments

We would like to put on record our deep appreciation and gratitude:

To Professors Manorama Berry, Sudha Suri and Veena Chowdhury (editor of the present series too) the three pioneers who in 1996 took a bold initiative and started a unique teaching course now popularly known as 'AIIMS-MAMC-PGI' imaging course. Up to 2013, three series of these courses have been completed and the fourth series will start at the end of 2016. This course series has become extremely popular and every course is followed by the publication of a book which too is highly appreciated and popular.

To Professors Sima Mukhopadhyay and Sushma Vashisht who have been the editors of past series and who contributed to organizing the earlier courses in their capacity as Heads of Departments.

To all the associate editors of the different course books who put in immense effort to bring the books out on time.

To all the authors who contributed chapters without whom we could not have collected such an outstanding content of teaching and academic material.

To our respective hospitals for giving us the privilege and unique opportunity to work, which enabled us to amass data from patients and document images of diverse diseases that provide the reader with a wide spectrum of knowledge (and also result in a huge demand for these books).

Our sincere and grateful thanks to Shri Jitendar P Vij (Group Chairman); Mr Ankit Vij (Group President); Mr Tarun Duneja (Director-Publishing); Mr KK Raman (Production Manager); Mrs Samina Khan (Executive Assistant to the Director-Publishing); Mr Neelambar Pant and Mr Mohit Bhargava (Production Coordinators); Mr Akhilesh Kumar Dubey and Mr Ashutosh Pathak (Proofreaders); Mr Bharat Bhushan Verma (Typesetter); Mr Rohan Ram Prasad (Graphic Designer) and other members of M/s Jaypee Brothers Medical Publishers (P) Ltd, New Delhi, India, for their untiring coordination efforts in the production of this book.

We are very proud indeed at the culmination of two decades of these course series, to compile and present them together in the form of these three volumes of *AIIMS-MAMC-PGI's Comprehensive Textbook of Diagnostic Radiology*.

We acknowledge Ms Srishti Sehgal and Dr Chetan Mittal for their support with language corrections and check for plagiarism.

Contents

VOLUME 1: NEURORADIOLOGY INCLUDING HEAD AND NECK, RECENT ADVANCES AND APPLIED PHYSICS IN IMAGING

Section 1: Neuroradiology including Head and Neck

Section 2: Recent Advances and Applied Physics in Imaging

VOLUME 2: GASTROINTESTINAL AND HEPATOBILIARY, GENITOURINARY AND PEDIATRIC IMAGING

Section 3: Gastrointestinal and Hepatobiliary Imaging

Section 4: Genitourinary Imaging

Section 5: Pediatric Imaging

VOLUME 3: CHEST AND CARDIOVASCULAR, MUSCULOSKELETAL, AND BREAST IMAGING

Section 6: Chest and Cardiovascular Imaging

Section 7: Musculoskeletal and Breast Imaging

SECTION 1

Neuroradiology including Head and Neck

- *Evaluation of Plain X-ray Skull: A Systematic Approach*
- *Normal Anatomy of Brain on CT and MRI*
- *Normal Cerebral Angiography*
- *Advances in Computed Tomography Technology*
- *Advances in Neuroimaging Techniques: Magnetic Resonance Imaging*
- *Magnetic Resonance Spectroscopy*
- *Functional Magnetic Resonance Imaging*
- *Imaging and Interventions in Cerebral Ischemia*
- *Imaging of Subarachnoid Hemorrhage*
- *Endovascular Management of Intracranial Aneurysms*
- *Endovascular Management of Arteriovenous Malformations*
- *Endovascular Management of Carotid-cavernous Fistulas*
- *Central Nervous System Infections*
- *White Matter Diseases and Metabolic Brain Disorders*
- *Current Trends in Imaging of Epilepsy*
- *Imaging of Supratentorial Brain Tumors*
- *Imaging of Infratentorial Tumors*
- *Sellar and Parasellar Lesions*
- *Intraventricular Lesions*
- *Imaging of the Temporal Bone*
- *Imaging of the Globe and Orbit*
- *Imaging of the Paranasal Sinuses*
- *Imaging of the Neck Spaces*
- *Thyroid Imaging*

- *Malignancies of Upper Aerodigestive Tract*
- *Imaging of Skull Base Lesions*
- *Maxillofacial Imaging: Imaging of Cysts, Tumors and Tumor-like Conditions of the Jaw*
- *Craniovertebral Junction Anomalies*
- *Endovascular Management of Craniofacial Vascular Lesions*
- *Imaging of Head Trauma*
- *Imaging of Facial Trauma*
- *Imaging of Acute Spinal Trauma*
- *Imaging of Spinal Neoplasms*
- *Spinal Vascular Malformations*
- *Imaging of Low Backache*
- *Localization in Clinical Neurology*
- *Basic Neuropathology*

1 CHAPTER

Evaluation of Plain X-ray Skull: A Systematic Approach

Niranjan Khandelwal, Sudha Suri

INTRODUCTION

In the past, skull radiograph was considered an essential step in the investigative protocol of a patient suspected to have a neurological disease. With the introduction of computed tomography (CT) and magnetic resonance imaging (MRI), there has been a tremendous decline in the usage of plain films and the indications for skull radiographs have been redefined.[1,2] The major indication for skull radiographs is in the evaluation of skeletal dysplasia, diagnostic survey in abuse, abnormal head shapes, infections and tumors affecting the skull bones, metabolic bone disease, leukemia and multiple myeloma. Abnormalities in skull radiographs may be seen in the form of change in the size, density and shape of the skull, as well as the other defects of the skull. In patients presenting with stroke, epilepsy, dementia or in postoperative cases, skull X-rays generally provide no useful information and MRI or CT is the investigation of choice.[3] In patients of trauma, CT should be the first line of investigation except in patients who suffer from facial and orbital fractures where plain films are helpful in orientation and in medicolegal cases.[4-6] Occasionally, skull X-rays may reveal linear fractures with more certainty than a CT scan.[4] In patients suspected to have intracerebral tumors, posteroanterior (PA) and lateral view of skull may provide additional information like detection of hyperostosis in case of meningiomas, presence of lytic and sclerotic metastasis in neuroblastomas and tram-track calcification in Sturge-Weber syndrome which may compliment the diagnosis on CT. The present chapter will describe the normal roentgen anatomy as seen in the basic views of skull followed by systematic approach to the analysis of the abnormal skull X-rays.[7-9]

LATERAL VIEW OF SKULL

A single lateral view of the skull (Fig. 1A) is the most common radiographic X-ray examination to be performed. A systematic approach to the examination consists of evaluation of the size and shape of the cranium, the thickness and density of the bones, the sutures, the vascular markings, the base of skull and the cranial cavity.

Size and shape of the skull is determined by examining the relative size of face and cranium. When the skull is longer and has a relatively shorter vertical diameter, it is referred to as *dolichocephalic*. On the other hand, when the vertical diameter is greater, it is termed as *brachycephalic*. The outer table, the inner table and the diploic space of the bones should be carefully examined for presence of any erosion, sclerosis or widening.

The normal sutures in adults are surrounded by a narrow area of increased density, a fact that helps in distinguishing fracture lines from sutures. Sutures are difficult to visualize in newborns but in children older than 3 years, the width of the suture should not be more than 2 mm. Width of the sutures can be best assessed at the top of the coronal suture in the lateral view. To see the sagittal and the lambdoid sutures, PA and Towne's views are performed. Vascular markings are seen along the coronal suture due to middle meningeal vessels. Arterial grooves become narrower as they go distally. They may be confused with fracture lines but the latter are more radiolucent whereas vascular markings have a halo of increased density around them. Posterior branch of middle meningeal artery as it ascends upward and posteriorly sometimes causes a shadow over the temporal bone that should not be mistaken for a fracture. Enlargement of the arterial grooves may occur in meningioma and arteriovenous malformations (Fig. 1B).

Diploic venous channels are extremely variable in position but are generally seen in the frontal and parietal bones. Venous lakes may be seen as round or oval radiolucent areas and should not be confused with destructive lesions of the bone. Besides the arterial and diploic venous channels, the dural sinuses also produce grooves on the inner table of the skull.

The structures along the base of the skull should be carefully examined, in particular the three lines which represent the floor of the anterior cranial fossa. The upper two lines are formed by the roofs of the orbits, which end posteriorly at the anterior clinoid processes. The lower line is formed anteriorly by the cribriform plate of the ethmoid bone and posteriorly by planum sphenoidale ending at the

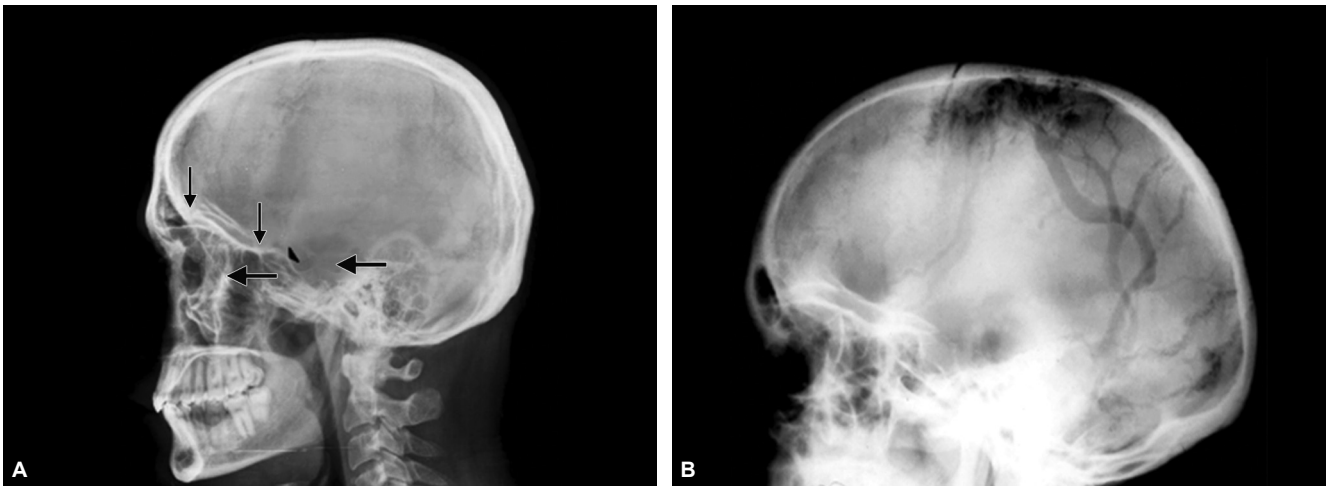

Figs 1A and B: (A) Normal lateral view of skull demonstrates the normal coronal sutures, lambdoid sutures and the vascular grooves due to middle meningeal vessels posterior to coronal sutures. Note the two lines formed by the roof of the orbits ending posteriorly at the anterior clinoid processes. Arrow head marks the tuberculum sellae. Vertical arrows (anterior) show the cribriform plate and the (posterior) planum sphenoidale. Open arrow shows the greater wing of sphenoid bone forming anterior borders of middle cranial fossa. The dorsum sellae (horizontal arrow) with posterior clinoid processes above and the clivus posteriorly are well seen; (B) Lateral view of skull shows multiple dilated vascular markings in the parieto-occipital region in a case of parasagittal meningioma

tuberculum sellae, which marks the superior limit of the anterior wall of the sella turcica. A depression just anterior to the tuberculum sellae is called sulcus chiasmaticus. The roof of the sella posteriorly is formed by the dorsum sellae, which ends in the posterior clinoid processes. Sphenoid sinus is seen below the floor of the sella turcica. The pneumatization of this sinus shows considerable variation. Floor of the middle cranial fossa is formed by the greater wings of the sphenoid on each side, which appear as curvilinear shadows concave outward. These lines serve as a point of reference for locating the temporal lobe of the brain. The dorsum sellae continues as the clivus, which is followed by the occipital bone ending at the anterior margin of the foramen magnum. Clivus is seen to terminate just above the top of the odontoid process of the axis. The normal calcification may be seen in the falx cerebri, petroclinoid ligaments, tentorium, pineal body, habenular commissure and choroid plexus.

Fig. 2: Posteroanterior (PA) view with 15° caudal angulation demonstrates the dense vertical bony projection in the midline due to crista galli, lesser wings of the sphenoid on both sides joining to form the planum sphenoidale (arrow heads). Floor of sella is faintly visualized in the midline (vertical arrows). Oblique line of the orbit is formed by the greater wing of sphenoid in its lower two-thirds and by the frontal bone in its upper one-third

FRONTAL VIEW (FIG. 2)

Posteroanterior projection with 15-20° craniocaudal angulation is preferred to straight PA projection as the petrous pyramids are projected below the orbits and the superior orbital fissure as well as greater and lesser wings of the sphenoid are clearly visualized. PA view is also examined for shape of the skull, with special attention to the symmetry of the two sides. The bony landmarks, which require to be carefully examined for any erosions, sclerosis or lack of continuity include crista galli in the midline, planum sphenoidale, floor of the sella, lesser and greater wings of the sphenoid and the three lines of the orbit formed by the palpable superior border of orbit, highest point of roof of the orbit and the sphenoid ridge which represents the floor of the anterior cranial fossa. The floor of the posterior cranial fossa can also be seen inferiorly. Pacchionian depressions due to arachnoid granulations can be seen in both PA and lateral views as tiny radiolucent areas usually within 2.5–3 cm from the midline. Their margins are well defined superiorly,

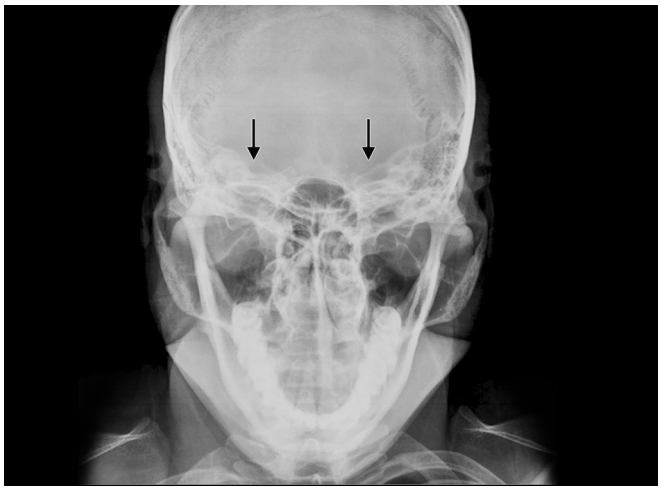

Fig. 3: Towne's view shows foramen magnum in the center with dorsum sellae projecting through it. The parallel lucencies (short arrows) on either side represent the internal auditory canals. Further, laterally pneumatized mastoids air cells can also be seen

Fig. 4: Basal view of skull shows the nasopharynx, sphenoid sinus and ethmoid sinuses in the midline. Posteriorly odontoid process is seen to project into the foramen magnum posterior to the arch of atlas. Laterally, the foramen ovale (open arrow), foramen spinosum, (long arrow), eustachian tube posterior to foramen spinosum and the carotid canal are well visualized. Anterolaterally, the three lines formed by the posterior wall of orbit (arrow head), maxillary sinus (S-shaped) (curved arrow) and the anterior wall of middle cranial fossa (thick arrow) (arched shadow with concavity posteriorly) should be looked for in each case. Medial and lateral pterygoid plates are well seen

whereas inferiorly the margins fade away—a feature helpful in distinguishing these from destructive lesions.

TOWNE'S VIEW

Towne's view (Fig. 3) is performed by angling the tube 35° caudally from the orbitomeatal line. It is generally performed when pathology is suspected in the petrous pyramids. This projection also shows the occipital bone, foramen magnum, dorsum sellae, the internal acoustic canals, mastoids and the condyles of mandible.

BASAL VIEW

Basal view (Fig. 4) of the skull or the submentovertical view is an infrequent examination and is generally performed in specific situations such as looking for the skull base lesions, middle ear or inner ear lesions, nasopharyngeal masses or oropharyngeal lesions and sinus pathologies. The bony landmarks that should always be identified and carefully examined include three lines, constituted by the lateral wall of the maxillary antrum (S-shaped), the posterolateral wall of the orbit, and the anterior wall of the middle cranial fossa which is arched with concavity pointing posteriorly. The lesser wing of the sphenoid is seen just behind the anterior wall of middle cranial fossa. A transverse dense line in the center represents the anterior margin of sella. The medial and lateral pterygoid processes are projected over the sphenoid ridge. Sphenoid sinuses should be carefully seen as early bone destruction in patients of nasopharyngeal carcinoma or sphenoid sinus carcinoma is well demonstrated in this view.

There are three important foramina seen in the basal view. Foramen ovale lying behind the pterygoid processes gives passage to the third division of the trigeminal nerve, an accessory meningeal artery and superficial petrosal nerve. Foramen spinosum lying behind and lateral to foramen ovale transmits the middle meningeal artery. Foramen lacerum is seen anterolateral to the petrous apex and has a well-defined medial margin produced by the internal carotid artery. The eustachian canal is seen behind the foramen spinosum. The external auditory canal is seen behind the condyle of the mandible. Internal auditory canals and inner ear structures including semicircular canals should be carefully looked for. The clivus and foramen magnum are well seen through which the anterior arch of atlas and odontoid process of axis are seen to project. Jugular fossa and jugular foramen are seen laterally on each side of the junction of petrous portion of the temporal bone and occipital bone.

WATERS VIEW

It is one of the standard views to study the maxillary and anterior ethmoidal sinuses. Waters view (Fig. 5) is generally performed with the patient in sitting position to facilitate demonstration of any fluid level in the sinuses. Patient is instructed to keep the mouth open with nose and chin touching the cassette in order to visualize the sphenoid sinuses. It is performed by placing the orbitomeatal line at an angle of 35° with the plane of film by either raising the chin or by tilting the tube. It also gives clear picture of the roof of the orbits, destruction of which may be seen in mucocele of frontal sinus and in carcinoma of lacrimal gland.

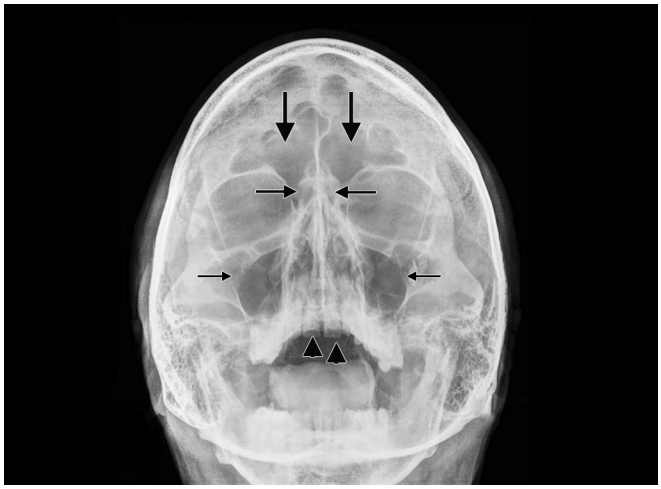

Fig. 5: Waters view of skull shows bilateral maxillary antrum (lower horizontal arrows), frontal sinuses (vertical arrows), ethmoid sinuses (upper horizontal arrows) and lower margin of sphenoid sinuses (arrowheads)

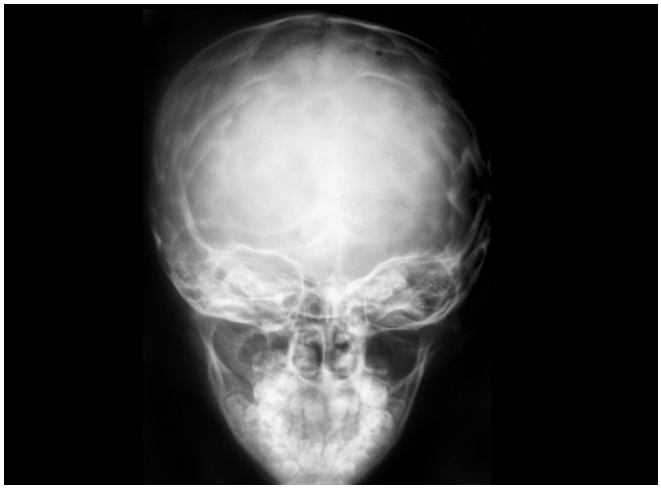

Fig. 6: Craniosynostosis. Anteroposterior (AP) view of skull shows silver beaten appearance due to exaggerated convolutional markings all over the skull vault. None of the sutures is seen

CALDWELL'S VIEW

Caldwell's view is the best projection for examining the frontal and ethmoid sinuses. Patient is positioned directly facing the cassette in either sitting or prone position with midsagittal plane and orbitomeatal line perpendicular to the film with nose and forehead touching the cassette. Central ray is directed 15° caudally to the nasion.

The various abnormalities that can be detected on the plain skull X-rays can be categorized in the following groups:

- Abnormal density
- Abnormal contour of the skull
- Abnormal intracranial volume
- Intracranial calcification
- Increased thickness of the skull
- Single lucent defect
- Multiple lucent defects
- Sclerotic areas.

Abnormal Density

Generalized reduced density: Thinning of the skull bones with decreased done density is seen in osteogenesis imperfecta, hypophosphatasia and achondrogenesis. In hypophosphatasia, there is decreased ossification of the skull and vertebrae or as isolated areas of unusually thin calvarial bone. Osteogenesis imperfecta shows increased osseous fragility leading to multiple fractures in addition to decreased density.

Focal reduced density: Focal areas of defective ossification can occur in the lacunar skull where in well-defined lucent areas are seen corresponding to nonossified fibrous bone and the lacunae are bounded by normally ossified bone.

Generalized increased density: It is seen in sclerosing bone dysplasias such as osteopetrosis, and pyknodysostosis. In osteopetrosis increased density is seen in the basal bones initially and later the calvaria becomes dense and thick. The density of facial bones is relatively less dense.

Localized increased density: It may be seen in fibrous dysplasia, osteoma, craniometaphyseal dysplasia, etc.

Abnormal Contour of the Skull

Normal contour of the skull is maintained by sutures, the intracranial contents and normal bone formation. Abnormality in any of these may result in abnormal contour of the skull.

Premature fusion of the sutures, craniosynostosis, is the most common cause of abnormal contour in children. If the suture closes early, the calvarium expands to accommodate the growing brain in the axis of the fused suture. Sagittal synostosis (scaphocephaly) is the most common form of isolated synostosis with M:F = 4:1.[10] It leads to an elongated narrow boat-shaped skull. The closure of both coronal sutures and lambdoid sutures (*turricephaly)* produces a short wide skull with towering head, with bulging temporal areas and shallow orbits (Fig. 6). The recessed supraorbital rims and hypoplasia of the basal frontal bone, gives cloverleaf-like skull appearance.

Plagiocephaly means skewed or oblique head. It results when there is unilateral such as coronal or lambdoid

synostosis. Unicoronal synostosis is the second most common form of craniosynostosis, after sagittal synostosis. Two-thirds cases occur in female patients and 10% are familial in nature. In this condition, there is elongation of the orbit, elevation of the lateral portion of ipsilateral orbital rim (the harlequin eye appearance) and tilting of the nasal septum and crista galli toward the affected side. Margins of the affected sutures develop sclerosis. Any decrease or increase in the cerebral volume may result in abnormal contour.

Premature fusion of multiple sutures on one side is associated with signs of raised intracranial tension in the form of increased convolutional markings. The hemicalvarium on the ipsilateral side is smaller than the opposite side. The tables of bones of the skull are thickened and there may be elevation of the petrous pyramid on the same side.

Expansion of the bony calvarium due to the presence of slow growing intracerebral or subarachnoid space occupying lesions such as arachnoid cysts may also result in abnormal contour (Figs 7A and B). The bony vault bulges outward with thinning of the inner table. Chronic subdural hematomas may also cause expansion of the adjacent calvarium and may even erode the inner table. Calcifications when present facilitate the diagnosis.

Abnormal bone formation such as that occurs in achondroplasia characterized by defective endochondral ossification, results in shortening of the bones of the skull base as these bones develop from cartilage. Since the bones of the vault develop from membranous bones, these remain unaffected. The result is a small foramen magnum and enlarged cranium with frontal bossing and large jaws.

Abnormal Intracranial Volume

Size of the calvarium is dependent on the size of the intracranial contents. The most accurate way to determine abnormal cranial volume is to measure the skull directly and compare the measurements to standard for age and body size. A simple method of assessing the size of the skull is to compare the skull vault to the size of the face. At birth, the volume of skull is approximately four times that of face. This ratio decreases to 3:1 by age 2 and 1.5:1 by adulthood.[8]

Enlarged head size may result from hydrocephalus, macrocephaly, hydranencephaly and in pituitary dwarfism. The most common cause of hydrocephalus in children is congenital obstruction of the ventricular system and is associated with raised intracranial tension. Sutures become wide due to expansion of the intracranial contents.

Small skull but otherwise normal contour is characteristically seen in microcephaly associated with mental retardation. Cranial sutures fuse early but this is a result of microcephaly and not the cause. The sinuses are large and the digital or convolutional markings are absent or decreased. It is important to differentiate premature closure of all the sutures from microcephaly with fused sutures. When multiple sutures fuse prematurely, the fusion does not occur simultaneously and the result is an irregular skull due to expansion of the skull in unusual directions to accommodate the brain. Clinically, signs of raised intracranial tension are present. Convolutional markings are exaggerated.

Increased thickness of the skull may result due to early cessation of brain growth or due to cerebral atrophy. Increased width of diploic space due to increased hematopoiesis is seen in hemolytic anemia. Progressive hydrocephalus leads to large bony calvarium and a decreased diploic space. However, if a ventricular shunt is performed and abnormal expansion ceases resulting in arrested hydrocephalus, the cranial sutures close and the inner table of bones of the skull become thicker and the diploic space becomes larger. A history of hydrocephalus and the presence of a ventricular shunt facilitate the diagnosis.

Among the hemolytic anemia producing hyperplasia of the bone marrow, thalassemia causes most marked changes.

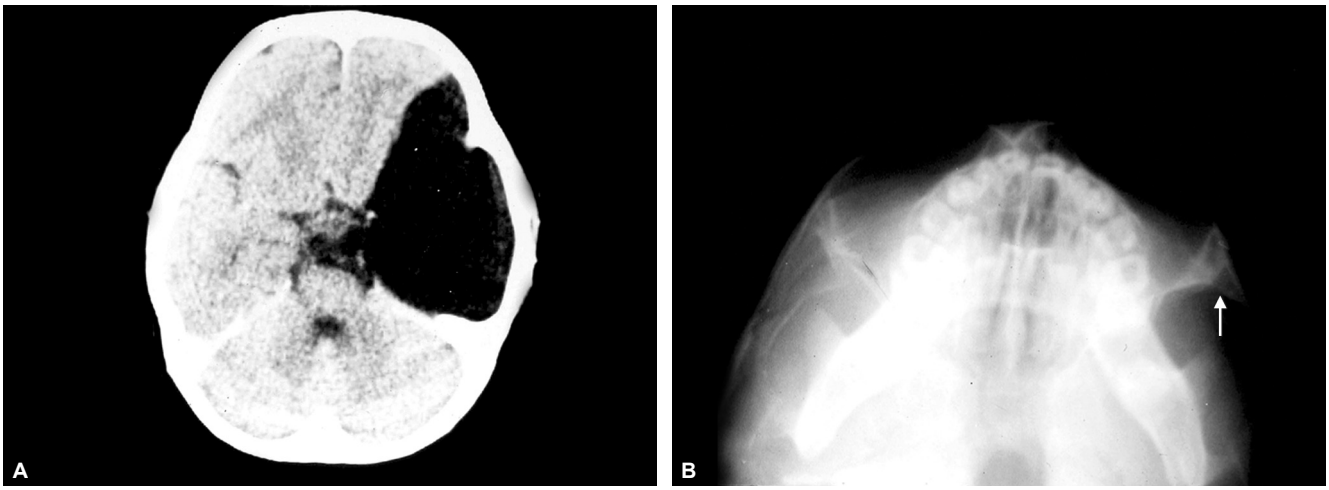

Figs 7A and B: Arachnoid cyst. (A) Basal view of skull shows thinning and ballooning of anterior and lateral walls of the left middle cranial fossa (arrow); (B) Axial CT scan of the same patient shows a large left temporoparietal arachnoid cyst

Fig. 8: Thalassemia. Lateral skull radiograph shows widened diploic space with coarsened trabeculae giving "hair-on-end" appearance typical of hemolytic anemia

Fig. 9: Craniolacunia. Lateral skull radiograph in an infant shows multiple lucencies with intervening dense areas typical of craniolacunia. Note the associated occipital encephalocele and absence of sutural widening

The diploic space is widened with striking radial striations, the "hair-on-end" appearance (Fig. 8). The paranasal sinuses may also be completely obliterated due to widening of the diploic space of facial bones. Such changes may also be seen in other forms of anemia, such as sickle cell disease, hereditary spherocytosis, but the changes are much less marked.

Single Radiolucent Defect

When there is a single lucent lesion, the important considerations that help in deciding its nature are its location, associated soft tissue swelling, table of the bone involved and margins of the lytic lesion, whether sharp, ill-defined or sclerotic. Radiolucent defects in the skull bone may be due to variety of causes, which may be congenital or acquired. Congenital causes may be parietal foramina, anomalous apertures, meningoencephalocele or dermal sinus. The acquired causes include trauma, infections, tumors and histiocytosis.

Bilaterally symmetrical rounded lytic defects located in the posterior parietal bone are characteristic of parietal foramina and are of no clinical significance. Lytic defects due to meningoencephalocele are located in the midline in the frontal or occipital regions and have sharp margins. Associated soft tissue mass clinches the diagnosis. In the first 3 months of life, meningoencephalocele is generally associated with lacunar skull (craniolacunia) (Fig. 9). A *dermal sinus* also occurs in the midline of the skull and may present as a radiolucent defect with a sharp slightly sclerotic border. It is generally associated with a lipoma or a nevus in the overlying soft tissues. These lesions may have an intracranial components which may require a CT scan for demonstration.

Fractures generally occur at the site of injury and may be associated with soft tissue swelling. *Linear nondepressed fractures* may be seen as radiolucent lines and should not be confused with sutures or vascular grooves. Fracture lines are nontapering, nonbranching and have sharp borders whereas vascular grooves have ill-defined borders and an undulating course. Sutures are seen in known anatomical positions and have saw tooth edges. *Depressed fractures* generally occur after severe trauma and are considered more serious than linear fractures. Radiologically, the depressed fragment presents as area of increased radiodensity surrounded by a radiolucent zone (Fig. 10). In children, when the dura beneath the suture is torn, the arachnoid membrane herniates through the dura into the bony defect. The pulsations of the brain lead to progressive enlargement of the arachnoid collection resulting in expansion of the fracture line termed as growing skull

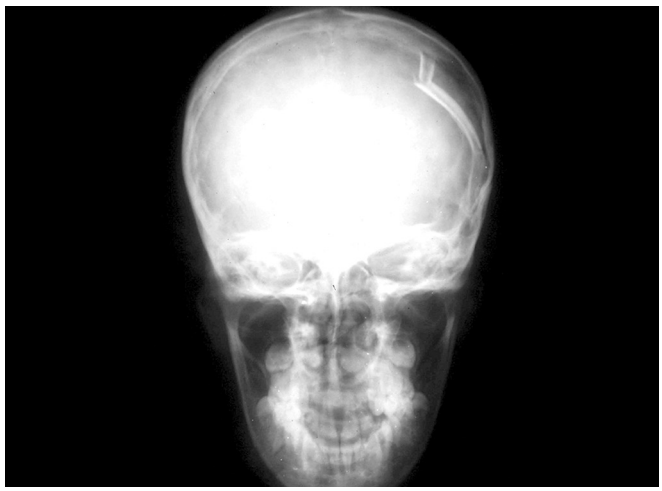

Fig. 10: Depressed fracture. Frontal radiograph shows the parallel dense lines due to depressed bone fragments and associated lucency due to absence of bone

fracture. The bulging membranes result in the formation of leptomeningeal cyst (Fig. 11).

Infections of the skull are uncommon and generally follow trauma or arise secondary to infection elsewhere in the body. The radiographic appearance consists of mottled irregular lucencies, which have ill-defined borders and are associated with soft tissue swelling of the scalp.

Epidermoid tumors develop from a congenital inclusion of epithelial cells within the calvarium. Radiologically, these lesions present as well-defined lytic lesions, which have sclerotic border and are not necessarily located in the midline such as dermoid (Fig. 12). Intracranial epidermoids may also produce a radiolucent shadow, which may mimick a lytic lesion (Figs 13A and B).

Malignant lesions such as primary osteosarcoma or metastasis can also produce lytic defects. Osteosarcoma causes gross destruction of the bone with ill-defined margins and soft tissue swelling (Figs 14A and B). Neurofibromatosis is a rare cause of a lytic defect seen along the suture. This defect is not due to the presence of neurofibroma but is a manifestation of mesenchymal defect. Intracranial mass lesions can also rarely present as lytic areas of the skull.

Eosinophilic granulomas, Hand-Schüller-Christian disease and *Letterer-Siwe disease* all form part of a complex comprising histiocytosis. The severity ranges from mild in eosinophilic granuloma to very malignant course in Letterer-Siwe disease. A single lytic lesion having sharp nonsclerotic

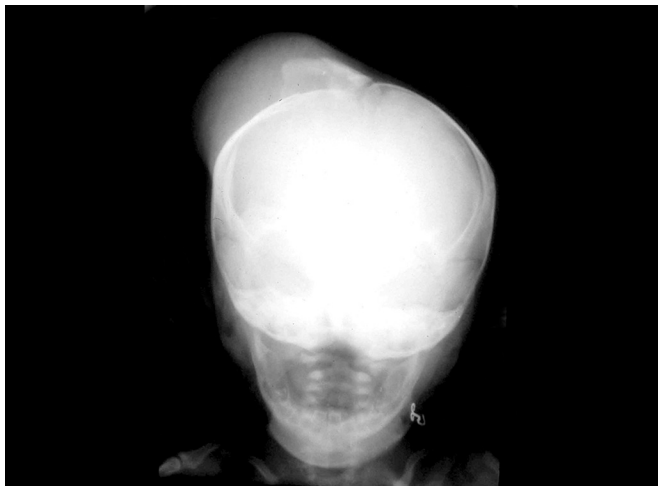

Fig. 11: Growing fracture. Posteroanterior (PA) skull radiographs in a child demonstrate fracture of the right frontal bone with thickening, sclerosis and wide separation of the fracture ends. Note the soft tissue swelling overlying this area

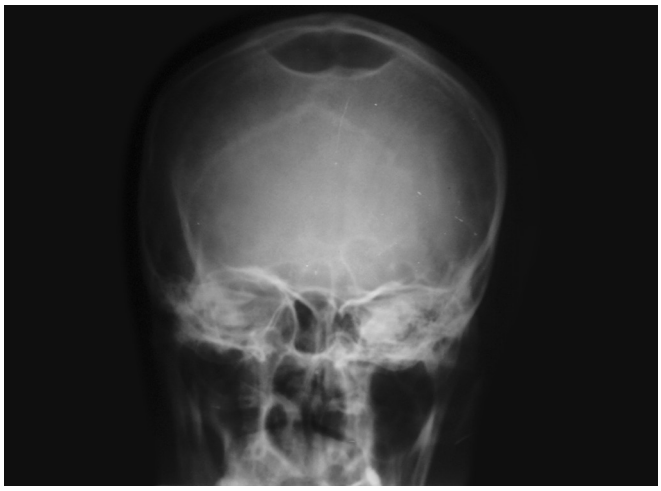

Fig. 12: Dermoid scalp. Skull radiograph shows a well-circumscribed lucency overlying the coronal suture

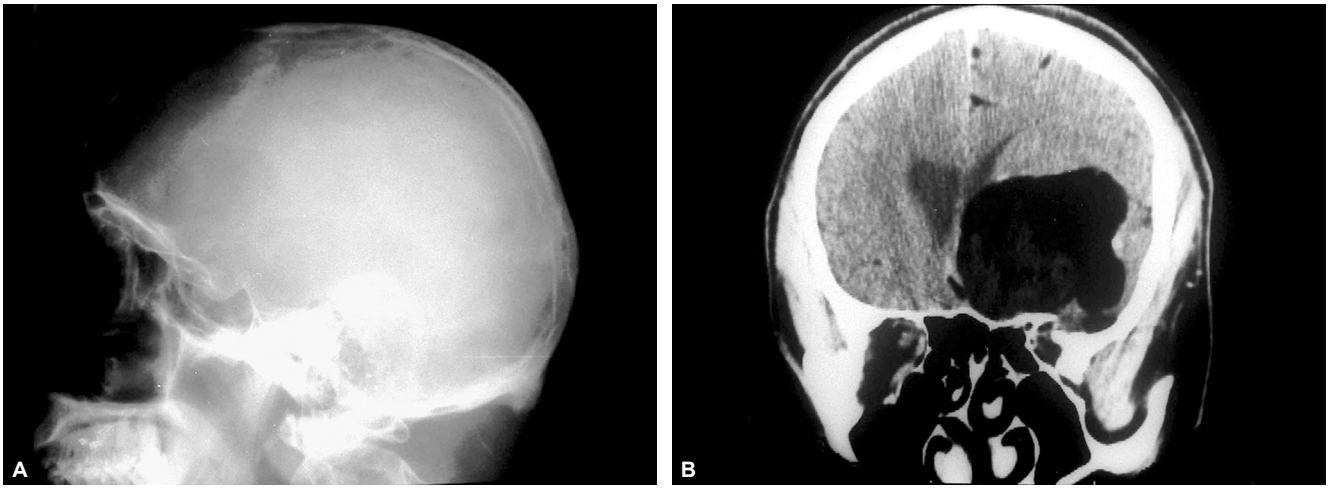

Figs 13A and B: Single lucent lesion. (A) Skull radiograph shows a well-circumscribed lucency overlying the coronal suture mimicking a lytic lesion; (B) Coronal computed tomography (CT) scan in the same patient shows a large hypodense lesion due to epidermoid in the temporoparietal region. No lytic lesion of skull vault is seen

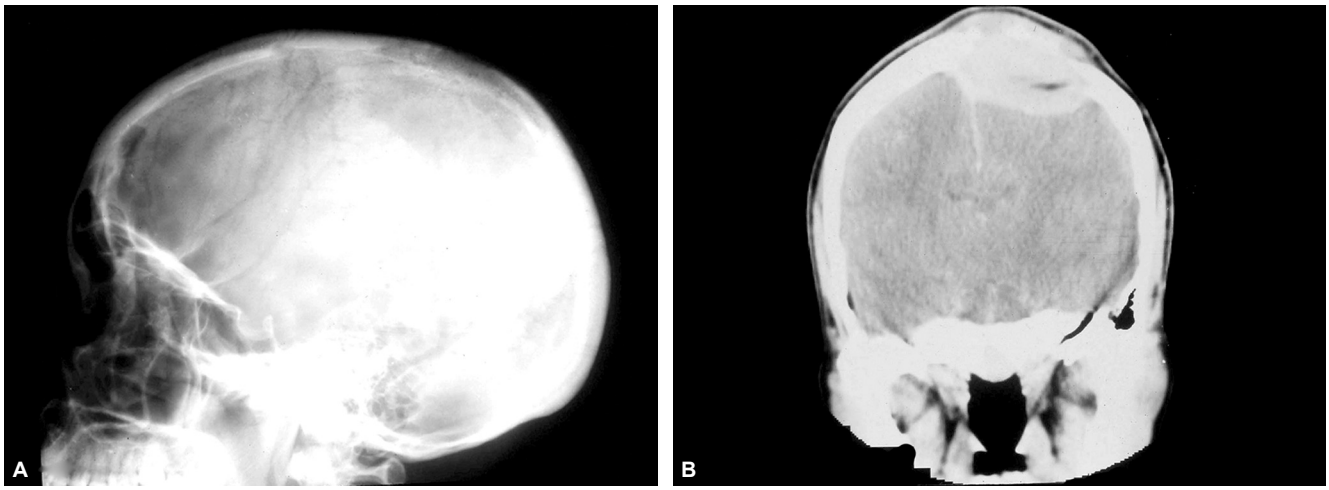

Figs 14A and B: Osteosarcoma. (A) Large lytic area with irregular margin is seen affecting the left parietal bone; (B) Computed tomography (CT) scan of the same patient shows the soft tissue swelling, destruction of the bone and extradural extension of the tumor

Fig. 15: Eosinophilic granuloma. Lateral skull radiograph shows a single lytic lesion having sharp nonsclerotic border and bevelled edges

Fig. 16: Histiocytosis (Hand-Schüller-Christian disease). Lateral radiograph of skull shows multiple well-defined lytic lesions of the vault with bevelled edges characteristic of histiocytosis

border and bevelled edges is characteristic of eosinophilic granulomas (Fig. 15). Occasionally, a small bone is seen in the center representing button sequestrum. Lytic lesions in the other two variants are larger, multiple and punched out (Fig. 16).

Multiple radiolucent defects in the skull in children may be due to craniolacunia, presence of wormian bones, increased convolutional makings due to raised intracranial tension, histiocytosis and metastasis from neuroblastoma (Figs 17A and B), leukemia or Ewing's sarcoma. In adults, multiple myeloma (Fig. 18), metastasis and hyperparathyroidism (Fig. 19) are the usual causes.

Craniolacunia is due to a defect in ossification of the bones, which develop from membranous tissue. There are multiple radiolucent defects seen all over the cranial vault interspersed with strips of normal bone, which appear dense. Craniolacunia (lacunar skull) by itself is not of much significance, but it is generally associated with myelomeningocele or encephalocele (Fig. 9). Appearance must not be confused with *increased convolutional markings* that result from raised intracranial tension and are seen as multiple radiolucent areas not exceeding the diameter of a finger. Convolutional marking may also be seen in normal children in the frontal and occipital region. Presence of increased convolutional markings in the parietal region should generally be considered abnormal. Wormian bones are seen along the sutures and results due to defective mineralization. Multiple wormian bones are seen in cleidocranial dysostosis, osteogenesis imperfecta, hypothyroidism and pyknodysostosis.

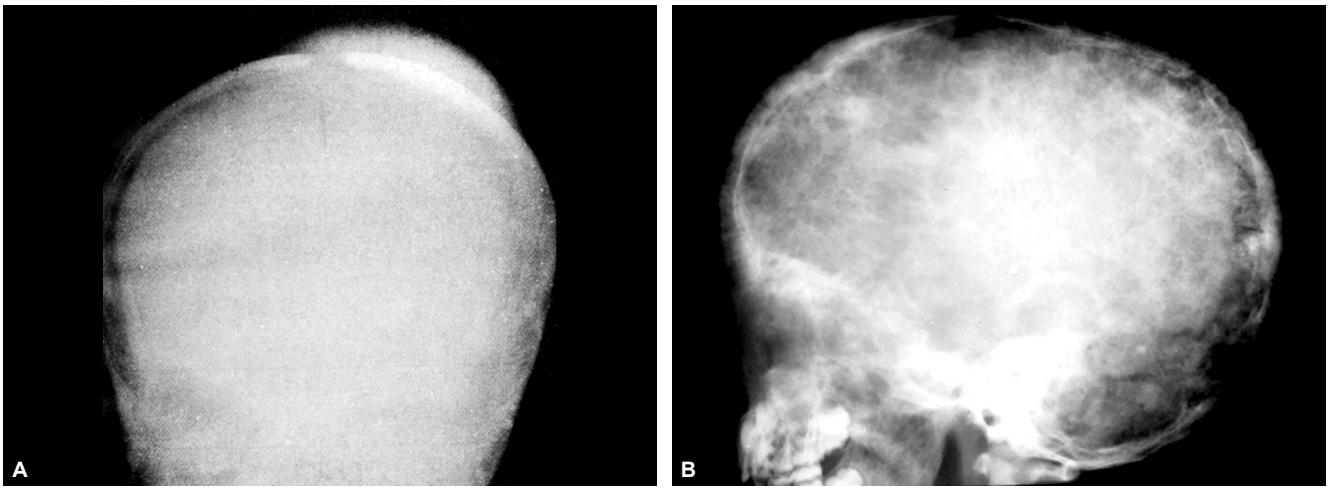

Figs 17A and B: Metastatic lesions of the skull in a child with abdominal neuroblastoma. (A) Sutural metastasis: Frontal skull radiograph shows widening of the sagittal suture with an overlying soft tissue swelling; (B) Diffuse metastasis of skull vault: Lateral skull radiograph shows multiple lytic areas involving both tables of skull and diploic space. Note widening of coronal suture also

Fig. 18: Multiple myeloma. Lateral skull radiographs shows multiple well-defined punched out lytic lesions affecting the skull vault as well as mandible typical of myeloma

Fig. 19: Hyperparathyroidism. Lateral skull radiograph shows multiple lytic lesions with mottled appearance

Lytic lesions seen in *multiple myeloma* are punched out, usually associated with osteoporosis and involve the mandible more frequently compared to *metastasis.* However, many times differentiation from metastasis may not be possible on radiological appearance alone. The sclerosis or sclerotic rim is very rare seen in 3% of cases in multiple myeloma and usually occur after therapy.[11] *Hyperparathyroidism* generally results in mottled demineralization (Fig. 19) but may sometimes cause multiple well-defined lytic areas (Fig. 20).

Sclerotic Areas of the Skull

Areas of increased density in the skull may be seen in both normal as well as pathological conditions. Osteopetrosis is a rare condition, which is characterized by diffuse thickening of the skull and face (Fig. 21). Fibrous dysplasia may involve the vault or base of skull. There may be a single lesion or it may be part of syndrome *(McCune-Albright syndrome*) seen in females when it affects multiple bones and is associated

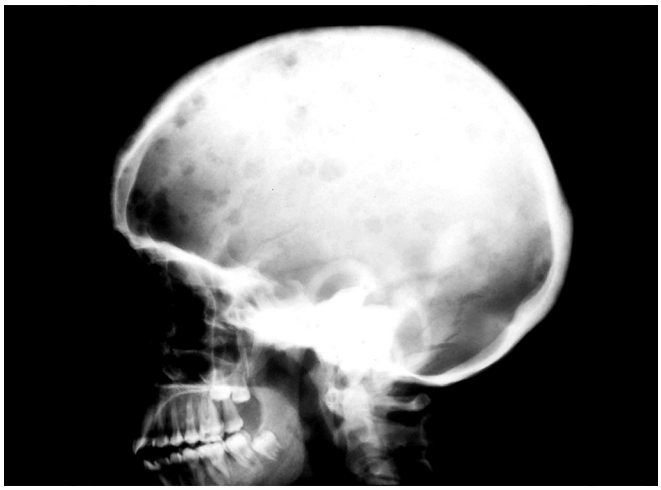

Fig. 20: Hyperparathyroidism. Lateral skull radiograph shows multiple well-circumscribed rounded lytic lesions involving skull vault with bone within bone appearance—an unusual feature of hyperparathyroidism

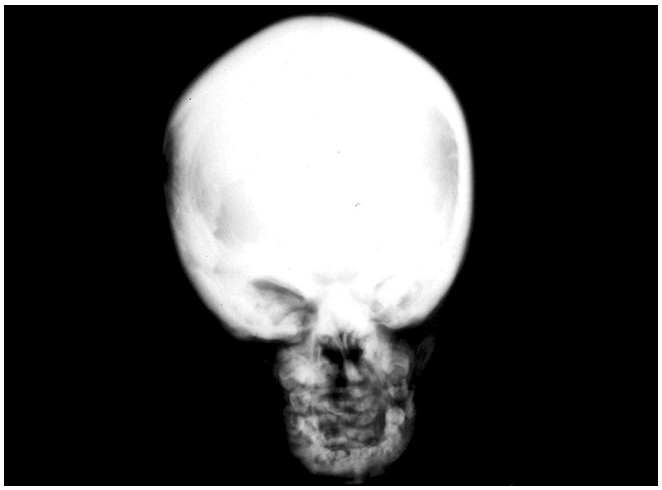

Fig. 21: Osteopetrosis. Frontal radiograph shows diffuse increased density affecting all bones of the skull vault as well as base

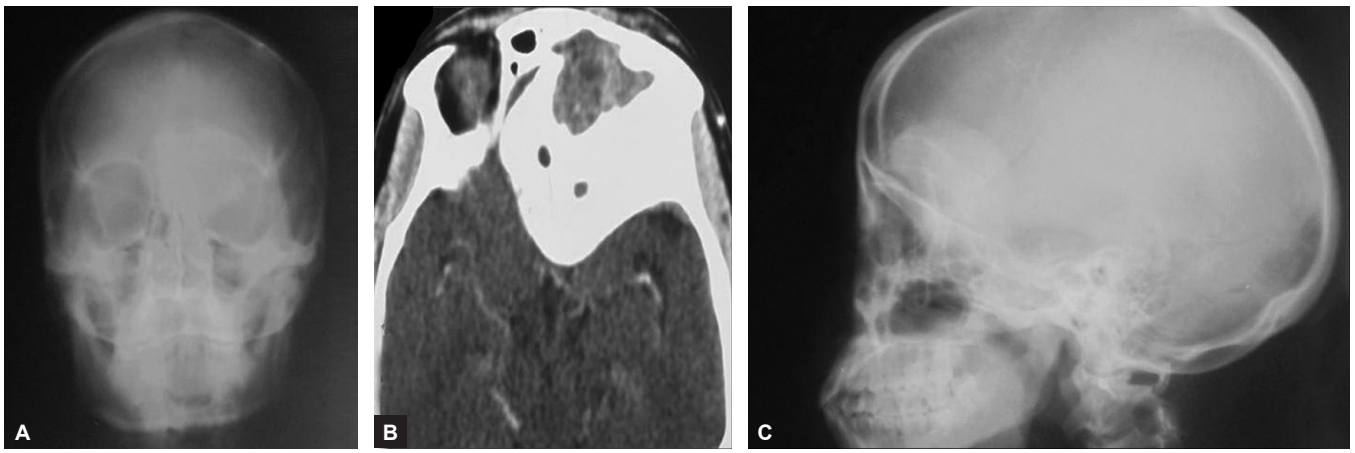

Figs 22A to C: Fibrous dysplasia. (A) Frontal and (B) lateral views of skull reveal sclerotic lesion involving the frontal bone. The frontal sinus is opaque; (C) Axial computed tomography (CT) scan in the same patient shows expanded sclerotic frontal bone

Fig. 23: Paget disease. Lateral view of skull reveals focal areas of opacities in previous areas of osteoporosis giving "cotton wool" appearance

with precocious puberty. The lesions are sclerotic with loss of normal trabecular pattern. Mixed types of lesions with sclerotic and lytic areas are also known to occur (Figs 22A to C). Paget disease in the mixed phase shows marked thickening of the diploic space, particularly the inner calvarial table, causing marked enlargement. The areas of sclerosis may be circular and occur in previous areas of osteoporosis. This pattern often creates focal areas of opacity giving "cotton wool" appearance at radiography (Fig. 23). Multiple hyperostotic lesions affecting the calvarium measuring 5–10 mm in size may be seen in tuberous sclerosis in association with calcified lesion in periventricular region. Thickening of the frontal and parietal bones may occur in rickets due to presence of poorly mineralized bone, which on healing becomes dense. An *osteoma* affecting the skull bones is a benign tumor, which appears as a dense lesion projecting extracranially from the outer table of skull. Osteoma is also the most common benign tumor affecting the sinuses (Fig. 24). Focal areas of

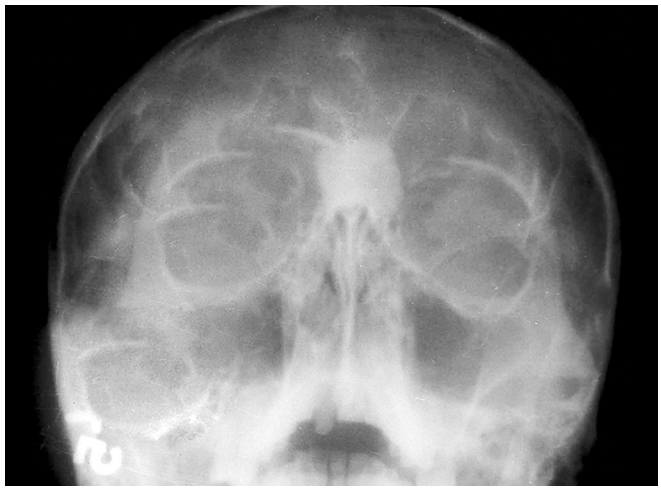

Fig. 24: Osteoma. Waters view of skull shows osteoma of the frontal sinus

hyperostosis are characteristic of *meningioma* (Figs 25A and B). When the hyperostosis affects the frontal bone, in a case of convexity meningioma, it must be differentiated from *hyperostosis frontalis interna* (Fig. 26), the later is generally seen in elderly females and affects the inner table with sparing of diploic space and does not cross the midline.

Intracranial Calcification

Presence of calcification can provide important clue to the diagnosis in several conditions. Although causes are numerous (Box 1), some of these conditions have specific appearance, which can be diagnostic.

The most common physiological calcification occurs in the pineal gland. It is seen in the midline approximately 3 cm above and behind the posterior clinoids in the lateral view (Fig. 27). Size of the pineal calcification is most important as

Figs 25A and B: Sphenoid wing meningioma. (A) Posteroanterior (PA) view of skull shows hyperostosis of the left lesser and greater wings of the sphenoid bone typical of meningioma; (B) Contrast enhanced computed tomography (CT) scan in the same patient shows proptosis and hyperostosis of sphenoid wings with enhancing extradural mass due to meningioma on the left side

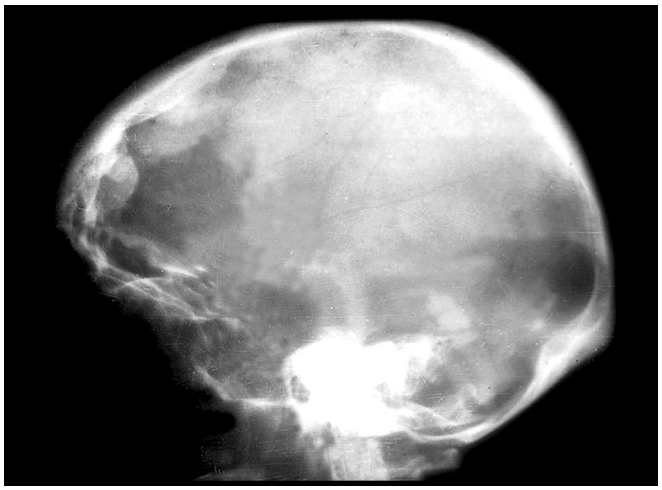

Fig. 26: Hyperostosis frontalis interna. Lateral skull radiograph shows irregular thickening of the frontal bone in an elderly female. The inner table is involved more than the outer table with sparing of diploic spaces

Box 1: Abnormal intracranial calcification
Familial conditions: • Tuberous sclerosis • Sturge-Weber syndrome • Idiopathic familial cerebrovascular calcinosis (Fahr's disease)
Metabolic causes: • Hypoparathyroidism • Pseudohypoparathyroidism
Inflammatory diseases: • Cytomegalic inclusion disease • Toxoplasmosis • Rubella • Abscess
Vascular causes: • Arteriovenous malformation • Intracerebral hematoma • Subdural hematoma
Neoplasms: • Craniopharyngioma • Astrocytomas • Oligodendrogliomas • Pinealoma

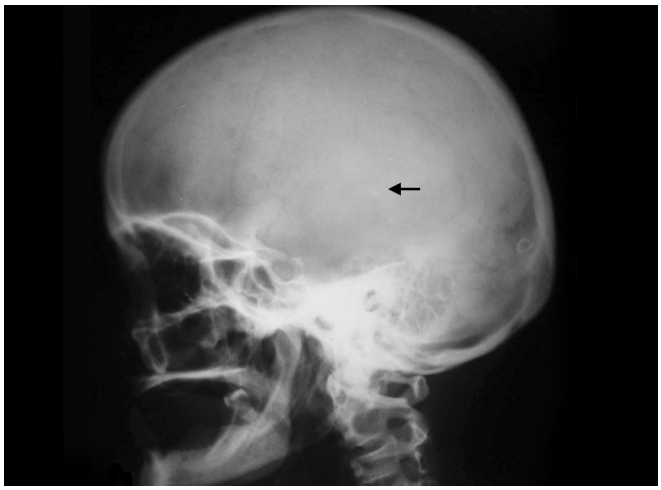

Fig. 27: Lateral view skull shows pineal gland calcification (arrow)

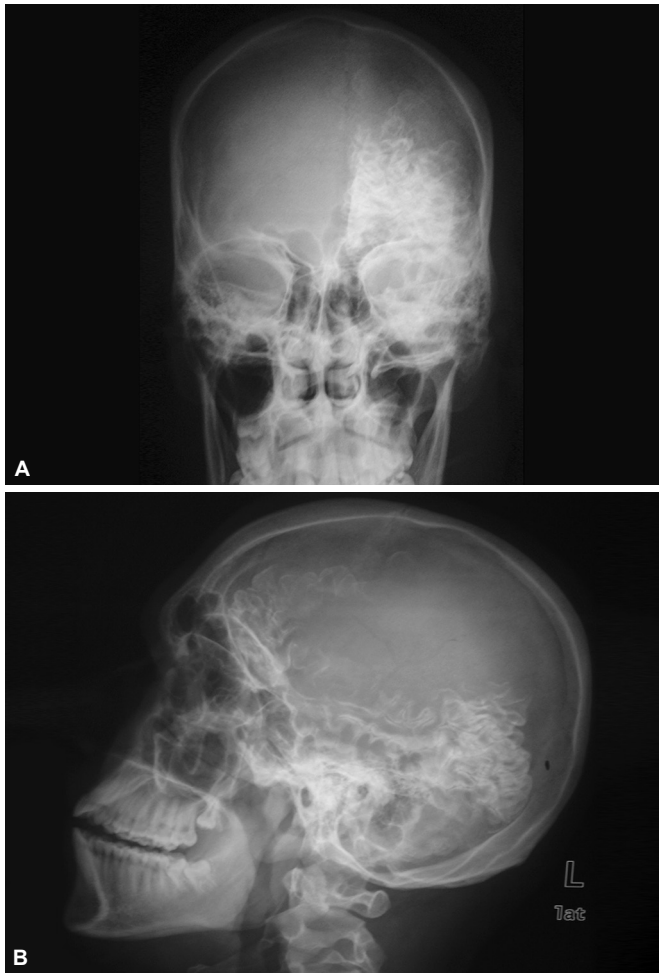

Figs 28A and B: Sturge-Weber syndrome. (A) Posteroanterior (PA) and (B) lateral view of the skull shows gyriform calcification on the left side

any increase in size more than 10 mm is abnormal and raises the possibility of pinealoma.

Habenular commissure calcification has a characteristic appearance and is seen as a C-shaped structure open posteriorly. It lies above and anterior to pineal gland. Choroid plexus calcification is generally bilateral and may be unequal on the two sides. Other normal sites of calcification are the falx and anterior petroclinoid ligaments above the sella.

Tuberous sclerosis is a syndrome comprised of epilepsy, mental retardation and adenoma sebaceum. Multiple hamartomas occur in the brain as well as at other sites such as kidneys. Tumors consist of glial tissue and ganglion cells. In the brain they are usually multiple and are seen in the subcortical, subependymal and basal ganglia regions. Calcification is seen in 50% of the lesions.

Sturge-Weber syndrome is another important cause of intracranial calcification. Patients present with epilepsy and mental retardation and often have cutaneous hemangioma in the distribution of trigeminal nerve on the same side as calcification. Calcification has a typical tram-track appearance and is seen in the cerebral cortex (Figs 28A and B).

Basal ganglia calcification is an important feature of hypoparathyroidism and pseudohypoparathyroidism. Widespread irregular and punctate areas of calcification, which are diffusely scattered, are characteristic of Fahr's disease. In this condition, patients present with severe growth and mental retardation. The disease is hereditary and is characterized by microscopic deposits of iron and calcium in the basal ganglia, cerebellum and subcortical region. Infections due to toxoplasma and cytomegalovirus are important causes of intracranial calcification in the newborn. Calcifications are multiple and diffusely scattered in the brain parenchyma or paraventricular region. Bacterial infections may progress to cerebral abscess, which may get calcified.

Arteriovenous malformations calcify in 2–25% of all affected patients. Typically, calcification is in the form of an incomplete ring but may be nodular or amorphous. A large arc like calcification seen in the region of pineal gland in a newborn presenting with congestive heart failure and hydrocephalus is characteristic of vein of Galen aneurysm. Intracerebral or chronic subdural hematomas may reveal curvilinear calcification. A variety of tumors may show calcification. In children, suprasellar craniopharyngioma is the most common tumor, which reveals calcification whereas in adults oligodendrogliomas and meningiomas are the common tumors to calcify.

REFERENCES

1. Tress BM. The need for skull radiography in patients presenting for CT. Radiology. 1983;146(1):87-9.

2. Moseley I. Long-term effects of the introduction of noninvasive investigations in neuroradiology. Neuroradiology. 1988;30(3):193-200.
3. Rastogi SC, Barraclough BM. Skull radiography in patients with psychiatric illness. Br Med J. 1983;287(6401):1259.
4. Taveras JM. Anatomy and examination of skull. In: Interactive Review of Radiology. Lippincotts Williams and Wilkins, 1999.
5. Sanders R, MacEwen CJ, McCulloch AS. The value of skull radiography in ophthalmology. Acta Radiol. 1994;35(5):429-33.
6. Baker HL Jr. The impact of computed tomography on neuroradiologic practice. Radiology. 1975;116(3):637-40.
7. Taveras JM. The skull. In: Taveras JM, Wood EH (Eds). Diagnostic Neuroradiology, 2nd edition. The Williams and Wilkins Company. 1986.pp.1-65.
8. Gerald B. Systematic radiographic evaluation of the abnormal skull. In: Rabinowitz JG (Ed). Pediatric Radiology. Philadelphia: JB Lippincott Company. 1978.pp.285-313.
9. Butler P, Jeffiree MA. The skull and brain. In: Butler P, Mitchell AWM, Ellis H (Eds). Applied Radiological Anatomy, 1st edition. Cambridge University Press. 2001.pp.17-60.
10. Kirmi O, J Lo S, Johnson D, et al. Craniosynostosis: a radiological and surgical perspective. Seminars in ULTRASOUND CT and MRI. 2009;30(6):492-512.
11. Baur-Melnyk A, Reiser M. Oncohaematologic disorders affecting the skeleton in the elderly. Radiol Clin North Am. 2008;46(4):785-98.

Normal Anatomy of Brain on CT and MRI

2 CHAPTER

Paramjeet Singh

INTRODUCTION

An understanding of basic anatomy of the brain is vital to the planning and interpretation of neuroradiologic studies. Modern imaging techniques provide cross sections of the brain similar to the dissected brain. Computerized tomography (CT) provides cross-sectional anatomy of the brain in axial plane. Magnetic resonance imaging (MRI) due to its multiplanar capabilities also allows direct coronal and sagittal sections. Better tissue differentiation on MRI allows not only morphological but also histological information to some extent. Recent advances in functional imaging and diffusion tensor imaging makes understanding of brain anatomy even more important. Current MRI scanners and multidetector computerized tomography (MDCT) have further expanded the scope of three-dimensional conceptualization of complex brain structures through true volumetric data sets. This chapter reviews the essentials of surface and cross-sectional anatomy of the brain as seen on CT and MRI.

TECHNIQUES AND NORMAL APPEARANCE

General Considerations

Noncontiguous axial CT sections are usually obtained at 15–20° angulation to the orbitomeatal line, while axial MRI sections are generally obtained parallel to it (along bicommissural plane). MRI, owing to its multiplanar capability allows direct coronal and sagittal sections. However, MDCT scanners and newer MR techniques allow volumetric data acquisitions. T1- and T2-weighted (T1W and T2W) images are routinely obtained on MRI. The T1WI are excellent for showing anatomy while T2WI are highly sensitive in detecting brain pathology.

The white matter is hypodense to gray matter on CT. The cerebral white matter appears bright while the gray matter is relatively dark on T1WI. The relationship reverses as white matter becomes progressively darker on increasing the T2-weighting; the crossover occurring in the proton density images. The basal ganglia, red nucleus and putamen appear hypointense on T2WI due to their mineral contents.

The cerebrospinal fluid (CSF) shows low density on CT (0-15HU) depending on its protein content. The CSF is hypointense on T1WI and extremely bright on T2WI due to its long T1 and T2 relaxation times. The CSF is in constant motion which may occasionally result in flow-related artifacts and loss of signal (flow void), classically seen in the region of cerebral aqueduct. The glomera of the choroid plexus within the lateral ventricles are seen as soft tissue density on CT and show homogeneous enhancement on CECT. On T2WI the choroid plexus appears heterogeneous due to the presence of calcification and cysts.

Visualization of blood vessels needs administration of iodinated contrast in CT. On MRI, major blood vessels are visualized without contrast administration and appear as flow voids on spin echo imaging or show flow-related enhancement on gradient echo imaging. Flow-related artifacts are often seen in phase encoding direction especially in long TR sequences and should not be mistaken for pathology. Familiarity with normal variations like dilated perivascular spaces is important. Modern MR imaging also provides a good understanding of white matter tracts through diffusion tensor imaging and functional areas of the brain through BOLD imaging.

Except for the intraorbital segment of the optic nerves, the remaining cranial nerves are usually not visualized on CT. On MR, using thin sections and fluid sensitive techniques like SPACE and CISS, the cisternal segments of most of the cranial nerves can be identified.

The inner meningeal layers are not normally visualized on noncontrast MRI and may show no or fine linear enhancement following contrast administration. Major dural folds like falx and tentorium appear hypointense on MRI and enhance after contrast administration along with the venous sinuses within them. Contrast-enhanced MR angiograms are increasingly used for demonstrating vascular anatomy.

The diploic space appears bright on T1WI due to its fat content and is outlined by the low signal intensity compact

bones of the inner and outer tables of skull. CT better demonstrates the bony outlines. Similarly, it is superior to MR for visualization of intracranial calcification.

Normal Anatomy of Brain

Figure 1 shows the major subdivisions of brain. Brain consists of three major components.

1. Forebrain (prosencephalon) comprised of two cerebral hemispheres (telencephalon) and fiber tracts connecting the cerebral hemisphere with the midbrain (diencephalon).
2. The midbrain (mesencephalon).
3. The hindbrain (rhombencephalon) comprised of cerebellum and pons (metencephalon), and medulla oblongata (myelen-cephalon).

CEREBRAL HEMISPHERES

Cerebrum consists of two hemispheres which are partially connected with each other through corpus callosum. Each cerebral hemisphere has three borders superomedial, inferomedial and inferolateral. The superomedial border separates the superolateral and medial surfaces, the inferolateral border separates the superolateral and inferior surfaces, and the inferomedial border separates medial surface and inferior surface.

Lateral Surface of the Cerebral Hemisphere (Fig. 2A)

The two cerebral hemispheres are incompletely divided by the interhemispheric fissure. The sylvian fissure (lateral fissure) separates the temporal lobe from the frontal and parietal lobes. Its anterior horizontal and anterior ascending rami extend into the inferior frontal gyrus. The posterior ramus passes backward and upward terminating into ascending and descending rami. The central sulcus separates the frontal from the parietal lobe (Fig. 3E). It originates slightly behind the mid-point between the frontal and occipital poles on the superomedial border and continues obliquely inferolaterally on the lateral surface.

The frontal lobe is bounded posteriorly by the precentral gyrus, which lies between the central and precentral sulci (Fig. 4E). The precentral gyrus contains the primary motor area with inverse topographic representation of contralateral body parts. The superior frontal sulcus and inferior frontal sulcus divide the frontal lobe anterior to precentral gyrus into superior, middle and inferior gyri (Figs 3E, F, 5A, B and 6H, J, K). In front of the precentral gyrus is the premotor area, consisting of posterior part of the superior, middle and inferior frontal gyri. The Broca's area which is concerned with the motor mechanisms of speech also lies at the posterior part of the inferior frontal gyrus in the dominant lobe usually seen at the level of frontal horns on axial sections.

The convexity of the parietal lobe consists of the postcentral gyrus and the superior and inferior parietal lobules separated by the horizontally running intraparietal sulcus (Figs 3E and F). The postcentral gyrus is located between the central and postcentral sulcus and contains the primary (somesthetic, tactile, thermal and kinesthetic) areas, with body representation corresponding to that in precentral gyrus. The inferior parietal lobule is further subdivided into the supramarginal and angular gyri, which are located around the terminal ascending ramus of the sylvian fissure and the superior temporal sulcus, respectively (Fig. 3E). The temporal

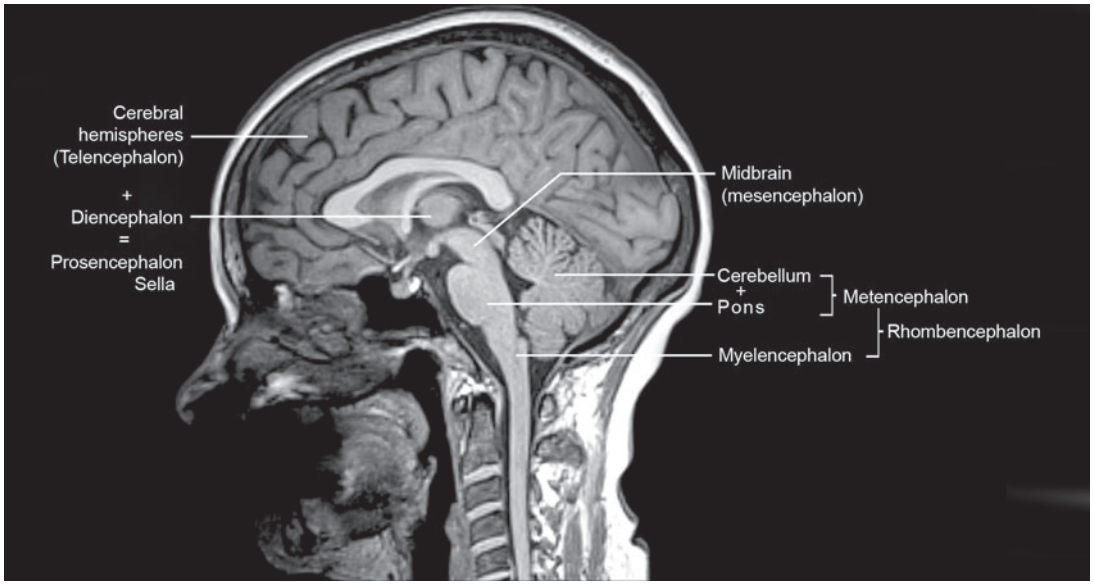

Fig. 1: Midline sagittal image of brain showing embryonal divisions

lobe is divided into superior, middle and inferior temporal gyri by two horizontally running sulci—the superior and middle temporal sulcus (Fig. 3F). In the dominant cerebral hemisphere at the posterior portion of the superior temporal gyrus lies the Wernicke's area, linked with comprehension of language. A lesion of this area causes sensory aphasia. Another important area is the area for hearing — acoustic area, which is also located in the temporal lobe. It lies in that part of the superior temporal gyrus which forms the inferior wall of posterior ramus of lateral sulcus and is defined as the

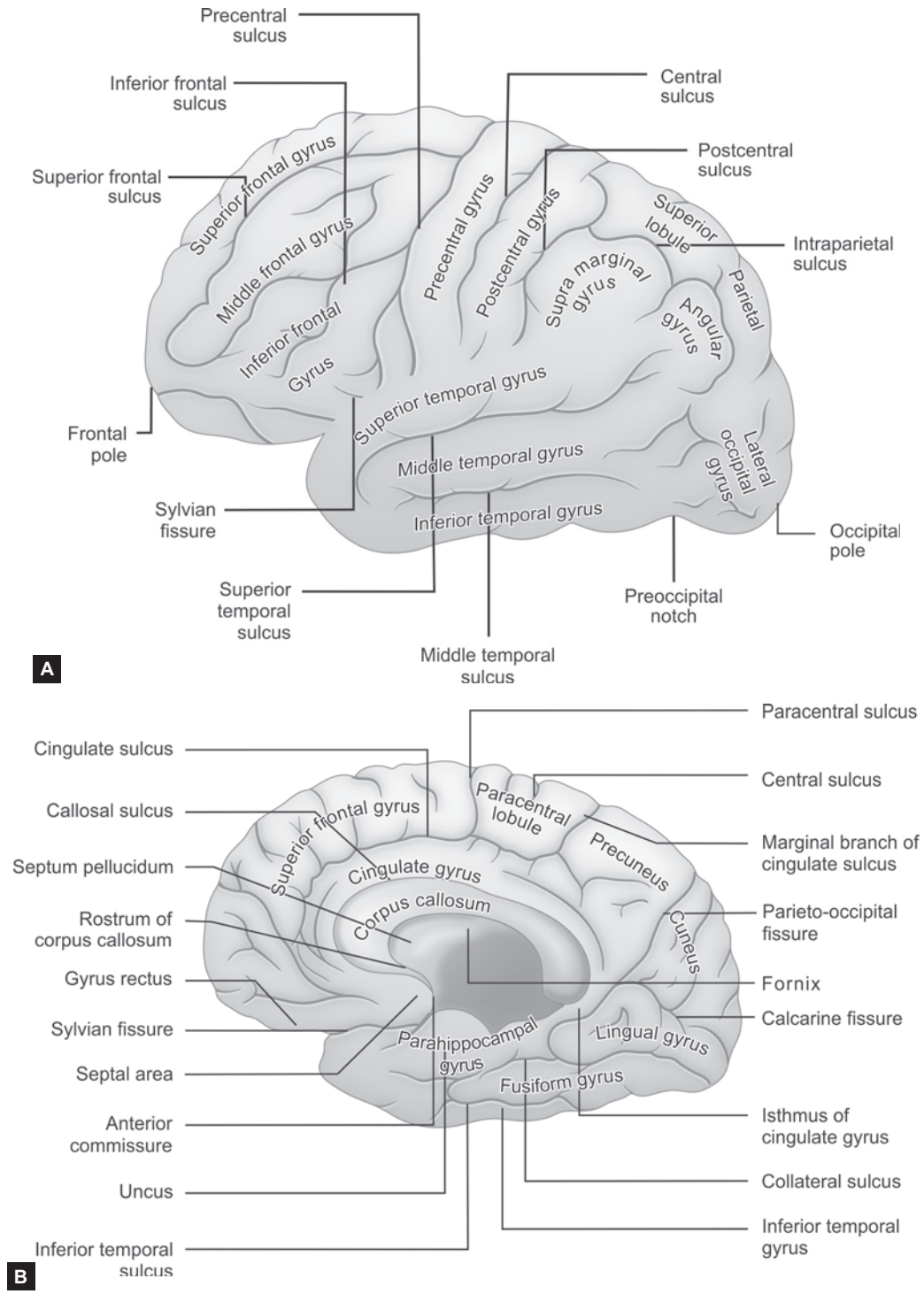

Figs 2A and B

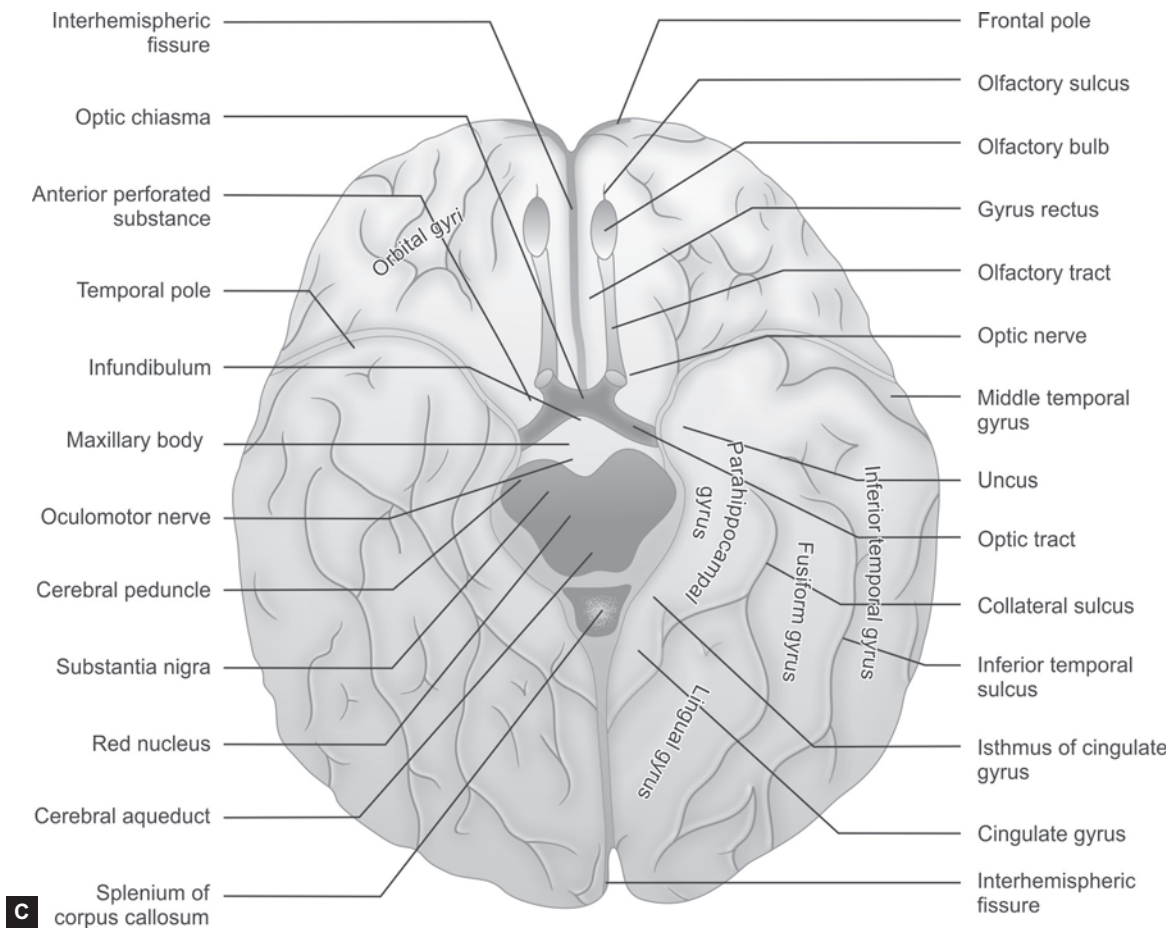

Figs 2A to C: Diagrammatic representation showing anatomy of cerebral hemispheres on the (A) Lateral; (B) Medial; and (C) Inferior surface

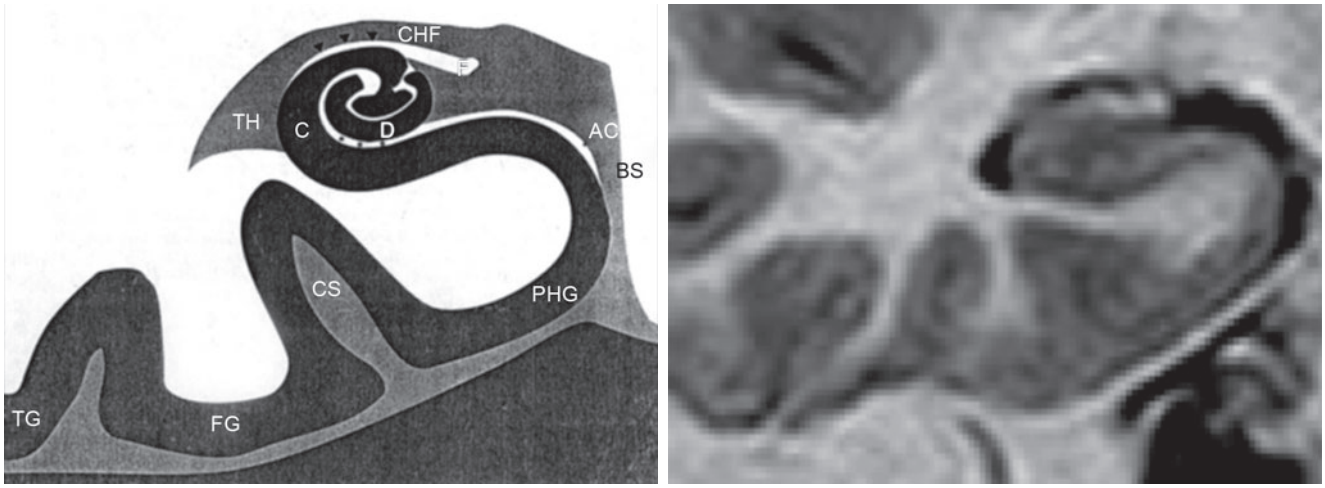

Fig. 2D: Line diagram and corresponding coronal inversion recovery image of right hippocampus
Abbreviations: AC, ambient cistern; BS, brainstem; C, cornu ammonis; CHF, choroid fissure; CS, collateral sulcus; D, dentate gyrus; FG, fusiform gyrus; F, fimbria; TH, temporal horn; TG, inferior temporal gyrus; PHG, parahippocampal gyrus

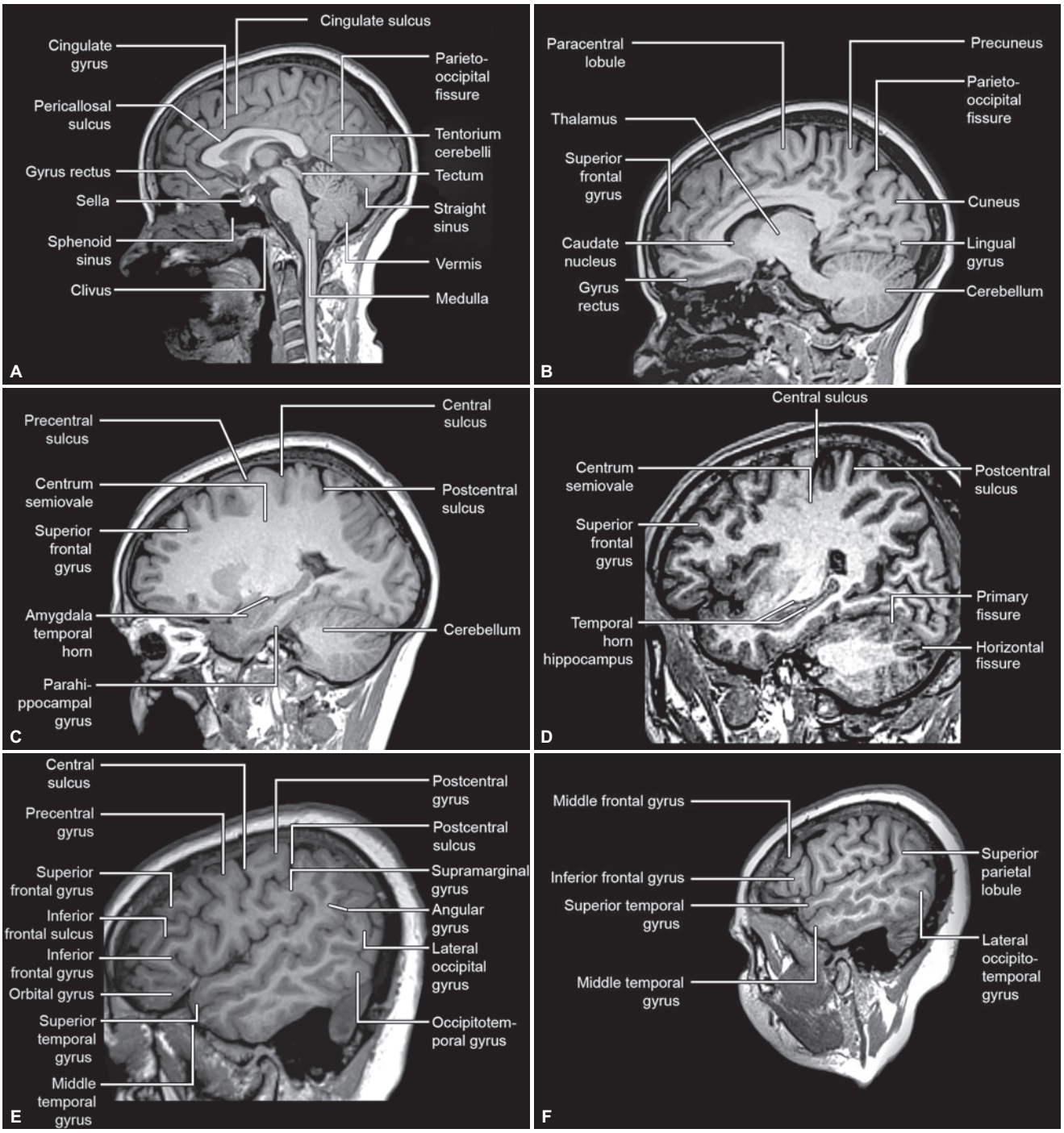

Figs 3A to F: (A) Mid-sagittal MR section shows the entire length of the corpus callosum bordered above by the pericallosal sulcus. Cingulate gyrus and sulcus lie above it. The brainstem divisions, cerebellar vermis and the sellar/suprasellar anatomy are exquisitely shown on this section. The vein of Galen and straight sinus are seen behind the splenium leading to the torcula. A large rounded mass of gray matter within the 3rd ventricle represents interthalamic adhesion. The fornix is seen beneath the corpus callosum. The 3rd and 4th ventricles with the interconnecting aqueduct are well shown in this section. The tectal plate lies posterior to the aqueduct. The suprasellar cistern interpeduncular fossa, quadrigeminal plate cistern and cisterna magna are important cerebrospinal fluid (CSF) spaces identified in this section; (B to D) Parasagittal MR sections. The parieto-occipital fissure marks the boundary between parietal (precuneus) and occipital (cuneus) lobes. The calcarine fissure separates lingual gyrus from cuneus. The central, pre- and postcentral sulci and the related gyri can be followed. The parahippocampal gyrus can be seen following the temporal horn closely. The frontal lobe consists of superior and middle frontal gyri on these sections; (E and F) Sagittal MR sections at and lateral to sylvian fissure. The sylvian fissure can be traced anteriorly where its anterior ascending and horizontal rami form a V or Y configuration. These divide the inferior frontal gyrus into pars orbitalis, pars triangularis and pars opercularis giving it a characteristic M shape. Posteriorly the fissure ends in ascending and descending rami. The horse-shoe shaped supramarginal gyrus sits atop the ascending ramus. The middle frontal gyrus extends posteriorly to meet the precentral gyrus and the inferior frontal sulcus meets the obliquely coursing precentral sulcus. The central sulcus can be traced inferiorly to the subcentral gyrus. The superior and inferior temporal gyri are identified in the extreme lateral sections

transverse temporal gyrus. This is best seen in the coronal sections.

The lateral surface of the occipital lobe consists of the lateral occipital gyri (Fig. 5I) (visual associative functions). The preoccipital notch indents the inferolateral border of the hemisphere about 4 cm from the occipital pole. An imaginary line drawn from the superior end of the parieto-occipital fissure to the preoccipital notch marks the boundary between the occipital lobe and the parietal and temporal lobes. Insula (central lobe) is the part of cerebral cortex which lies in the depth of the lateral sulcus. It is formed by portions of the frontal, parietal and temporal lobes (Figs 5C and 6H).

Medial Surface of the Cerebral Hemisphere (Fig. 2B)

The corpus callosum is a large mass of nerve fibers which connect the cerebral hemispheres and forms most of the roof of the lateral ventricles. It is arbitrarily divided from front to back into rostrum, genu, body, and splenium (Fig. 3A). The small anterior commissure ventral to the rostrum of the corpus callosum connects portions of the middle and inferior temporal gyri. The two lateral ventricles are separated by septum pellucidum (Fig. 4D) which extends from the inferior aspect of the body and genu of the corpus callosum to the superior aspect of the columns of the fornix (Figs 5C and D).

The callosal sulcus separates the corpus callosum from the cingulate gyrus. The cingulate sulcus separates the cingulate gyrus from the superior frontal gyrus anteriorly and the paracentral lobule posteriorly (Figs 3A and B). The central sulcus is deficient on medial surface and continuations of the precentral and postcentral gyri form the paracentral lobule on medial surface which is limited posteriorly by the marginal branch of the cingulate sulcus and anteriorly by the paracentral sulcus, a direct continuation of the precentral sulcus from the lateral surface. On the medial surface the parietal lobe (precuneus) is separated from the occipital lobe by parieto-occipital fissure (Figs 3B, C and 6J, K).

The calcarine fissure divides the medial surface of occipital lobe into the cuneus above and the lingual gyrus below (Figs 6H and I). The calcarine (primary visual) cortex, consisting of portions of the cuneate and lingual gyri lies along the banks of the calcarine fissure deep within the occipital lobe. At the inferolateral aspect of the occipital and temporal lobes lies the fusiform (lateral occipitotemporal) gyrus.

The cingulate gyrus continues posteriorly behind the corpus callosum through the isthmus into the parahippocampal gyrus which is separated from the fusiform gyrus by the collateral sulcus. The uncus is the most anterior part of the parahippocampal gyrus which points medially (Fig. 4B).

Understanding of anatomy of medial temporal lobe is important to interpret the MR findings in hippocampal sclerosis in epilepsy. Hippocampus is located on the medial aspect of temporal lobe, superior to the parahippocampal gyrus bounded superolaterally by the floor of the temporal horn of lateral ventricle. It is composed of two interlocking U-shaped lamina of gray matter called cornu ammonis and dentate gyrus. White matter tracts extend form cornu ammonis to alveus, which converge medially to form fimbria. Cornu ammonis is connected with gray matter of parahippocampal gyrus through subiculum. Choroid fissure lies superomedial to hippocampus and medially lies the ambient cistern (Fig. 2D). Anteroposteriorly hippocampus is divided into head, body and tail.

Inferior Surface of the Cerebral Hemisphere (Fig. 2C)

The lingual and fusiform gyri course through this areas separated by collateral sulcus. The inferior temporal sulcus separates the inferior temporal gyrus from the fusiform gyrus (Figs 5I and J).

The inferior aspects of the occipital lobe and the temporal lobe sit over the tentorium of the cerebellum. On the inferior (orbital) surface of frontal lobe the olfactory bulb and the olfactory tract over lie the olfactory sulcus which runs in the anteroposterior direction. Area medial to this is called gyrus rectus. Area lateral to olfactory sulcus is divided into four parts by a H-shaped sulcus into anterior, posterior, medial and lateral orbital gyri (Figs 5A and B).

BRAINSTEM AND CRANIAL NERVES

The brainstem comprises of midbrain, pons and medulla (Fig. 3A). The diencephalon connects the cerebral hemispheres to the mid brain and is made of thalamus, hypothalamus, subthalamus and epithalamus. The hypothalamus lies within the floor and lateral walls of the third ventricle. It extends from the lamina terminalis anteriorly to the caudal aspect of the mamillary bodies and includes the tuber cinereum which gives rise to the pituitary stalk (Fig. 6F).

Each thalamus is a large mass of gray matter in the lateral wall of the 3rd ventricle. It is bounded laterally by the posterior limb of the internal capsule and ventrally by the hypothalamic sulcus (Fig. 6G). The interthalamic adhesion projecting through the 3rd ventricle forms a medial connection with the opposite thalamus. The dorsolateral margin of the thalamus forms part of the floor of the lateral ventricle. The posterolaterally bulging portion of the thalamus is called the pulvinar (Fig. 5F). It overhangs medial and lateral geniculate bodies.

Ventral to the pulvinar lie the medial and lateral geniculate bodies on each side of midbrain, together called the metathalamus. They relay auditory and visual information to their respective receptor areas of cortex. The subthalamus is bounded by the hypothalamus anteriorly, the internal capsule laterally, and the thalamus above. The subthalamic nucleus integrates and relays connections from the globus pallidus and the thalamus.

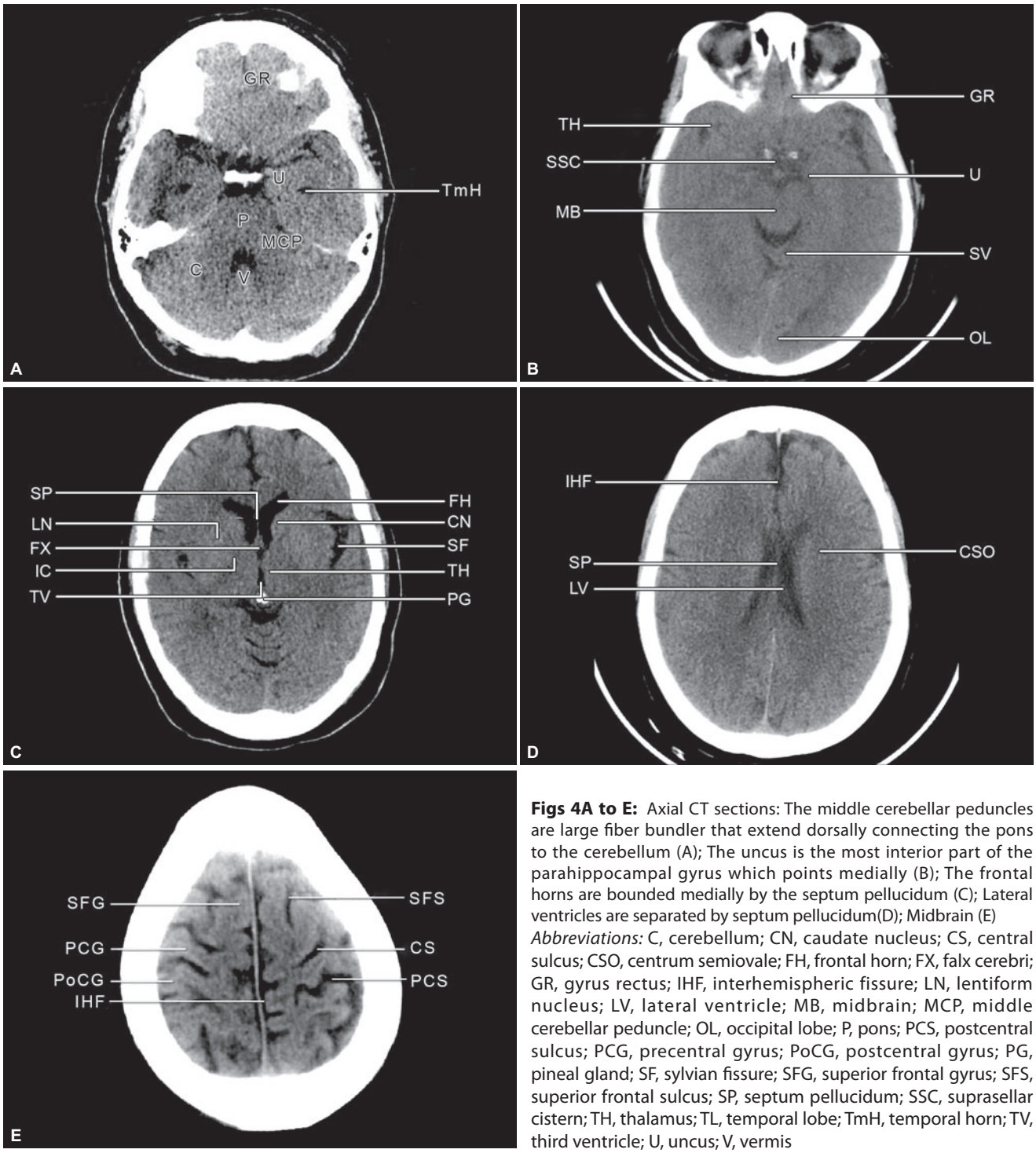

Figs 4A to E: Axial CT sections: The middle cerebellar peduncles are large fiber bundler that extend dorsally connecting the pons to the cerebellum (A); The uncus is the most interior part of the parahippocampal gyrus which points medially (B); The frontal horns are bounded medially by the septum pellucidum (C); Lateral ventricles are separated by septum pellucidum(D); Midbrain (E)
Abbreviations: C, cerebellum; CN, caudate nucleus; CS, central sulcus; CSO, centrum semiovale; FH, frontal horn; FX, falx cerebri; GR, gyrus rectus; IHF, interhemispheric fissure; LN, lentiform nucleus; LV, lateral ventricle; MB, midbrain; MCP, middle cerebellar peduncle; OL, occipital lobe; P, pons; PCS, postcentral sulcus; PCG, precentral gyrus; PoCG, postcentral gyrus; PG, pineal gland; SF, sylvian fissure; SFG, superior frontal gyrus; SFS, superior frontal sulcus; SP, septum pellucidum; SSC, suprasellar cistern; TH, thalamus; TL, temporal lobe; TmH, temporal horn; TV, third ventricle; U, uncus; V, vermis

The most dorsal division of the diencephalon, the epithalamus, includes the habenular nuclei, posterior commissure and pineal body. The structure is a part of limbic system.

The midbrain consists of a smaller dorsal portion the tectum and larger ventral portion, the cerebral peduncles (Fig. 6F). Aqueduct connecting the 3rd and 4th ventricles runs in the center of the junction of the tectum and cerebral peduncles (Fig. 3A). Each cerebral peduncle has a ventral part–the crus and a dorsal part—the tegmentum, separated by substantia nigra. The red nucleus, another pigmented nucleus is located posterior and medial to the substantia nigra

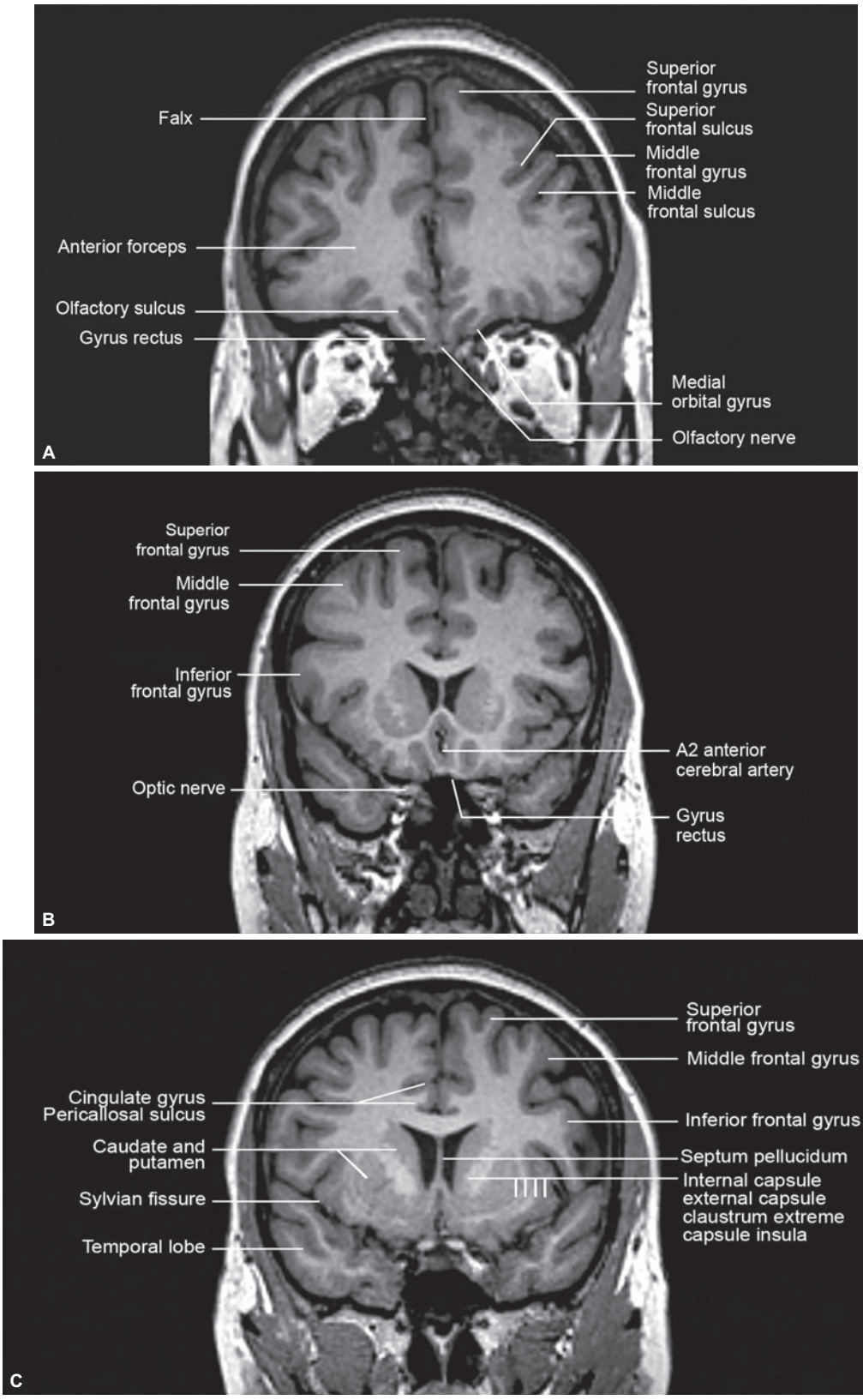
Superior frontal gyrus
Falx
Superior frontal sulcus
Middle frontal gyrus
Middle frontal sulcus
Anterior forceps
Olfactory sulcus
Gyrus rectus
Medial orbital gyrus
Olfactory nerve
A
Superior frontal gyrus
Middle frontal gyrus
Inferior frontal gyrus
A2 anterior cerebral artery
Optic nerve
Gyrus rectus
B
Superior frontal gyrus
Middle frontal gyrus
Cingulate gyrus
Pericallosal sulcus
Inferior frontal gyrus
Caudate and putamen
Septum pellucidum
Internal capsule
external capsule
claustrum extreme
capsule insula
Sylvian fissure
Temporal lobe
C

Figs 5A to C:

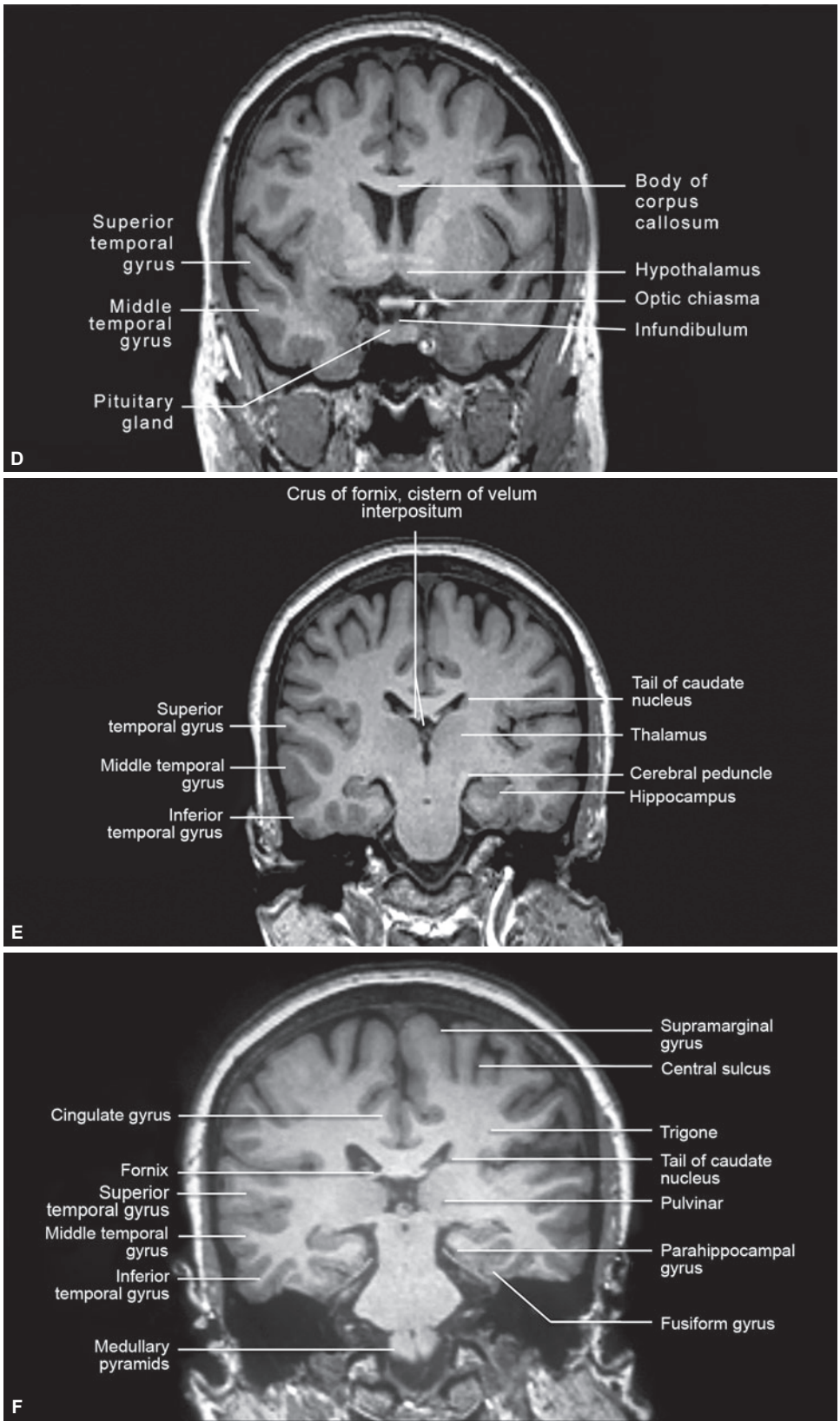
Body of corpus callosum
Superior temporal gyrus
Hypothalamus
Middle temporal gyrus
Optic chiasma
Infundibulum
Pituitary gland
D
Crus of fornix, cistern of velum interpositum
Tail of caudate nucleus
Superior temporal gyrus
Thalamus
Middle temporal gyrus
Cerebral peduncle
Hippocampus
Inferior temporal gyrus
E
Supramarginal gyrus
Central sulcus
Cingulate gyrus
Trigone
Fornix
Tail of caudate nucleus
Superior temporal gyrus
Pulvinar
Middle temporal gyrus
Parahippocampal gyrus
Inferior temporal gyrus
Fusiform gyrus
Medullary pyramids
F

Figs 5D to F:

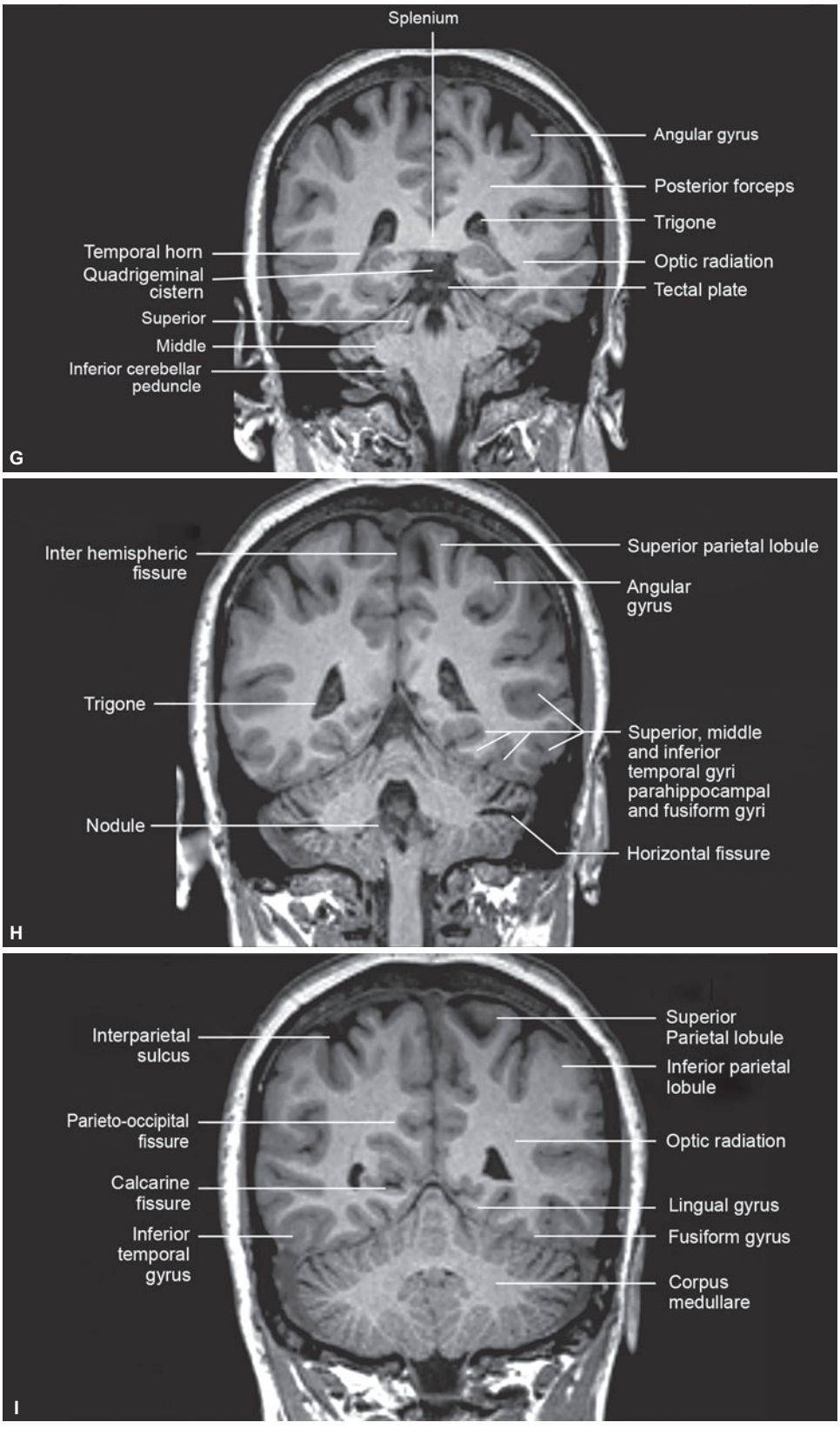
Splenium
Angular gyrus
Posterior forceps
Trigone
Temporal horn
Quadrigeminal cistern
Optic radiation
Tectal plate
Superior
Middle
Inferior cerebellar peduncle
G
Inter hemispheric fissure
Superior parietal lobule
Angular gyrus
Trigone
Superior, middle and inferior temporal gyri parahippocampal and fusiform gyri
Nodule
Horizontal fissure
H
Interparietal sulcus
Superior Parietal lobule
Inferior parietal lobule
Parieto-occipital fissure
Optic radiation
Calcarine fissure
Lingual gyrus
Inferior temporal gyrus
Fusiform gyrus
Corpus medullare
I

Figs 5G to I:

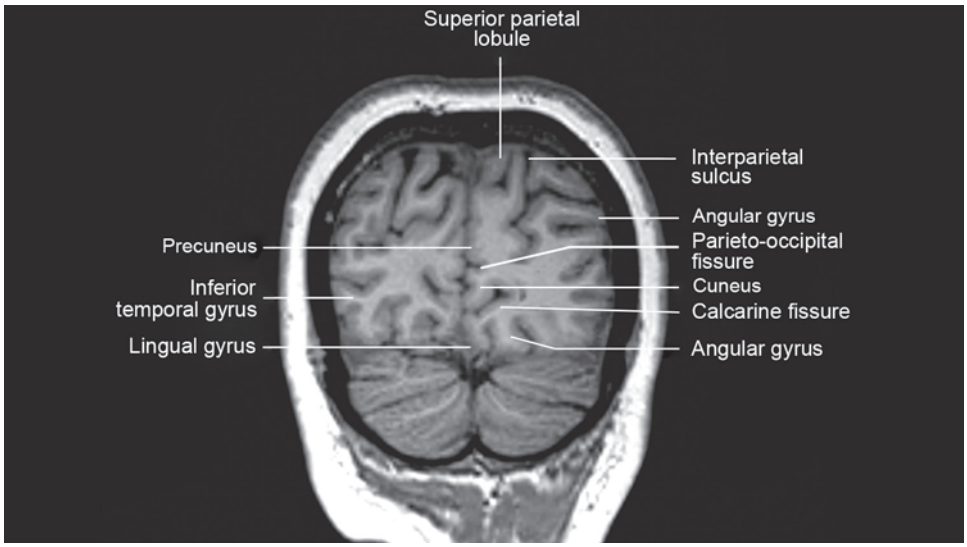

Fig. 5J:

Figs 5A to J: (A and B) Coronal MR sections anterior to the frontal horn. The entire slice contains frontal lobe. The olfactory nerve nestles between the gyrus rectus and medial orbital gyrus on the cribriform plate. (A) The more anterior section shows a continuous interhemispheric fissure which is; (B) Interrupted by corpus callosum on a more posterior section. The optic strut separates the optic nerve from superior orbital fissure; (C and D) Coronal MR sections through the frontal horn. The frontal horns are outlined by corpus callosum and caudate nucleus. The internal capsule, putamen, external capsule, claustrum and insula can be seen from medial to lateral. The two columns of fornix outline the foramen of Monro with septum pellucidum above it separating the two frontal horns. Optic chiasma can be identified above the pituitary gland and its infundibulum. In the parasellar area, the cavernous sinuses containing third, fourth, fifth and sixth nerves are outlined by low intensity dura; (E) Coronal MR sections at the third ventricle level. Mid third of the lateral convexity is parietal lobe and lower third is temporal lobe. Corpus callosum lies at the bottom of the interhemispheric fissure. The lateral ventricles (with crus fornix on its superior medial part) and third ventricle are seen more inferiorly. The interpeduncular fossa is seen as a CSF space below third ventricle. The tail of caudate nucleus lies on the lateral aspect of lateral ventricle. The medial temporal lobe consists of hippocampus with overlying choroid fissure; (F) Coronal MR sections through the body of lateral ventricle. This section cut through the splenium of corpus callosum with the cingulate gyrus lying just above it. Below it lie the quadrigeminal plate (tectum) and its cistern. The sections pass through the mid brain, pons and medulla. The lateral convexity consists entirely of parietal and temporal lobes; (G and H) Coronal MR sections through the trigone and occipital horns. Superior two-thirds of the lateral convexity of brain at this level consists of superior and inferior parietal lobules. The lower third belongs to the temporal lobe. The inferior surface of temporal lobe consists of parahippocampal, fusiform and inferior temporal gyri; (G) The section through trigones cuts the cerebellar peduncles while; (H) A more posterior section shows the cerebellar hemispheres, vermis and the tonsils; (I and J) Coronal MR sections posterior to the occipital horn. The interhemispheric fissure completely divides the two cerebral hemispheres. The lingual, fusiform and inferior temporal gyri are clearly identified. The precuneus and cuneus are separated by parieto-occipital fissure and between the cuneus and lingual gyrus lies the calcarine fissure

on each side. Pars compacta separates the substantia nigra and red nucleus (Fig. 6L). The tectum consists of four rounded prominences – the two superior colliculi and two inferior colliculi or corpora quadrigemina. Each superior colliculus is connected to the *ipsilateral lateral* geniculate body through the superior brachium, where the optic tract ends. Similarly, the inferior colliculi are connected to the medial geniculate bodies through the inferior brachium thereby connecting it to the auditory cortex (Fig. 6F).

The oculomotor nerves (CN III) exit from the caudal aspect of the interpeduncular fossa (Fig. 7A). The paired trochlear nerves (CN IV) emerge from the dorsal surface of the brainstem caudal to the inferior colliculi, and wrap around the lateral aspects of the midbrain. The ventral and dorsal aspects of the cerebral peduncles are separated by semilunar substantia nigra with red nuclei on its dorsomedial aspect (Fig. 6L).

The pons has a bulging ventral surface with a shallow midline basal sulcus. The middle cerebellar peduncles are large fiber bundles that extend dorsally connecting the pons to the cerebellum (Fig. 4A). Emerging from the lateral aspect of the pons are the trigeminal nerves (CN V) (Fig. 7B), while the paired paramedian abducens nerves (CN VI) exit ventrally from the pontomedullary junction. The facial nerves (CN VII) and the vestibulocochlear nerves (V III) emerge from the lateral aspect of the pontomedullary junction and pass through the cerebellopontine angle cistern (Fig. 7C).

The medulla oblongata connects the midbrain and the spinal cord. It measures 3 cm in length and 2 cm in width. On the ventral aspect of the medulla the paramedian pyramids

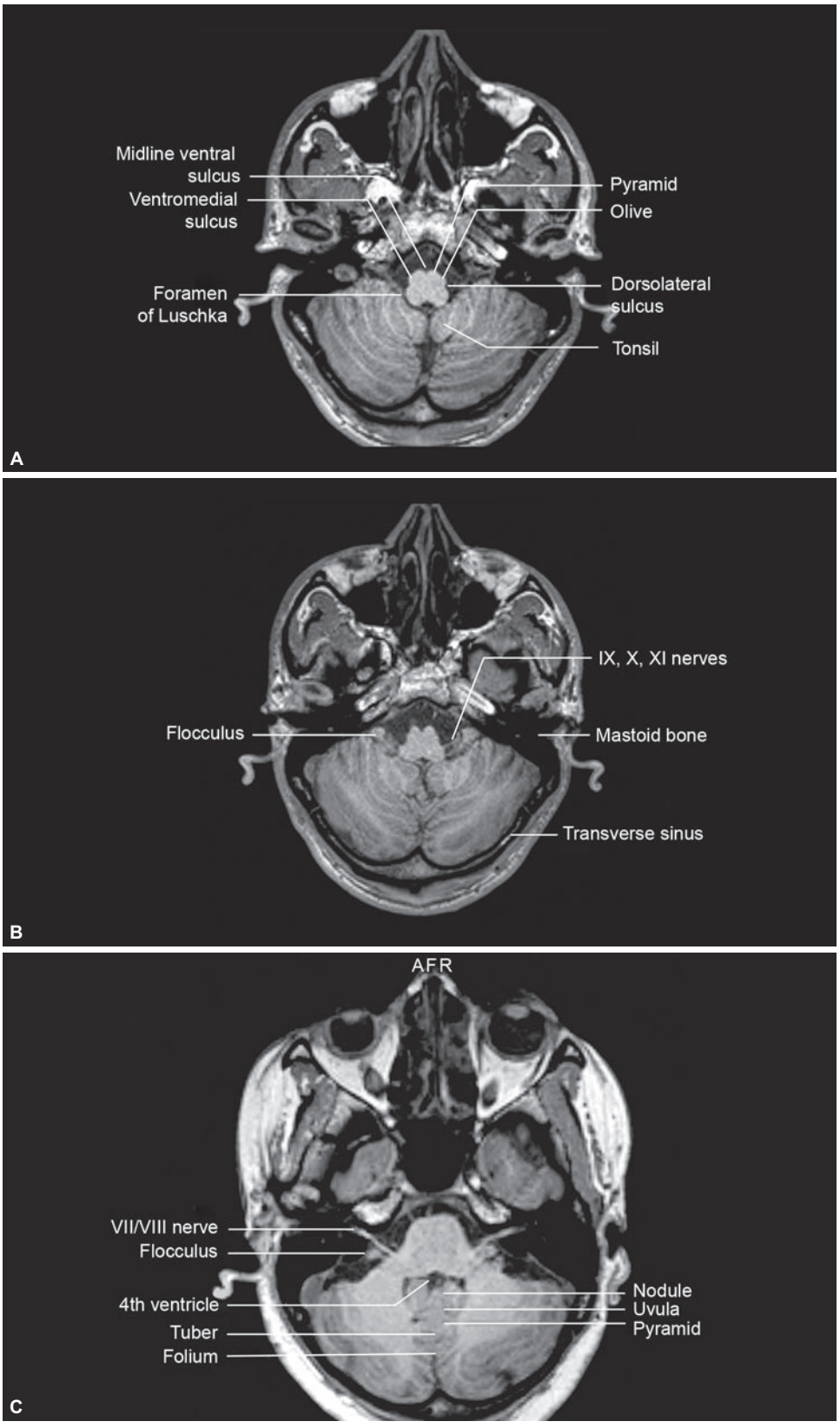
Midline ventral sulcus
Ventromedial sulcus
Foramen of Luschka
Pyramid
Olive
Dorsolateral sulcus
Tonsil
A
IX, X, XI nerves
Flocculus
Mastoid bone
Transverse sinus
B
AFR
VII/VIII nerve
Flocculus
4th ventricle
Tuber
Folium
Nodule
Uvula
Pyramid
C

Figs 6A to C:

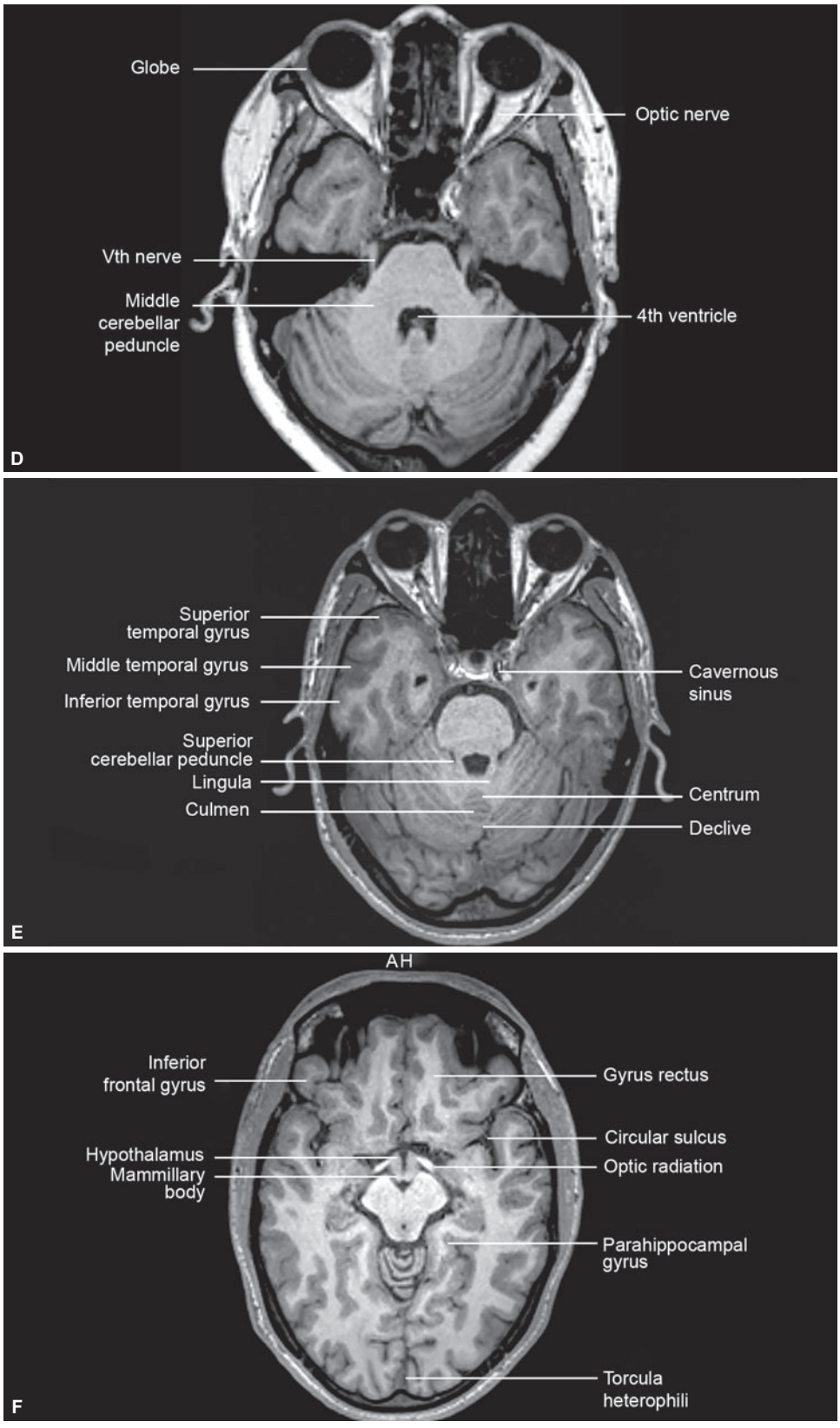
Globe
Optic nerve
Vth nerve
Middle cerebellar peduncle
4th ventricle
D
Superior temporal gyrus
Middle temporal gyrus
Inferior temporal gyrus
Superior cerebellar peduncle
Lingula
Culmen
Cavernous sinus
Centrum
Declive
E
AH
Inferior frontal gyrus
Gyrus rectus
Circular sulcus
Hypothalamus
Mammillary body
Optic radiation
Parahippocampal gyrus
Torcula heterophili
F

Figs 6D to F:

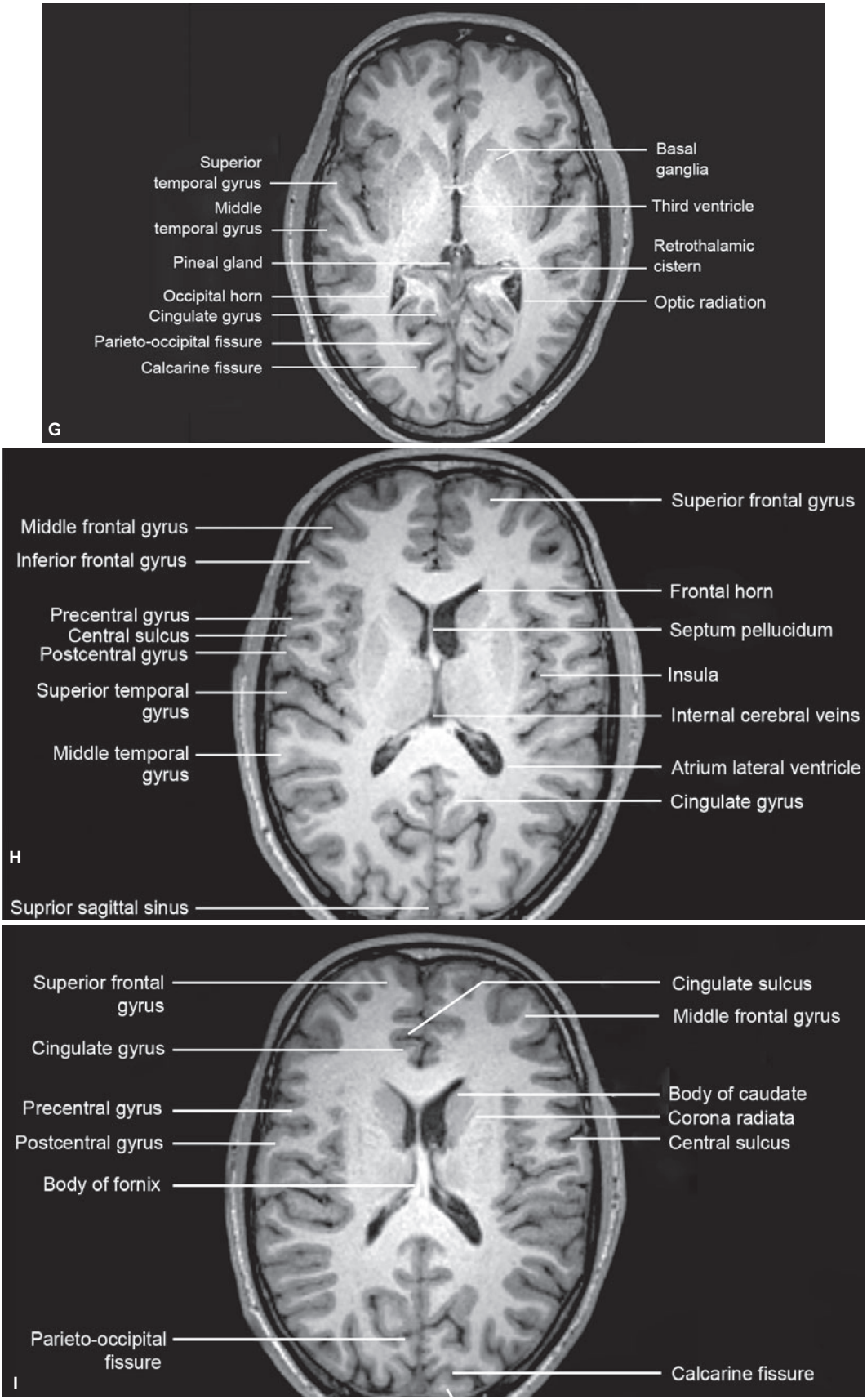
Superior temporal gyrus
Middle temporal gyrus
Pineal gland
Occipital horn
Cingulate gyrus
Parieto-occipital fissure
Calcarine fissure
Basal ganglia
Third ventricle
Retrothalamic cistern
Optic radiation
G
Middle frontal gyrus
Inferior frontal gyrus
Precentral gyrus
Central sulcus
Postcentral gyrus
Superior temporal gyrus
Middle temporal gyrus
Suprior sagittal sinus
Superior frontal gyrus
Frontal horn
Septum pellucidum
Insula
Internal cerebral veins
Atrium lateral ventricle
Cingulate gyrus
H
Superior frontal gyrus
Cingulate gyrus
Precentral gyrus
Postcentral gyrus
Body of fornix
Parieto-occipital fissure
Cingulate sulcus
Middle frontal gyrus
Body of caudate
Corona radiata
Central sulcus
Calcarine fissure
I

Figs 6G to I:

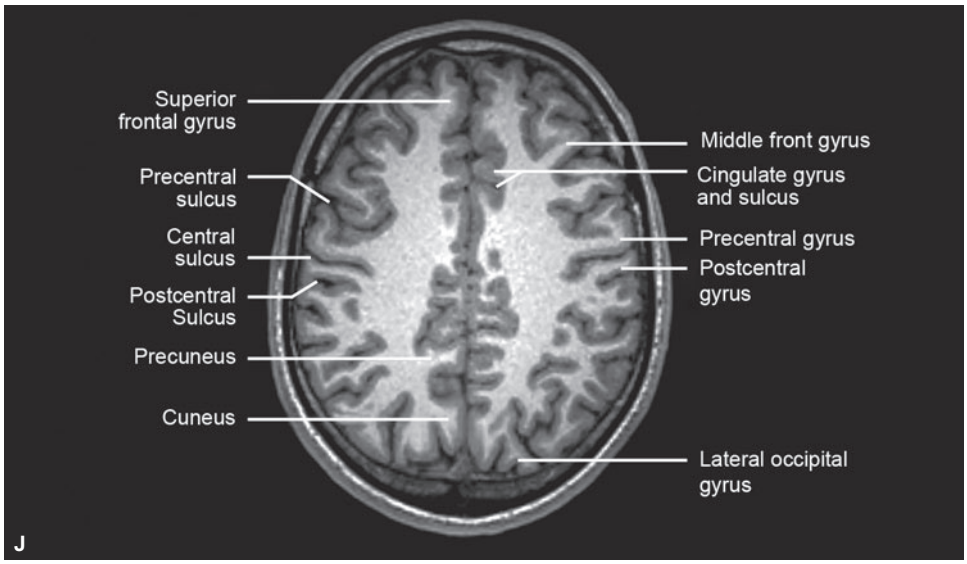
Superior frontal gyrus
Precentral sulcus
Central sulcus
Postcentral Sulcus
Precuneus
Cuneus
Middle front gyrus
Cingulate gyrus and sulcus
Precentral gyrus
Postcentral gyrus
Lateral occipital gyrus
J

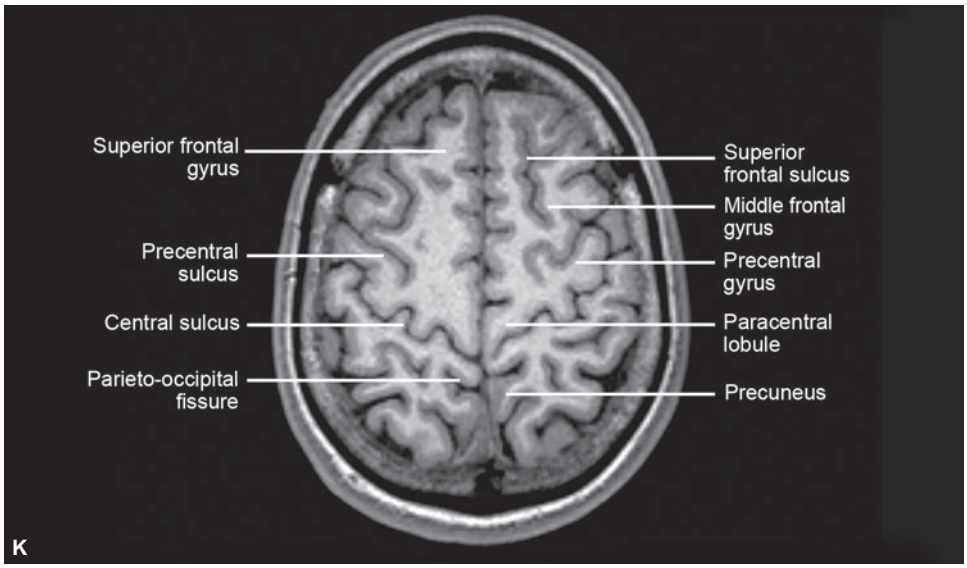
Superior frontal gyrus
Precentral sulcus
Central sulcus
Parieto-occipital fissure
Superior frontal sulcus
Middle frontal gyrus
Precentral gyrus
Paracentral lobule
Precuneus
K

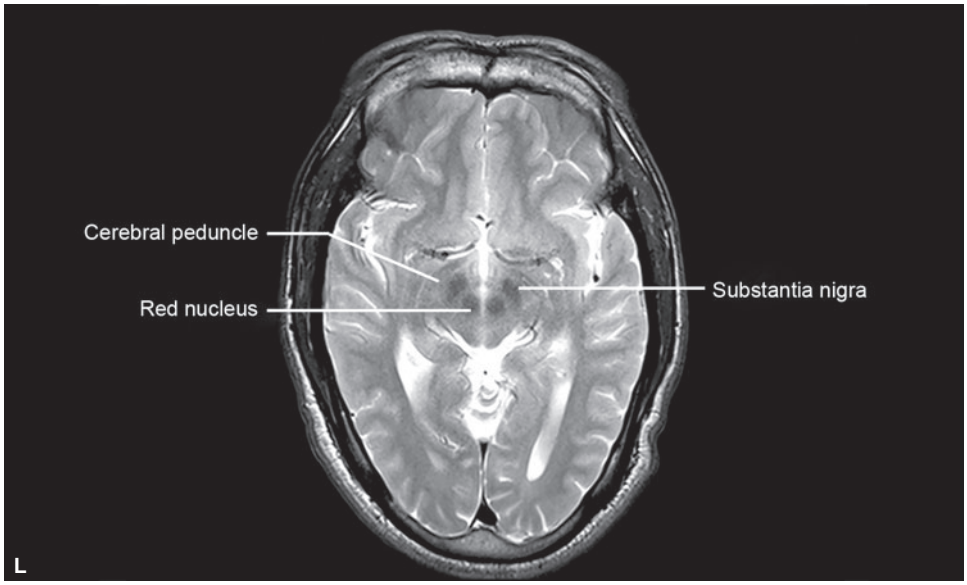
Cerebral peduncle
Red nucleus
Substantia nigra
L

Figs 6J to L:

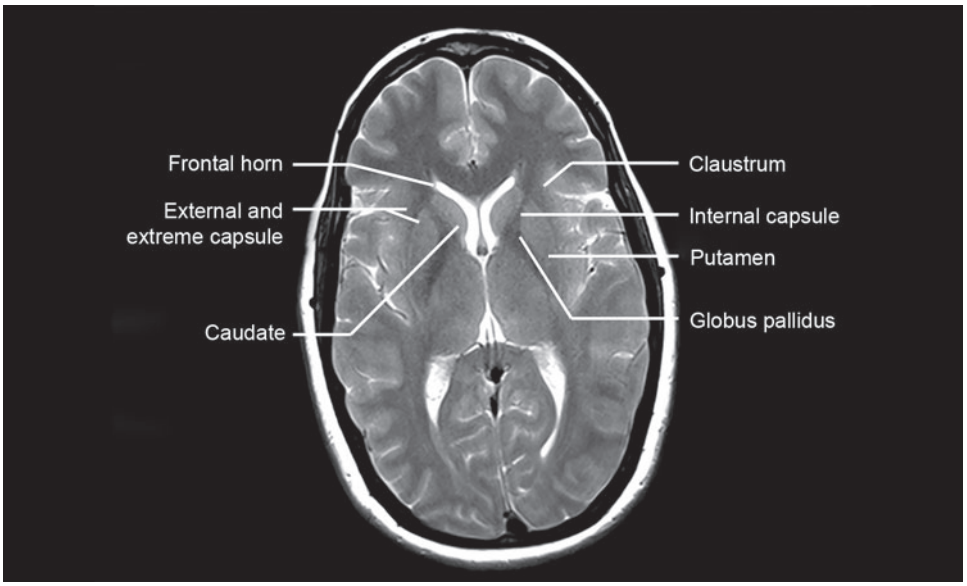

Fig. 6M:

Figs 6A to M: (A) T1-weighted axial MR section at the level of medulla shows the midline ventral sulcus, pyramids and olives separated by ventromedial sulcus. Dorsolateral sulcus is seen posterior to olives. Cerebellar tonsils are seen posterolateral to the medulla. Vallecula is seen posteriorly. Fourth ventricle with foramen of Luschka is seen posterior to medulla; (B) T1-weighted axial MR section at slightly higher level than Figure 6A shows the IX, X and XI cranial nerves seen as a common bundle exiting from the dorsolateral sulcus; (C) T1-weighted axial MR section through the pons. Pons is seen in front of the fourth ventricles. The CP angle cisterns lie lateral to the pons. Seventh and eight cranial nerves course through the cistern anterior to flocculus towards internal auditory canals. The inferior vermis and its various divisions are well seen; (D) T1-weighted axial MR section through middle part of fourth ventricle. Middle cerebellar peduncles connecting the pons with cerebellar hemispheres are well seen. Fifth nerves are seen emerging from the lateral surface of pons on both sides. Also seen are globes with optic nerve and lower part of temporal lobes; (E) T1-weighted axial MR section through the midbrain shows the superior cerebellar peduncles, and the parts of superior vermis. Anteriorly the olfactory nerve and gyrus rectus on each side of inter-hemispheric fissure are seen clearly. The structures of the middle cranial fossa-cavernous sinus, both temporal lobes with superior, middle and inferior temporal gyri, are also seen; (F) T1-weighted axial MR section at the level of midbrain. Inferiorly frontal and temporal lobes are seen separated by sylvian fissure. V shaped tentorium outlining the superior vermis is seen with quadrigeminal plate and cistern located anterior to it. Parahippocampal gyrus and fusiform gyrus course forward from occipital pole to midbrain. Anterior to midbrain, mammillary bodies, optic radiations and hypothalamus are seen; (G) T1-weighted axial MR section at the level of lower third ventricle shows the basal ganglia, internal capsule, thalami and retrothalamic cistern. Peripherally superior temporal and middle temporal gyri are seen posterior to sylvian fissure. Frontal horns of lateral ventricles are seen anteriorly and occipital horns posteriorly. Pineal gland is seen posterior to the third ventricle. Optic radiations are seen ending in the occipital cortex. Also seen is the Y-shaped parietooccipital fissure and calcarine fissure, the later forming the lateral boundary of lingual gyrus; (H) T1-weighted axial MR section at the level of mid-3rd ventricle showing various parts of frontal lobe, anteriorly and occipital lobes posteriorly. In the mid line genu of the corpus callosum is seen anteriorly connecting the frontal lobes. Septum pellucidum is seen separating the frontal horns of lateral ventricles. Posteriorly in the mid line splenium of the corpus callosum is seen forming posterior wall of 3rd ventricle and medial wall of atria of lateral ventricle. Peripherally the central sulcus is seen separating the frontal (precentral) and parietal (postcentral) lobes. The sylvian fissure separates the parietal lobe (post central gyrus) from the temporal lobe (superior temporal gyrus). In the depth of the sylvian fissure, portions of frontal, parietal and temporal lobe form the insula; (I) T1-weighted axial MR section at the superior part of 3rd ventricle shows the superior frontal gyrus and middle frontal gyrus separated by superior frontal sulcus. Body of fornix is seen anterior to 3rd ventricles which separate the lateral ventricles. The other structures seen in Figure 6H are also seen; (J and K) T1-weighted axial MR section at supraventricular level show the deep white matter of cerebral hemispheres, the centrum semiovale. The central sulcus characteristically dips posteriorly and leads to paracentral lobule. Posterior to it the precuneus and cuneus are separately seen. Only superior and middle frontal gyri are seen at this level; (L) T2-weighted axial MR section at midbrain level. Semilunar band of pigmented gray matter anteriorly—the substantia nigra, appears hypointense. Another area of hypointensity is seen dorsomedial to substantia nigra called the red nucleus. The substantia nigra and red nuclei are separated by pars compacta; (M) T2-weighted axial MR section at the level of basal ganglia. Slit like third ventricle in midline is flanked by thalamus on each side. The interhemispheric fissure anteriorly separates the two frontal lobes. Medial to the sylvian fissure, lie the insular cortex and external capsule. The caudate and lentiform nuclei with intervening internal capsule lie medially. Globus pallidus appears hypointense in comparison to putamen on T2-weighted images. Claustrum—a strip of gray matter lies between the external and extreme capsule

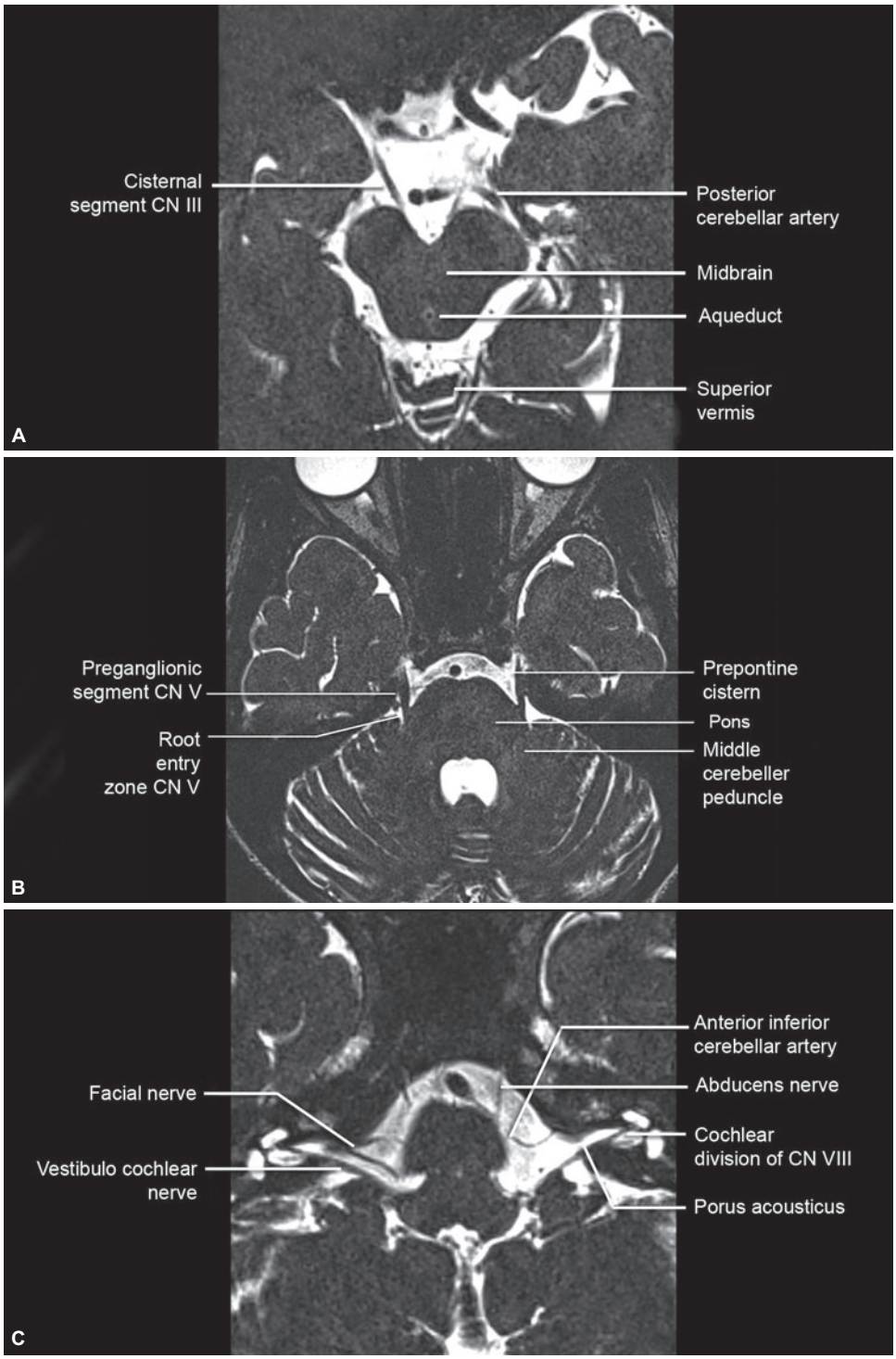
Cisternal segment CN III
Posterior cerebellar artery
Midbrain
Aqueduct
Superior vermis
A
Preganglionic segment CN V
Root entry zone CN V
Prepontine cistern
Pons
Middle cerebeller peduncle
B
Anterior inferior cerebellar artery
Facial nerve
Abducens nerve
Vestibulo cochlear nerve
Cochlear division of CN VIII
Porus acousticus
C

Figs 7A to C:

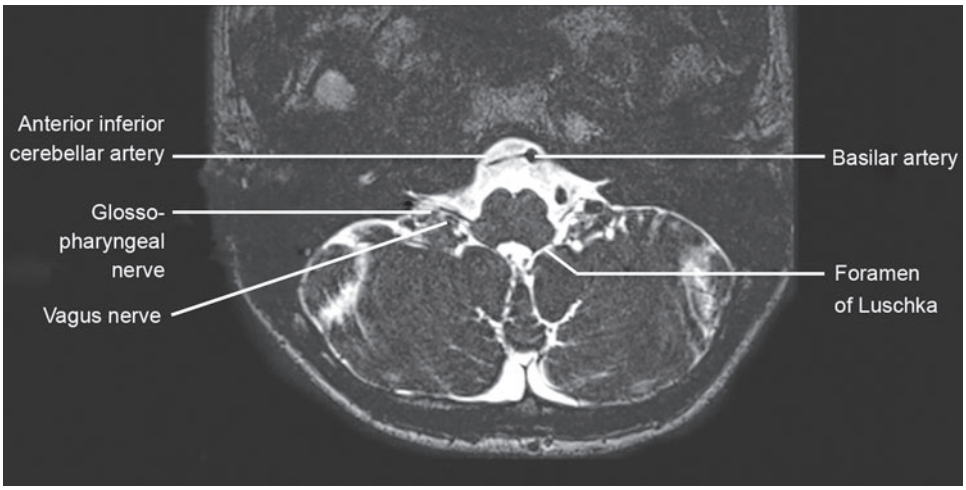

Fig D:

Figs 7A to D: Axial MR cisternography sections using SPACE technique through (A) Midbrain; (B and C) Pons; and (D) Medulla show III, V, VI, VII, VIII, IX and X cranial nerves in relation to brainstem as labeled

form longitudinal protrusions on each side of the ventral median fissure. The paired ventrolateral sulci separate the medullary pyramids and the inferior olives (Fig. 6A). The hypoglossal nerves (CN XII) emerge from the ventrolateral sulci. The rootlets of the glossopharyngeal (CN IX), vagus (CN X) and spinal accessory (CN XI) nerves exit from the dorsolateral sulcus which is located further laterally (Fig. 7D). The paired cuneate and gracilis tubercles form longitudinal ridges on the dorsal aspect of the medulla oblongata just caudal to the fourth ventricles separated by posterior median sulcus.

CEREBELLUM

The cerebellum lies posterior to the pons and medulla. The superior, middle, and inferior cerebellar peduncles connect the cerebellum to midbrain, pons and medulla respectively. The narrowest leaf-like subdivisions of the cerebellar cortex are termed folia. The cerebellum consists of the midline cerebellar vermis connecting the paired lateral hemispheres. The hemisphere is divided into anterior lobe, middle lobe and flocculonodular lobe by deep fissures named primary fissure and posterolateral fissure (Figs 3D and 5H). A deep horizontal fissure divides it into superior and inferior halves. Caudal to the inferior vermis and between the cerebellar tonsils is the vallecula (Fig. 6A) which communicates with the fourth ventricle through the foramen of magendie. The superior divisions of the vermis are lingula, centrum, culmen, declive and folium (Fig. 6E). The inferior divisions are tuber, pyramid, uvula and nodule (Fig. 6C). Immediately caudal to the inferior medullary velum is the nodulus of the vermis. The flocculus projects into the cerebellopontine angle cistern ventral to the inferior cerebellar peduncle (Fig. 6B). The deep cerebral nuclei are laterally placed dentate and medially placed paired emboliform, globose and fastigial nuclei.

WHITE MATTER OF THE CEREBRUM

The fiber connections of the cerebral cortex are divisible into three major groups (Figs 8A to E). Projection fibers are corticospinal, corticobulbar, corticopontine and cortico-thalamic tracts. Association fibers consist of subcortical U fibers, long projection fibers of cingulum, superior/inferior longitudinal fasciculi, uncinate fasciculus and superior/inferior occipitofrontal fasciculi. The commissural fibers interconnecting the two hemispheres are corpus callosum, anterior and posterior commissure, hippocampal/habenular commissures and the hypothalamic commissure. The common central mass of white matter is known as the centrum semiovale (Fig. 4D). Projection fibers passing through the corona radiata converge to form the internal capsule consisting of anterior and posterior limbs and the genu (Figs 6M and 4C).

The columns of fornix which lie on either side of the foramen of Monro continue posteriorly as body of fornix. It is a C-shaped bundle of white matter forming the roof of III ventricle. Posteriorly it divides into the two crura which continue into the fimbria and alveus of hippocampal formation (Fig. 2B). This is part of limbic system concerned with emotional and sexual behavior and recent memory.

VENTRICLES AND CISTERNS

The ventricular system consists of lateral, third, fourth ventricles and the cerebral aqueduct. The lateral ventricles communicate with the third ventricle by the foramen of

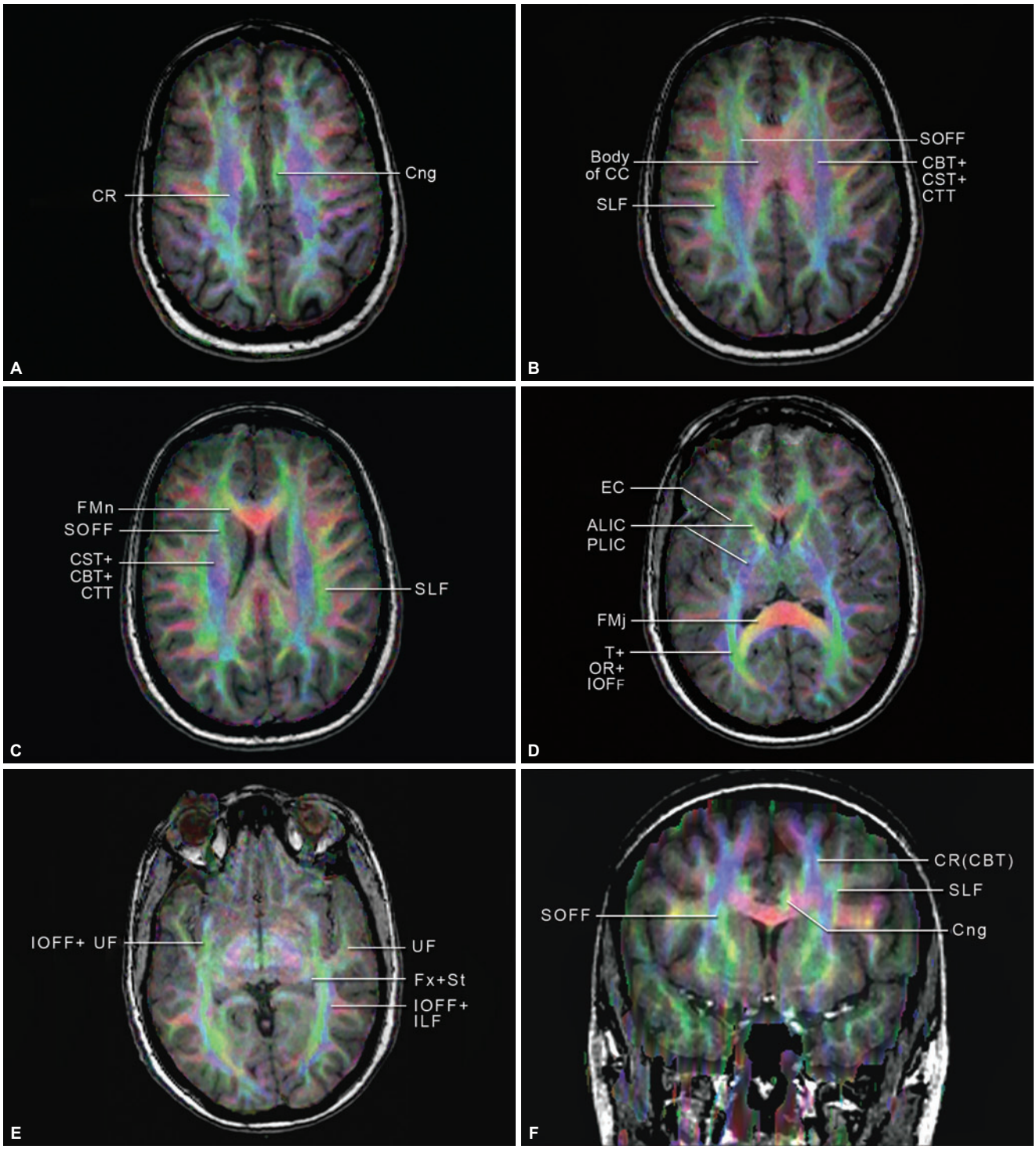
CR
Cng
A
Body of CC
SLF
SOFF
CBT+ CST+ CTT
B
FMn
SOFF
CST+ CBT+ CTT
SLF
C
EC
ALIC PLIC
FMj
T+ OR+ IOFF
D
IOFF+ UF
UF
Fx+St
IOFF+ ILF
E
SOFF
CR(CBT)
SLF
Cng
F

Figs 8A to F:

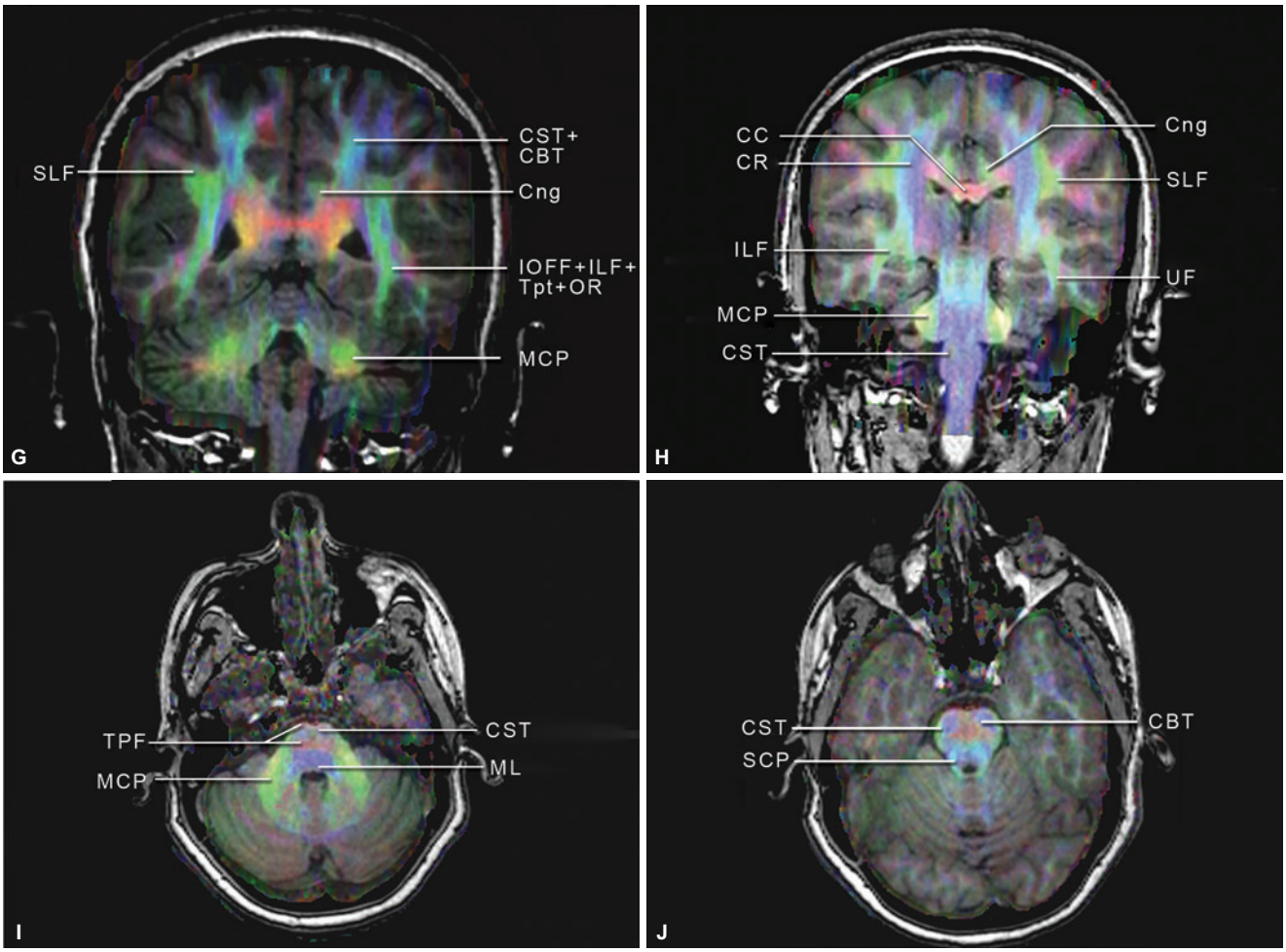

Figs 8G to J:

Figs 8A to J: Fractional anisotropy maps superimposed on T1 weighted images of brain showing the white matter tracts
Abbreviations: ALIC, anterior limb of internal capsule; CBT, corticobulbar tract; Cng, cingulum; CR, corona radiate; CST, corticospinal tract; CTT, corticothalamic tract; FMj, forceps major; FMn, forceps minor; Fx, fornix; ILF, inferior longitudinal fasciculus; IOFF, inferior occipitofrontal fasciculus; MCP, middle cerebellar peduncles; ML, medial lemniscus; OR, optic radiation; PLIC, posterior limb of internal capsule; SCP, superior cerebellar peduncle; SLF, superior longitudinal (arcuate) fasciculus; SOFF, superior occipitofrontal fasciculus; St, stria terminalis; TPF, transverse pontine fibers; Tpt, tapetum; UF, uncinate fasciculus

Monro while the third ventricle communicates with the fourth ventricle via the aqueduct of Sylvius.

The lateral ventricles consist of frontal horns, body, trigone, occipital and temporal horns. Foramen of Monro defines the junction between frontal horns and body of lateral ventricles and the splenium of corpus callosum arbitrarily separates the body from the trigone. The frontal horns are bounded medially by the septum pellucidum (Fig. 4C), inferiorly and laterally by the head of the caudate nucleus, and superiorly and anteriorly by the corpus callosum. The body is bounded superiorly by the corpus callosum, inferiorly by caudate nucleus and the thalamus, medially by the fornix and laterally by the body of the caudate nucleus (Fig. 5E). The trigone contains large tuft of choroid plexus called glomus (Fig. 5H).

The third ventricle is bounded laterally by the thalami, inferiorly by the hypothalamus (Figs 5D and E), anteriorly by the anterior commissure and lamina terminalis, posteriorly by the epithalamus and posterior commissure, and superiorly by the cistern of the velum interpositum and body of the fornix. The inferior aspect of third ventricle has downward invaginations called optic, infundibular recesses anteriorly and, suprapineal and pineal recesses posteriorly.

The fourth ventricle is rhomboid in shape and lies between the pons and cerebellum. It communicates above with the third ventricle via the aqueduct and with subarachnoid

space through posterior midline foramen of magendie and posterolateral foramina of Luschka (Fig. 6A).

The major cisterns at the base of the brain are suprasellar cistern, perime-sencephalic cistern, prepontine and perimedullary cisterns and the cerebellopontine angle cistern. The suprasellar cistern is a five pointed CSF space, communicating anteriorly with interhemispheric fissure, laterally with sylvian fissure and posteriorly with perimesencephalic cistern. It contains optic chiasma, internal carotid artery and circle of Willis and pituitary stalk (Fig. 4B).

The perimesencephalic cistern consists of interpeduncular, crural, ambient and quadrigeminal plate cisterns lying along the anterior, anterolateral, posterolateral and posterior aspects of the midbrain respectively. The upper end of basilar artery and the III cranial nerve lie within the interpeduncular cistern. Intimately related to the quadrigeminal plate cistern (Fig. 5G) are the pineal gland and the vein of galen. The fourth cranial nerves course in the ambient cisterns around the midbrain.

The cerebellopontine angle cistern (Figs 5C, 7B and C) is bounded medially by the middle cerebellar peduncle and the anteroinferior surface of the cerebellum and laterally by the temporal bone. It contains VII/VIII cranial nerves and anterior inferior cerebellar arteries. Prepontine cistern (Fig. 7B and C) lies anterior to the pons and contains basilar artery. The perimedullary cisterns surround the medulla and contain lower cranial nerves (CN IX, X and XI) and vertebral arteries (Fig. 7D). Superior cerebellar cistern lies superior to the cerebellum and contains vein of Galen. The cisterna magna is a CSF space at the posteroinferior aspect of cerebellum and may be sometimes very large in normal people.

GRAY MATTER NUCLEI AND ADJACENT STRUCTURES

Basal ganglia represent central gray matter consisting of corpus striatum (caudate nucleus and lentiform nucleus) and claustrum a strip of gray matter lateral to the lentiform nucleus and amygdala at the roof of temporal horn. The caudate nucleus has a larger head anteriorly and a narrow posterior part the tail, which follows the superolateral border of thalamus and the temporal horn into the amygdala. The lentiform nucleus is wedge shaped and comprised of globus pallidus medially and putamen laterally. External capsule, claustrum, extreme capsule and insular cortex lie lateral to the putamen in that order (Fig. 5C). The internal capsule is bounded anteromedially by caudate head, laterally by lentiform nucleus and posteromedially by thalamus (Figs 6G and M).

SUGGESTED READING

1. Atlas S (Ed). Magnetic Resonance Imaging of the Brain and Spine, 4th edition. Philadelphia: Lippincott Williams & Wilkins. 2009.
2. Berry M, Standring SM, Bannister LH. Nervous system. In: Susan Standring (Ed): Gray's Anatomy, 40th edition—The Anatomical Basis of Clinical Practice, New York: Elsevier, Churchill Livingstone. 2008.
3. Butler P, Jeffiree MA. The skull and brain. In: Butler P, Mitchell AWM, Ellis H (Eds). Applied Radiological Anatomy, 1st edition. Cambridge University Press. 2001. pp. 17-60.
4. Lee SH, Rao KCVG, Zimmerman RA (Eds). Normal Anatomy in Cranial MRI and CT, 4th edition. New York: McGraw Hill Inc. 1999. pp.105-37.
5. Patel VH, Friedman L. MRI of the brain: Normal Anatomy and Normal Variants, 1st edition, Philadelphia: WB Saunders Company. 1997.
6. Scott WR, Hanaway J. Correlative anatomy of the brain. In: Radiology-diagnosis-imaging-intervention Vol 3, Philadelphia: JB Lippincott Co. 1986.
7. Snell RS (Ed). Snell's Textbook of Clinical Anatomy, 7th edition. Boston: Little Brown and Company. 2004. pp. 790-830.

3
CHAPTER

Normal Cerebral Angiography

Shailesh B Gaikwad, Ajay Kumar

PART 1: CEREBRAL ANGIOGRAPHY TECHNIQUE

INTRODUCTION

This is an important albeit invasive procedure wherein most cases of suspected vascular pathologies baring few exceptions are diagnosed. It is a direct examination of the blood vessels that provide not only the information of the vascular anatomy but also the flow dynamics.

Historical Background

Within months of Karl Roentgen's discovery of X-rays, an angiographic study of an amputated arm was conducted successfully in Vienna using the Teichmann mixture of lime, mercuric sulfide, and petroleum.

Definition

It is the demonstration of the vascular anatomy by direct injection of the iodinated contrast medium into the vessel.

Six Vessel Angiography

It includes the study of the following vessels:
1. Right internal carotid artery
2. Left internal carotid artery
3. Right external carotid artery
4. Left external carotid artery
5. Right vertebral artery
6. Left vertebral artery.

Indications

- Primary vascular diseases
  - Vaso-occlusive diseases
  - Aneurysms
  - Ateriovenous malformations
  - Ateriovenous fistula
- Vascular assessment of tumors
- Source of hemorrhage
- Congenital vascular condition
- Interventional procedure

Contraindications

- Bleeding disorders
- Thrombogenic condition
- Skin infection
- Abnormal renal function
- Cardiac condition (CCF)
- Allergy to iodinated contrast agents
- Pregnancy
- Nonpalpable pulse.

Patient Preparation

Careful history taking is very important part before most of the procedure. It is advisable to take informed consent from the patient in case of elective procedure and from relatives in case of emergency. Patient should be well hydrated along with four hour fasting before the procedure. Part preparation includes shaving of both the groins. It is recommended to obtain the xylocaine sensitivity test. Patient must have passed urine before the procedure.

Requirement

- DSA machine (Figs 1A and B)
- Catheterization equipment (Fig. 2)
- Disposables.

Catheterization Equipment

Cleaning agents, blade no. 11, puncture needle, vascular sheath, mini-guidewire, various catheters, Terumo guidewire, syringes.

Figs 1A and B: DSA biplane machine with monitors

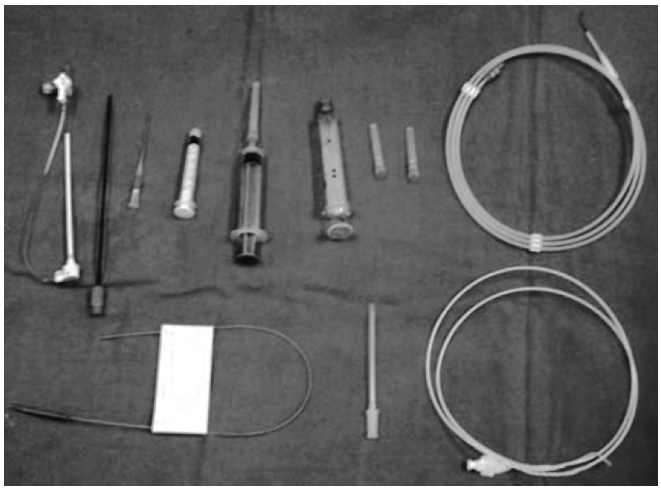

Fig. 2: Instruments required: (left to right) Sheath, dilator, puncture needle, syringes, terumo wire, short guidewire, single puncture needle, catheter

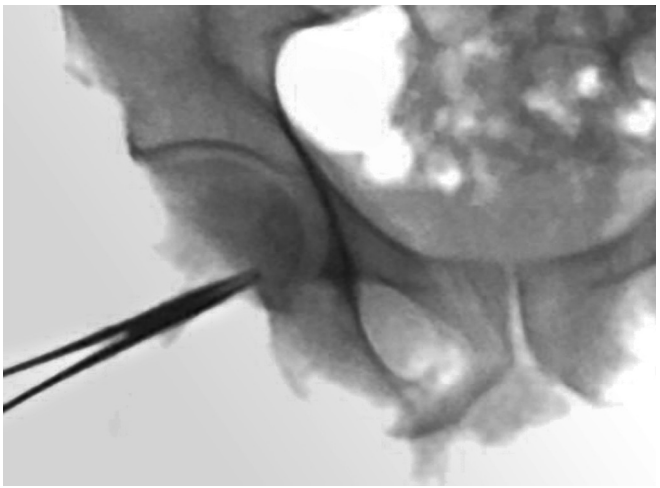

Fig. 3: Marking the site of puncture on fluoroscopy

Site of the Puncture

If the femoral pulsations are good in the groins, then access is usually through the right femoral artery. Palpate the site of the puncture and feel the inguinal ligament along the ASIS and pubic symphysis. Inguinal ligament is 1–2 cm below the site of the palpation. Puncture over middle of medial 3rd of femoral head (Figs 3 and 4).

Preparation

Sterilize the site first with savalon, then with betadine and with spirit in the last.

Wipe with sterilized gauze piece.

Local Anesthesia

For local anesthesia, give subcutaneous injection of 2% xylocaine without adrenaline. Palpate the artery with index, mid and ring finger of the left hand. Infiltrate 2–3 mL each on the either side of the artery. Care must be taken to not to inject LA into the vessel, before giving injection always check by withdrawing to rule out arterial puncture. Give injection slowly for the patient comfort (Fig. 5).

Artery Puncture

- Give 3 mm wide and 3 mm deep, superficial skin incision at the puncture site by using 11 no. blade. It is ideal to check the site under fluoroscopy before arterial puncture.

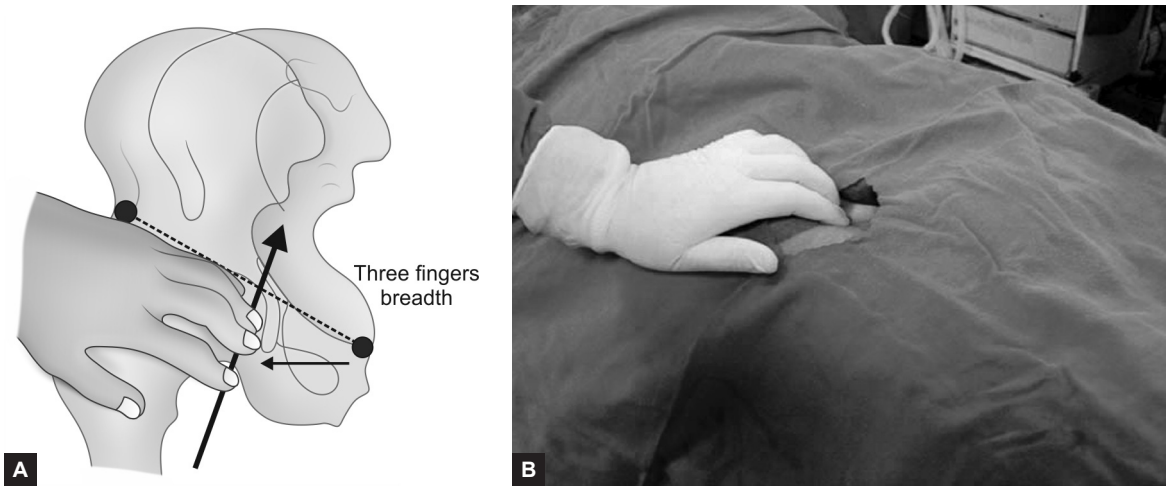

Figs 4A and B: Localization and palpation of femoral artery

Fig. 5: Infiltrating local anesthetic at the site of puncture

Fig. 6: Arterial puncture

- **Seldinger technique:** Palpate femoral artery by the index, middle and ring finger, of the left hand. Take Medicut (puncture needle with needle inside and plastic canula outside) in the right hand and advance towards the artery at about 45 degree angle. Feel the pulse of the artery through the needle in the right hand and as one feel it over femoral artery, enter artery with a jab (Fig. 6). Remove the needle and slowly withdraw the canula till the jet of the blood is obtained. Rule out venous puncture (blood will not come out in jets). After confirming arterial access introduce mini-guidewire, and remove the canula. Then introduce arterial sheath over the short guidewire.
- Again check the position of the sheath by withdrawing blood using syringe. Arterial blood will come into syringe in pulsatile manner and with thrust.
- Inject 2500 unit of heparin (0.5 mL) and flush sheath with saline to flush in remaining part of heparin in the sheath lumen.
- Take the desired catheter and start angiography (Fig. 7).

Puncture Technique

It is of two types:

1. Single wall puncture
2. Double wall puncture.

In single wall puncture technique, only the anterior wall of artery get punctured and in double wall both anterior as well as posterior wall get punctured. Single wall is safe in experienced hand and double wall is safe in inexperienced hand as chances of dissection of artery are high in single

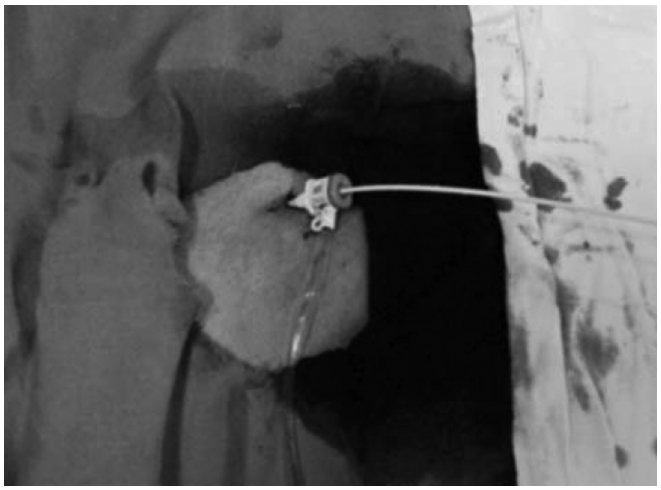

Fig. 7: Placement of arterial sheath

wall technique. In double wall technique, posterior wall hematoma is high, but can be affordable as compared to the dissection of the artery. Improper technique can lead to trauma of the vessel regardless of the type of needle used.

Seldinger Needle

This needle is comprised of three parts. Outer one is 16 G cannula. Middle one is a needle with a lumen inside. Stillete is inner most. The length of the needle is 7 cm. This is no longer used now. Recent needles consists of two parts; outer one is a cannula and inner one is thin needle.

Important Points to Remember

Check for free backflow of the blood in the catheter. Inject test amount 2–3 mL of contrast before taking run to check the exact position of the catheter and to check vascular spasm. Instruct the patient before every injection and inform the effect of the contrast like flushing and warm sensation or alteration in the taste, etc.

Postprocedural Management

Before removing the sheath, aspirate few mL of the blood to aspirate out any thrombus that could have formed during the procedure. If there is free backflow and if no clots are visible in the aspirate, the sheath can be safely removed. Compress the artery which is about 0.5 cm above the puncture site (for about 20 min). Compress the actual puncture site with middle finger, compress above it with index finger and below it with ring finger. Puncture site should be clearly visible during compression so that hematoma formation can be avoided. Do not obliterate the pulse, distal pulse should be faintly palpable. Apply steady moderate pressure for 15 minutes, reduce the pressure in next 5 min. Never remove compression abruptly. After compression feel all distal pulses. Bed rest with extended legs for next 8 hours, (patient may be allowed for leg roll). Check groin for hematoma formation. Monitor BP, pulse and neurological status of the patient. If patient is unable to pass urine then catheterize the patient until the patient is able to ambulate.

Types of Angiographic Catheters

- Pigtail catheter
- Head hunter catheter
- Cobra catheter
- Renal double curve catheter
- Multipurpose catheter
- Sims/Sidewinder
- Roberts uterine catheter.

PART 2: CEREBRAL ANGIOGRAPHIC ANATOMY

Arterial Anatomy

The brain is supplied by the two internal cerebral arteries, and two vertebral arteries which join to form the basilar artery. The basilar artery divides into two posterior cerebral arteries which along with posterior communicating arteries form the posterior part of circle of Willis. The anterior part of circle of Willis is constituted by both anterior cerebral arteries, anterior communicating artery and internal cerebral arteries.

The internal carotid artery (ICA) on each side enters the cranium by passing through the carotid canal in the petrous temporal bone (petrous segment). Petrous ICA give rise to tympanic branches as Vidian artery (artery of pterygoid canal) and caroticotympanic artery which supplies middle and internal ear and persistent stapedial artery. At times, the ICA courses posterolaterally than anteromedial (normal course) and present as pulsatile retrotympanic mass called as aberrant ICA. Knowledge of this variant is necessary to differentiate it from glomus tympanicum so that hazardous biopsy can be avoided.

The ICA exits from the carotid canal at the apex of the petrous bone and runs within the cavernous sinus to pierce the dura to enter the subarachnoid space adjacent to the anterior clinoid process. The cavernous ICA can be subdivided into ascending cavernous (C5). It starts from carotid canal to first posterior genu (C4). This segment can give rise to meningohypophyseal artery near junction of C5 and C4. Meningohypophyseal artery branches supply the posterior pituitary, cavernous sinus, clival dura and sometimes III to VI cranial nerves. The horizontal part (C3) extends between first posterior (C4) and second anterior genu (C2). After second genu (C2), rest of the cavernous ICA is called as C1 segment (Fig. 8). The inferolateral trunk arises from C4 segment and supplies the dura of the cavernous sinus and cranial nerves

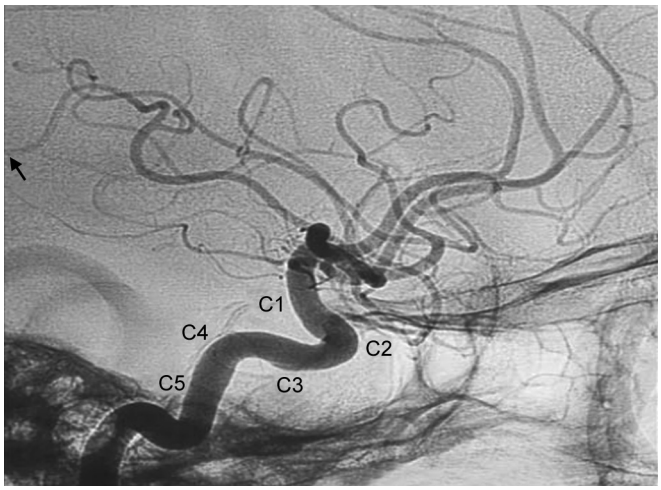

Fig. 8: ICA cavernous segments. C5 segment extends from carotid canal opening to first posterior genu (C4), horizontal segment (C3) extends between first posterior genu (C4) and second anterior genu (C2). Rest of cavernous ICA is called (C1)

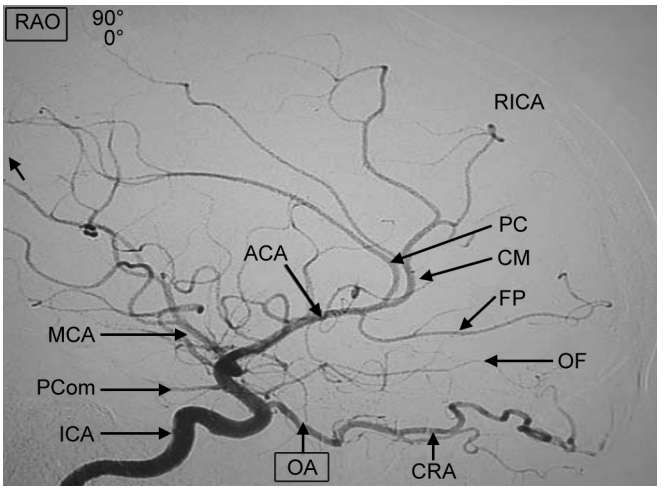

Fig. 9: Anterior circulation lateral view. Selective ICA angiogram lateral view showing different important branches (as annotated)
Abbreviations: ICA, internal carotid artery; OA, ophthalmic artery; CRA, central retinal artery; PCom, posterior communicating artery; MCA, middle cerebral artery; ACA, anterior cerebral artery; OF, orbitofrontal artery; FP, frontopolar artery; CM, callosomarginal artery; PC, pericallosal artery; RICA, right internal carotid artery

III, IV, V and VI. The superior hypophyseal trunk arises from supraclinoid ICA and supplies anterior pituitary. The ophthalmic artery arise from paraclinoid ICA (Fig. 9). The anterior choroidal artery arises from ICA just above PCom origin which arises posteromedially from supraclinoid ICA. The anterior choroidal artery supplies the choroid plexus of the lateral ventricles, medial temporal lobe and some striate branches to deep ganglionic structures (Fig. 10). The PCom runs posteriorly to join the posterior cerebral arteries (branches of basilar artery) to complete the circle of Willis. PCom supplies the deep ganglionic structures including the thalamus.

The anterior cerebral arteries proceed medially within the interhemispheric fissure separated by the falx. Both anterior cerebral arteries are connected by the anterior communicating artery in the midline completing the anterior part of circle of Willis (located in the suprasellar cistern).

Anterior cerebral artery (ACA) is thus divided into three segments. *Horizontal (A1) segment* which extends from the ACA origin to its junction with the anterior communicating artery (ACoA). The medial lenticulostriate arteries arise from A1 segment. *A2 segment* which extends from the junction of ACoA to its bifurcation into pericallosal and callosomarginal arteries. The orbitofrontal and frontopolar arteries arise from A2 segment. The recurrent artery of Heubner which is a lenticulostriate branch may arise from proximal A2 segment and less commonly from A1 segment.

A3 segment refers to the cortical branches that supply the anterior two-thirds of medial hemispheric surface and a small superior area over the convexities.

Middle cerebral artery (MCA) is also divided into three major segments. *Horizontal (M1) segment*: Extends from the origin of MCA to its bifurcation or trifurcation at sylvian

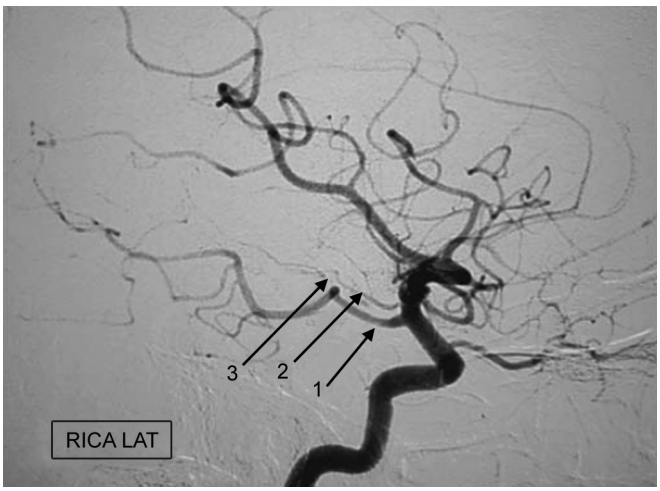

Fig. 10: Lateral ICA angiogram showing fetal PCA (1), anterior choroidal artery (2), and the plexal point (3), the point where artery enters the choroidal fissure
Abbreviations: RICA, right internal carotid artery; LAT, lateral

fissure. The lateral lenticulostriate arteries arise from M1 segment and supply the lentiform nucleus, parts of internal capsule and caudate nucleus. *Insular (M2) segment*: At its genu, the MCA divides into its insular (M2) branches, which loop over the insula and pass laterally to exit from sylvian fissure. *Opercular (M3) segment*: Which gives off branches that emerge from the sylvian fissure and ramify over the hemispheric surface. The insular and the opercular branches supply the temporal, parietal and variable parts of frontal and occipital lobes (Figs 11 and 12).

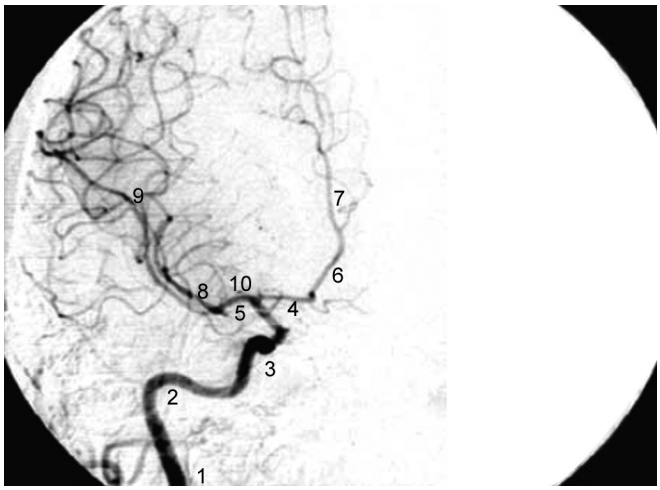

Fig. 11: Right internal carotid artery angiogram PA view. 1 = Cervical segment of ICA, 2 = Petrous segment of ICA, 3 = Cavernous segment of ICA, 4 = Anterior cerebral artery (A1), 5 = Middle cerebral artery (M1), 6 = Anterior cerebral artery (A2), 7 = Anterior cerebral artery (A3), 8 = Middle cerebral artery (M2), 9 = Middle cerebral artery (M3), 10 = Lenticulostriate arteries

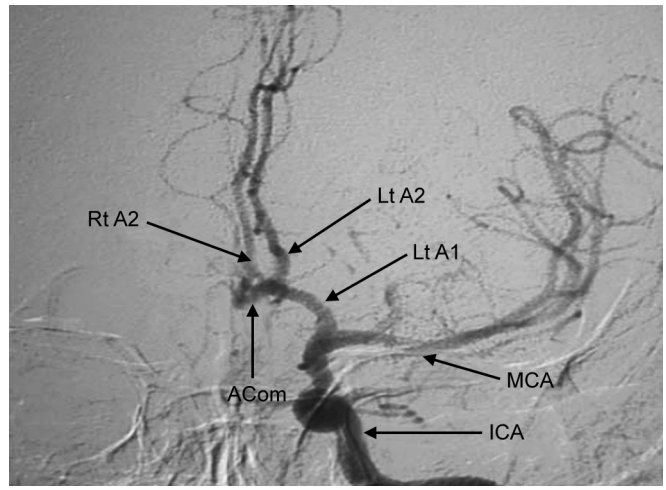

Fig. 12: Left ICA angiogram frontal view revealing ICA bifurcation, MCA, ACA segments and ACom (as annotated)

The two vertebral arteries (VA) arise from the respective subclavian arteries, course cephalad and enter the cranium through the foramen magnum. These unite in the posterior fossa, usually anterior to the medulla to form the basilar artery. Most of the time vertebral arteries are asymmetrical. In about 60% left vertebral artery is dominant, in 25% right can be dominant and in about 25% both vertebral artery can be symmetrical in size. Left vertebral artery can arise directly from aorta in small percentage.

The intracranial VA gives two major branches: Anterior spinal artery supplying the spinal cord and posterior inferior cerebellar artery (PICA) on each side which supplies choroid plexus of fourth ventricle, medulla, cerebellar tonsils, inferior vermis and parts of cerebellar hemispheres.

Basilar artery (BA) runs anterior to pons in the prepontine cistern and terminates in the interpeduncular cistern by dividing into posterior cerebral arteries (PCA). In prepontine cistern, it lies within the space marginated by lateral margin of clivus. Any further deviation from these boundaries are considered as dolichoectasia. In addition, the basilar artery gives off anterior inferior cerebellar artery (AICA) and superior cerebellar artery (SCA) on each side, just before bifurcation into posterior cerebral arteries. The anterior inferior cerebellar artery is the first major branch of basilar artery and most of the time (about 70%) arises as single vessel.

AICA courses posterolaterally within the CP angle cistern, whereas SCA curves around the pons and the midbrain just below the tentorial hiatus (Figs 13 and 14). The AICA supplies the VII, VIII CN, inferorlateral pons, middle cerebellar peduncle and anterolateral surface of cerebellum. The SCA supplies the entire superior surface of cerebellum, vermis, deep cerebellar white matter and dentate nuclei. In addition, BA also gives off multiple short and long segment circumflex perforating branches which supply the ventral pons and rostral brainstem.

The PCAs are usually terminal branches of basilar artery but they can arise directly from supraclinoid ICA with hypertrophy of PCom and hypoplasia of ipsilateral P1 segment of PCA called as fetal PCA (Fig. 10). Posterior cerebral artery (PCA) on each side is divided into three major segments. *Precommunicating (P1 or peduncular) segment*: It extends from the origin of PCA to its junction with the posterior communicating artery (PCoA). The posterior thalamoperforating arteries and medial posterior choroidal artery usually arise from P1 segment. *Ambient (P2) segment*: It courses around the midbrain above the trochlear nerve and tentorial incisura. The lateral posterior choroidal artery and thalamogeniculate arteries arise from the P2 segment.

Quadrigeminal (P3) segment: It runs behind the midbrain in the quadrigeminal plate cistern. The major branches of P3 segment are inferior temporal arteries, parieto-occipital artery, calcarine artery and posterior pericallosal arteries which supply the occipital lobe and posterior part of parietal lobe (Figs 13A and B).

Venous Anatomy (Fig. 14)

The cerebral venous system is composed of two components, the dural venous sinuses and the cerebral veins.

Dural Sinuses

Superior sagittal sinus (SSS): It is situated in the midline and typically originates near the crista galli anteriorly and extends posteriorly to its confluence with the straight and lateral sinuses at the torcula.

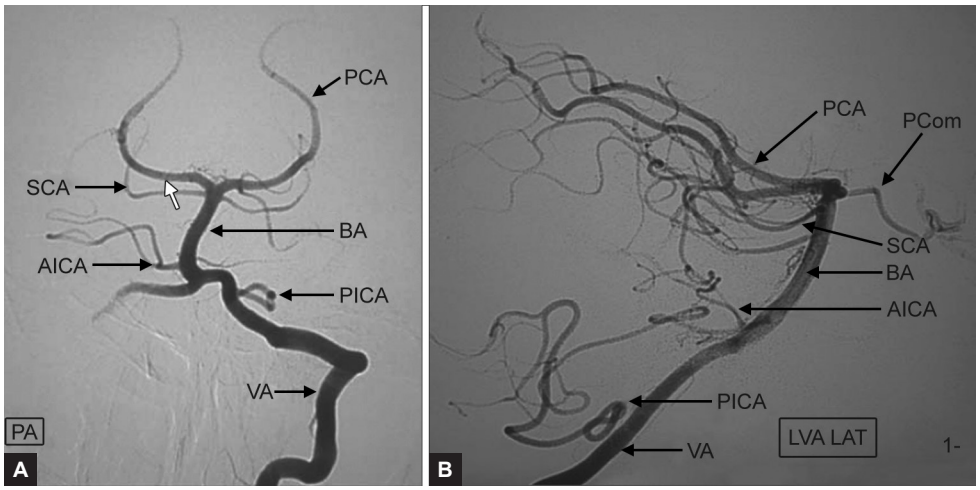

Figs 13A and B: Posterior circulation frontal and lateral view showing the major arteries and their branches.
Abbreviations: VA, vertebral artery; BA, basilar artery; PICA, posterior inferior cerebellar artery; AICA, anterior inferior cerebellar artery; SCA, superior cerebellar artery; PCA, posterior cerebral artery; PCom, posterior communicating artery; PA, pulmonary artery; LVA, left ventricular artery; LAT, lateral

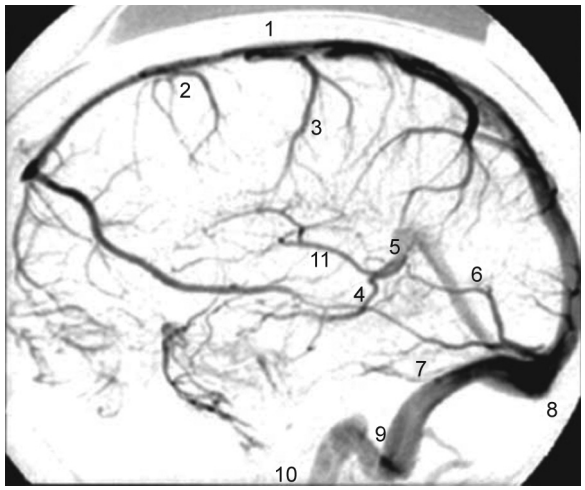

Fig. 14: Right internal carotid angiogram venous phase (lateral view). 1 = Superior sagittal sinus, 2 = Superior cerebral veins, 3 = Vein of Trolard, 4 = Basal vein of Rosenthal, 5 = Vein of Galen, 6 = Straight sinus, 7 = Transverse sinus, 8 = Torcular herophili, 9 = Sigmoid sinus, 10 = Internal jugular vein, 11 = Internal cerebral vein

Inferior sagittal sinus is situated in the inferior free margin of the falx cerebri and joins the vein of Galen to form the straight sinus.

Straight sinus courses backwards to unite with the SSS at the torcular herophili.

Transverse and occipital sinuses: The torcular herophili divides into the transverse (lateral) and occipital sinuses. The transverse sinuses course laterally around the tentorial attachment to form the sigmoid sinuses and drain into the internal jugular veins on either side. The occipital sinus is rudimentary.

Cavernous sinuses: The cavernous sinuses are the largest venous sinuses located in the parasellar region. Its major tributaries are superior and inferior ophthalmic veins. The ICA and 3rd, 4th, 6th, ophthalmic and maxillary divisions of 5th cranial nerves course within each sinus. Both cavernous sinuses communicate with each other, preclival venous plexus, sigmoid sinuses, and jugular bulb (through superior and inferior petrosal sinuses).

Cerebral Veins

These are divided into superficial (cortical) veins and deep veins.

Superficial cortical veins: These are variable in number and enter the SSS near the vertex. The larger veins which may be identified are superficial middle cerebral vein which runs along the sylvian fissure, vein of Trolard which courses from sylvian fissure to SSS and vein of Labbe which courses from sylvian fissure to the transverse sinus.

Deep cerebral veins: The medullary veins originate 1–2 cm below the cortex and course centrally towards subependymal veins which surround the lateral ventricles. The thalamostriate vein and septal vein join near the foramen of Monro to form the internal cerebral vein (ICV). The two ICVs and basal veins of Rosenthal (BVR) join to form the vein of Galen which runs under the splenium of corpus callosum and unites with the inferior sagittal sinus to form the straight sinus which join the SSS at the torcula.

The major veins draining the posterior fossa are anterior pontomesencephalic vein, precentral cerebellar vein, superior and inferior vermian veins and hemispheric veins.

4 CHAPTER

Advances in Computed Tomography Technology

Niranjan Khandelwal, Paramjeet Singh, Sameer Vyas

INTRODUCTION

Computed tomography (CT) technology has evolved from first generation scanners with a single detector to multidetector computed tomography (MDCT), dual source CT, flat panel CT and dynamic CT.[1-8] Better collimation of the X-ray beams, higher heat capacity of the newer X-ray tubes and increased sensitivity of detector assembly have significantly upgraded the technology. Introduction of spiral (helical) CT scans in 1990 which use slip ring technology allows continuous data acquisition of a volume by 360° gantry rotation during continuous table movement during the scan. The technique reduced slice thickness to submillimeter levels, allowed faster scanning and acquisition of a large volumetric data which can be used to generate thin slices and high resolution reformations of images in any desired plane from very thin isotropic voxels.

MULTIDETECTOR COMPUTED TOMOGRAPHY

The introduction of multidetector computed tomography (MDCT) system into clinical radiology has brought a revolution in the field of medical imaging. MDCT are the latest techniques where multiple rows of detectors are used to acquire multiple slices per rotation through interweaving helices (2, 4, 16 up to 320 slices). 1 mm × 20 mm detectors are replaced with arrays of 1 mm × 1.25 mm channels in MDCT which can be arranged in a symmetrical, adaptive or hybrid fashion. MDCT uses high gantry speed (0.5–0.8 seconds) allowing faster imaging and larger volume coverage particularly for CT angiography.[2,3]

This technology allowed the maturing of traditional CT from plain axial cross-section imaging to a modern real-like three-dimensional (3D) tool with identical spatial resolution along all directions allowing excellent multiplanar reformations and high quality 3D reconstructions. The scan parameters can be manipulated by changing the collimation, detector configuration and reconstruction algorithm.[3] Retrospective data analysis allows flexibility of examination. Simultaneous development of efficient computer systems made possible postprocessing and analysis of enormous data sets.

The two chief benefits of helical or multislice CT are an increase in the speed and defined ability of performance of volume acquisitions.

1. *Increased speed:* Multislice CT allows high-speed scanning, thinner sections or longer scan ranges. Increased scanning speed leads to less motion artifacts, especially in the cases of children and patients who are critically ill or are in trauma. Since scanning 0 is rapid, more volume can be covered and more data of higher resolution can be acquired for better 3D reconstructions. The contrast requirement is also less compared with standard CT or better images can be obtained with the same amounts of contrast material.
2. *Volume acquisition:* A continuous volume acquisition in a helical CT makes sure that none of the lesions go as miss when a patient respirates or makes a movement. These improved 3D capabilities of multiplanar reformations and exhaustive 3D representations are the prime benefits for volume acquisition. This technology provides best result if the thickness of the chosen section is reduced to the minimum. The utility of volume rendering techniques has risen so much that interpretation of images has progressed from observation of aerial sections to evaluation of real 3D data sets.

DUAL SOURCE COMPUTED TOMOGRAPHY

Dual source CT uses two separate X-ray sources of different energies to enhance the contrast between adjacent structures and their respective detector sets which are placed orthogonal to one another.[4,5] It provides high temporal resolution and enables bone removed CT neuroangiographic images of diagnostic quality. In addition, calcified plaques and surgical clips can be removed by processing the data. Recent studies have reported contrast-enhanced dual-energy CT angiography had high diagnostic accuracy for

the detection of intracranial aneurysm as compared with 3D digital subtraction angiography (DSA) at a lower radiation dose.[5]

FLAT-PANEL VOLUME COMPUTED TOMOGRAPHY

Flat-panel volume computed tomography is recent development in the CT technology that allows coverage of a large volume per rotation, fluoroscopic and dynamic imaging, and high spatial resolution.[6] It represents combining of different modalities like radiography, fluoroscopy, X-ray angiography, and volumetric CT into one system. Area detectors have replaced the detector rows in this new technology. The flat-panel detector with its wide Z-axis coverage makes the imaging of entire organs possible in a single axial acquisition. Its fluoroscopic and angiographic capabilities permit intraoperative and vascular applications. The flat-panel volume CT is advantageous in comparison to multidetector CT as it allows ultra-high spatial resolution, real-time fluoroscopy, dynamic imaging capabilities, and whole-organ coverage in one rotation.[6] The main limitations of flat-panel volume CT is that it requires a higher radiation dose [needed to achieve a comparable signal-to-noise ratio (SNR)], lower contrast resolution, and a slower scintillator that slows down the scanning process.

DYNAMIC COMPUTED TOMOGRAPHY ANGIOGRAPHY

Inability to provide any dynamic (i.e. temporal resolved) information was a major limitation of MDCT compared to the gold standard of angiographic, digital subtraction angiography. But this limitation seems to be resolved with the recent introduction of a 320-detector row CT scanner that provides the possibility of dynamic volume scanning (four-dimensional scanning with the fourth dimension being the time).[7,8] Volumetric CT using 320 detector rows enables full brain coverage in a single rotation that allows for combined time-resolved whole-brain perfusion and four-dimensional computed tomography angiography (CTA). Its potential applications in neuroradiology are in stroke, steno-occlusive disease, arteriovenous malformations and dural shunts. The broad coverage enabled by it offers Z-axis coverage allowing for whole-brain perfusion and subtracted dynamic angiography of the entire intracranial circulation. It has the potential of scanning entire organs such as the heart and brain in a single rotation as it provides large maximum detector area that can be used for this scanner, therefore allowing the visualization of dynamic flow and perfusion, as well as motion of an entire volume at very short time interval.

COMPUTED TOMOGRAPHY IN NEUROIMAGING

Computed tomography scan has been the workhorse of neuroimaging. It is a cost-effective and quick screening test with established role in cross-sectional imaging of craniospinal trauma, subarachnoid hemorrhage, stroke, evaluation of postoperative patients as well as of bone and detection of calcifications in brain lesions. In addition, it has a role in those patients in which MRI is contraindicated. The concept of CT imaging was challenged with the advent of MRI; however, with multislice the modality has seen a new resurgence. Many of these CT applications are current standards in clinical practice.

Computed tomography angiography now plays an expanded role in evaluation of subarachnoid hemorrhage by detecting vascular lesions like aneurysms and arteriovenous malformations. These patients are already on the CT table and it only requires a few more minutes to obtain detailed information about possible causes of the hemorrhage. By now, there are an increasing number of surgeons who are willing to operate solely on the basis of a CTA exam. With MDCT, spatial resolution is excellent and the results are similar or even superior to angiography.

There is an increasing use of the modality in imaging of stroke through CTA of intracranial and neck vessels, venography and CT perfusion imaging. The excellent reconstructions of CT data have also enhanced the utility of CT in neuroimaging, i.e. in spinal trauma and evaluation of craniovertebral junction.

NONCONTRAST COMPUTED TOMOGRAPHY OF HEAD

Helical CT has not caught on for routine imaging of the neurocranium and axial mode is still used for routine imaging; however, thin-sections obtained on multichannel scans have distinct advantage. Thin sections of the middle cranial and posterior fossa reduce the beam hardening artifacts and improve delineation of the brain stem and temporal lobe. A usual spiral protocol is 5 mm acquisition with a table speed of 15–30 mm/s for brain. Thin sections (i.e. 1.5 mm) can be merged into thicker (2.5 mm or more) thus reducing noise and radiation dose. The data may be split back for high resolution reconstructions. Thus, there is now the option of not only axial but also coronal or sagittal images of the brain. The clinical usefulness of this technique, however, has not yet been tested. The technology has affected pediatric neuro applications in many ways. Increased speed has eliminated the need for sedation and a reconstruction of data obtained in least provocative position allows multiplanar depiction of anatomy.

Computed Tomography Angiography

Catheter angiography; the gold standard for diagnostic neuroangiography, is an expensive and invasive procedure with a morbidity and mortality of 1.5–2%. Accurate imaging of vascular anatomy of head and neck requires excellent spatial resolution for visualization of small and tortuous vessels. In addition speed is needed to avoid venous enhancement. CTA of the intracranial or cervical vessels thus has strikingly benefits from the technology of MDCT. At submillimeter collimation (0.5–0.75), the entire length of the carotids or the cerebral arteries is scanned in a few seconds in pure arterial phase. Finest anatomic detail can be achieved by this isotropic data set providing high quality 2D and 3D renderings of vascular anatomy through different reconstruction techniques, such as multiplanar reconstruction (MPR), surface-shaded display (SSD) or volume-rendering technique (VRT).[9-12]

Magnetic resonance angiography (MRA) and color Doppler ultrasound (DUS) are some noninvasive alternatives. The limitations of MRA include motion artifacts, long examination times, loss of signal due to turbulence and in plane saturation leading to exaggeration of stenosis, poor demonstration of calcium and bony landmarks and limitations in evaluating postoperative patients with metallic clips and stents. With recent advances in MR technology [contrast enhanced magnetic resonance angiography (CE MRA)], some of these have been overcome. Color Doppler (CD) is operator-dependent and limited in evaluating the intracranial vasculature.

Computed tomography angiography the current noninvasive modality of choice for neuroangiography, overcomes many of the disadvantages of MRA. It is faster, available in smaller centers, cheaper, sensitive to presence of calcium, displays bony landmarks and can be used in patients with aneurysm clips and other MR incompatible metallic hardware. CTA depends on volume expansion and opacification of blood in the vessel and hence more accurate. Drawbacks of CTA are the use of intravenous contrast and radiation exposure.

Technique

Computed tomography angiography evaluates the area from arch of aorta to vertex for cervicocerebral study in one sitting or from C1 to vertex for cerebral angiogram in 15–20 seconds. Typical parameters can be as follows: 120–140 kVp, 200–350 mAs, 1.25 mm cuts with 1 mm overlap, a pitch of 3 for head (1.25 mm/3.75 mm/rev) and 6 (1.25 mm/7.5 mm/rev) for neck and 0.5 second rotation time. 100 mL of contrast is injected at a rate of 4 mL/s by a power injector which can be chased by bolus tracking. When a threshold attenuation of 100 HU is reached as detected by the ROI placed in one of the common carotids, the scan starts automatically. Alternatively, a test bolus method (20 mL), using a single axial section dynamic study at C5 level can be used. An arbitrary delay of 15–20 seconds is also adequate for CTA of brain. A rapid intravenous injection of nonionic contrast, preferably from right hand, via pressure injector with flow rate of at least 3 mL/s achieves a luminal density of 150 HU which is considered to give best results. Higher rates do not offer any significant advantage.[13] The images are reformatted with section thickness of 1.25 mm and overlap of 1 mm at a narrow field of view (120 mm).

Image Processing

The display technique consists of multiplanar reconstructions (MPR), maximum intensity projection (MIP), shaded-surface display (SSD) and volume-rendering technique (VRT). MPR allows for viewing of the raw data in any desired plane along the course of the vessel and is good for relatively straight vessels such as the carotid arteries but is not very effective for vascular anatomies which are complex like circle of Willis. MIP images are obtained by projection of imaginary rays through the image data and mapping the maximum attenuation values. The attenuation value, i.e. vessel lumen, calcium and thrombus are well delineated but depth information is totally lost. The degree of stenosis is calculated accurately but there may be overlapping of vessels with bone. Surface shaded display computes all surface connecting neighboring pixels above a particular threshold. Unlike MIP it preserves depth information (displays complex anatomic relationship in region of vessel overlap) but loses attenuation information. It does not show interiors of the vessels, thrombus and wall calcification and as underestimates stenosis. Volume rendering allows integration of all available information through most advanced 3D rendering algorithm. An opacity as well as color is assigned to all the voxels available and VR incorporates all the relevant data into the final resulting image. It overcomes many of the problems seen with MIP and SSD. Since some data loss is inherent with all postprocessing techniques, raw images should be analyzed in all cases.

APPLICATIONS

Extracranial Vasculature

Carotid Artery Stenosis

The detection and accurate quantification of carotid artery stenosis is important for appropriate treatment since carotid endarterectomy has a clear benefit in symptomatic patients with high grade stenosis (70–99%) [North American Symptomatic Carotid Endarterectomy Trial (NASCET)].[14] The gold standard of carotid evaluation has been conventional angiography but the risks associated with it, interobserver variability in interpreting stenosis (up to 7%), a tendency to overestimate stenosis (6%) and limited number of views are some of the limitations.[15] CTA can provide infinite views

for accurate estimation of eccentric or irregular stenosis, delineates mural calcium from luminal contrast and prevents inaccuracy in grading stenosis. Magnified axial images with a window setting half way between luminal contrast and wall are considered best to evaluate stenosis followed by MIP and SSD.[16] Length of thickness, thickness of slices presence of calcification and direction of vessel in the imaged volume also affect measurements.[17-19]

It is difficult to assess exact accuracy of CTA in carotid stenosis due to different criteria and parameters used on different machines; however, reported sensitivity for severe stenosis and occlusion has ranged from 88–100%, which correlates well with conventional angiography (Figs 1A to D). Lee et al. reported 100% accuracy for occlusion, 90% for critical stenosis (90–99%), greater than 95% for severe stenosis (70–89%), greater than 85% for moderate stenosis (50–69%) and 95% for minimal stenosis.[17-19] CTA also has a good correlation of plaque morphology (calcified, soft or ulcerated).

Computed tomography angiography has a higher accuracy compared to DUS and is comparable or slightly better than CE MRA (100% vs 93%) for assessing high-grade stenosis and distinguishing it from complete occlusion.[18] This is crucial, as high-grade stenosis is an indication for carotid endarterectomy whereas complete occlusion is a contraindication to surgery. CTA also provides assessment of the brain parenchyma at the same time.

Dissections

Dissection of carotid or vertebral artery is an increasingly recognized cause of stroke in young is adequately evaluated with CTA and results are comparable to other noninvasive techniques like MRA and CD.[20] Subadventitial dissections, presence of intramural hematoma, stenosis, occlusions and pseudoaneurysms can be picked up.

Computed tomography angiography is not successful for hemodynamic of blood flow. MDCT can simultaneously evaluate the intracranial vasculature for tandem stenosis in same sitting. Polytrauma patients with a high index of vascular injury can also be evaluated by CTA. Helical CT provides simultaneous assessment of vascular, soft tissue and vertebral injury in this setting.

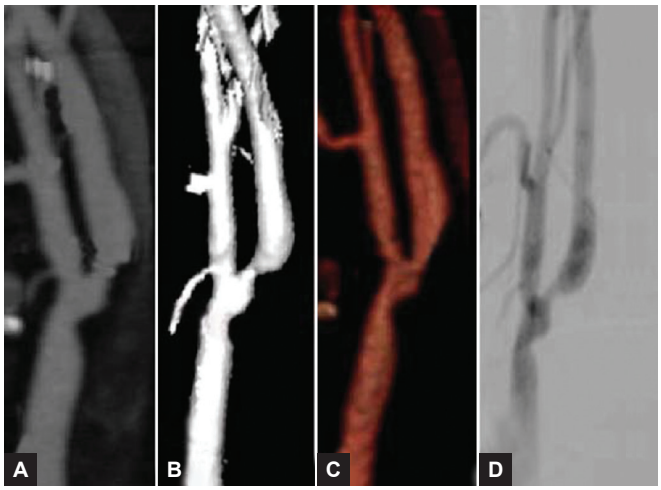

Figs 1A to D: Left common and internal carotid artery stenosis. (A) MIP; (B) SSD; (C) VR and (D) DSA images showing moderate stenosis of distal common carotid and proximal internal carotid artery. The stenosis is not complete

Intracranial Vasculature

Aneurysms

Digital subtraction angiography is the gold standard for the evaluation of patients with subarachnoid hemorrhage secondary to suspected aneurysmal rupture, but it is time consuming, invasive and carries a less than 0.1% complication rate of permanent neurological deficit.[13] There is an associated increased risk of rebleed.

As shown by some clinical studies, CTA seems suitable in the acute stage after subarachnoid hemorrhage (SAH) as it does not require intra-arterial catheterization, uses short scan times and can immediately follow the initial unenhanced CT examination.[21]

A recent study found CTA to detect 90% of all aneurysms associated with acute SAH and neurosurgeons assessed CTA as equal or superior to DSA in 83% of cases. In 74% of patients, surgery might have been based on CTA findings alone.[21] The reported sensitivity of CT angiography lies in the range of 80–97% depending on the size and location of an aneurysm.[22] Sensitivity is highest for aneurysms more than 5 mm in size, however, those less than 5 mm in size can be detected with a sensitivity of only about 20%.[23] For diagnosed aneurysms, CTA provides a more detailed analysis of the sack morphology, neck, parent vessel caliber and its spatial relationship with aneurysm, additional vascular relationships and surrounding anatomy (bony and soft tissue landmarks) which helps in finding the appropriate options for treatment (surgical or minimally invasive endovascular) (Figs 2 to 4).

Computed tomography angiography is also a problem-solving modality in poorly defined aneurysms on DSA and particularly useful for evaluation of paraclinoid aneurysms for their anatomically complex relationships with bony and vascular structures (Figs 2A to D). CTA is significant in the characterization of giant aneurysms preceding surgical or endovascular treatment and helps in the detection of pseudoaneurysms. CTA is also indicated in the assessment of postoperative/postintervention status of aneurysm.

Though conventional angiography is more sensitive for small aneurysms, CTA may show small thrombosed aneurysms not shown on DSA.[24] CTA can be very efficient for screening of vasospasm following SAH. It can be a screening technique to detect aneurysms in high-risk group patients

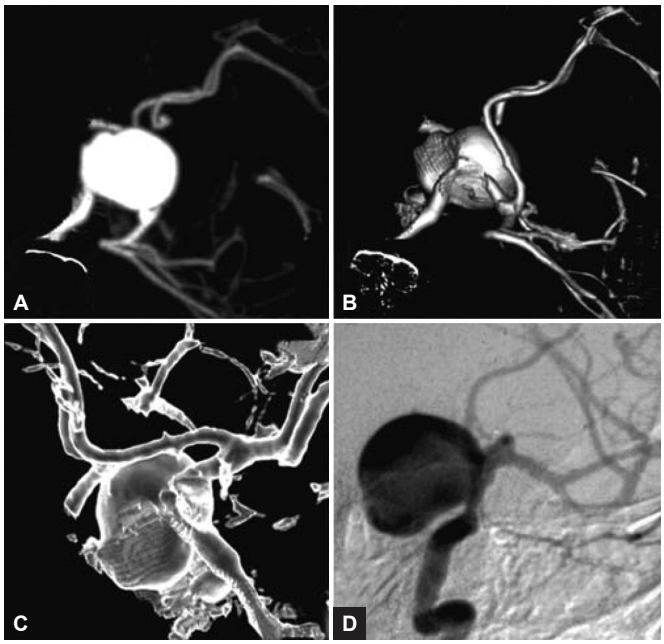

Figs 2A to D: A giant carotico-ophthalmic aneurysm. Maximum intensity projection (A), volume-rendering (B and C) images; and digital subtraction angiography (D). The carotid artery is incorporated into the aneurysm. Post processing shows vascular relationship better than DSA

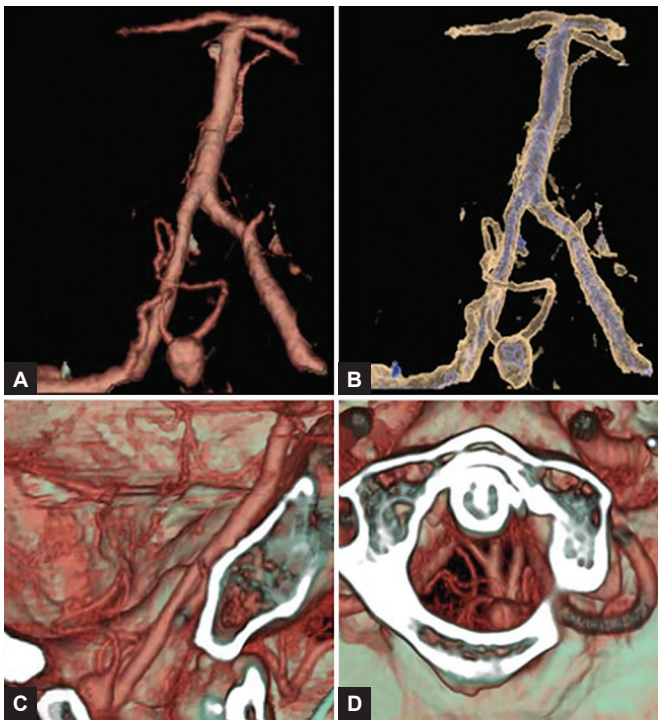

Figs 3A to D: Posterior inferior cerebellar artery (PICA) aneurysm: volume-rendering images (A and B) posterior view showing the aneurysm arising from the left PICA. The relationship with C1 posterior arch was clearly shown (C and D) helping the decision for surgical approach

such as those with strong family histories, though MRA is currently the modality of choice.

Computed tomography angiography and MRA have been found to be generally equivalent in their ability to detect and characterize aneurysms (>5 mm).[25] CTA however, is superior to MRA, as turbulent flow or slow flow may cause artifactual loss of signal in MRA. CE MRA may circumvent some of these disadvantages. MRI and MRA are currently the noninvasive modality of choice for screening patients in the high-risk group for aneurysms and following up incidentally detected aneurysms being managed conservatively.

Some drawbacks of CT angiography include bleak visibility of small arteries, difficulty in distinguishing the infundibular dilatation at the origin of an artery from an aneurysm, the kissing vessel artifact, display of venous structures that can simulate aneurysms, inability to identify thrombosis and calcification on three-dimensional images, and beam-hardening artifacts produced by aneurysm clips.

Arteriovenous Malformations

Computed tomography angiography though has limited role in intracranial arteriovenous malformations (AVMs), it can visualize the feeding arteries, nidus and draining veins but

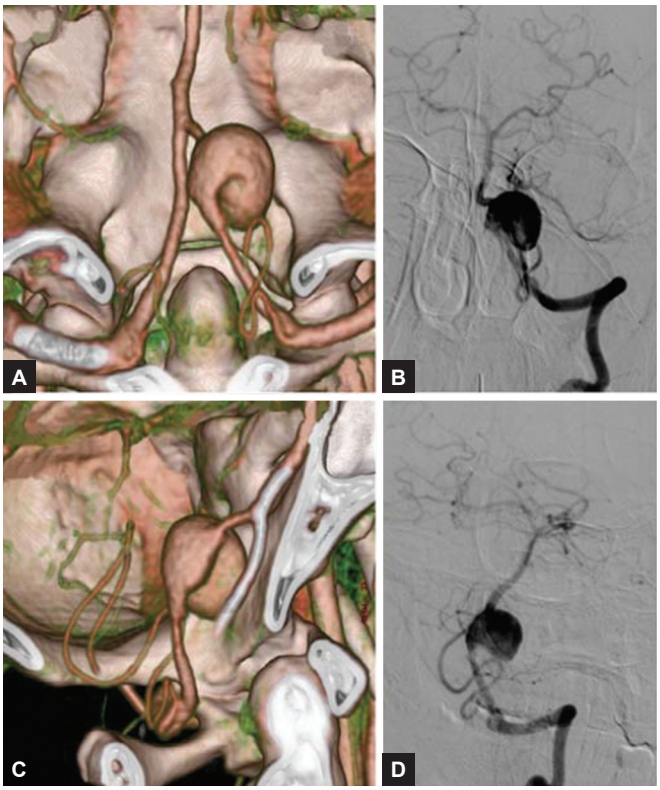

Figs 4A to D: Left vertebral artery aneurysm: Volume-rendering (A and C) and digital subtraction angiography (B and D) showing left vertebral artery aneurysm with complex configuration better shown on computed tomography volume-rendering images

optimal temporal information regarding arterial and venous phases may not be adequate as compared to DSA.[26] CTA does not possess a high spatial resolution which is required for detecting associated aneurysm, stenosis and small feeding vessels provided by conventional angiography. The major use of CTA today is in the evaluation of the AVM nidus during radiosurgery planning and post-treatment follow-up.[27]

Though any study has not yet compared the roles of CTA and MRA in AVMs yet each modality appears to have its own advantages and disadvantages but flow encoded MR may provide more information in AVM. Embolization material can interfere with delineation of vasculature on MRA but usually is not a problem with CTA.

Tumors

Computed tomography angiography can demonstrate vascular encasement by skull-base tumors. It also provides preoperative assessment of the 3D bony and vascular anatomy prior to tumor excision. Computed tomography venography (CTV) is also useful for showing venous invasion by meningioma.

Computed Tomography Perfusion

It has been shown that cerebral blood volume when falls below 20 mL/100 g/min synaptic transmission in neurons fails and below 10 mL irreversible cell death occurs. Therefore tissue salvage is possible in areas with lesser degrees of compromise of blood flow. Computed tomography perfusion (CTP) is a rapid means to evaluate cerebral perfusion as there is a linear relationship between the contrast agent concentration and attenuation.[28-34] CTP is based on the central volume principle as per the equation: CBF = CBV/MTT [cerebral blood flow (CBF), cerebral blood volume (CBV), mean transit time (MTT)]. During the first pass of a bolus of contrast, there is a transient increase in attenuation proportional to the concentration of the agent in a given region. Contrast agent-time concentration curves are generated in an arterial and venous region of interest (ROI) (i.e. middle cerebral artery and superior sagittal sinus) and in the area of perfusion abnormality. Deconvolution of this data gives the MTT. Cerebral blood volume (CBV) is calculated as the area under the curve of parenchymal pixel and the arterial ROI. From this CBF can be calculated.[28]

Technique

Four adjacent 5 mm slices are selected starting at the level of basal ganglia. About 50 mL of a nonionic contrast is injected at a rate of 3 mL/s. Five seconds later a continuous scan is initiated using 80 kVp, 190–200 mA at one second rotation for 50 seconds. The perfusion data is analyzed at a work station to generate color coded CBF, CBV and MTT maps.

With the advent of 256 and 320 MDCT, whole brain perfusion CT can be performed which provides access to the entire brain with the administration of one contrast medium bolus so that ischemic region can be identified. I can improve the diagnostic utility in neuroimaging.[33-34]

CLINICAL APPLICATIONS

Acute Stroke

The goal is to identify potentially salvageable tissue for thrombolytic therapy. In a retrospective study, Eastwood et al. found significant difference in CBV, CBF and MTT in symptomatic hemisphere of which MTT was the best indicator for stroke.[30] A 35% decrease in CBF had a good correlation with ischemic penumbra in another study.[30] Early studies do indicate that CTP may enable predication of patients who would benefit from therapy and determine final infarct size.

Cerebrovascular reserve: In patients with chronic ischemia related to underlying stenotic lesions, the involved territory is maximally vasodilated due to autoregulation and cannot respond to acetazolamide challenge. An increase of 5% in CBF indicates insufficiency and a decrease in CBF indicates higher risk of stroke. CTP has been used to show low CBV and CBF in patients of SAH with moderate-to-severe vasospasm.[31,32]

Tumors

Many studies has shown that modified CTP technique has high permeability surface product (a measure of microvascular permeability) in tumors and may prove advantageous over MR in tumor perfusion studies. CTP can be used for preoperative grading of gliomas and can provide additional information about tumor hemodynamics.[33,34] In addition, perfusion computed tomography (PCT) maps are also useful for surgical biopsy and/or radiosurgery guidance to target the areas of increased CBV which can yield better histology and better response to treatment.

Computed Tomography Imaging of Acute Ischemic Stroke

Several studies have shown better neurological outcome in patients with acute stroke with thrombolytic therapy which were based on the imaging criteria. Multimodal CT (noncontrast CT, CT Angiography and perfusion CT) allows the assessment of the four Ps (parenchyma, pipes perfusion, and penumbra).[35-40] MDCT provides a 'one-stop-shop' approach for comprehensive noninvasive assessment of acute stroke patients by demonstrating the site of arterial occlusion and hemodynamic status of the brain parenchyma. A non-contrast scan is done to diagnose infarct, determine its extension and rule out hemorrhage. A CTA is an accurate

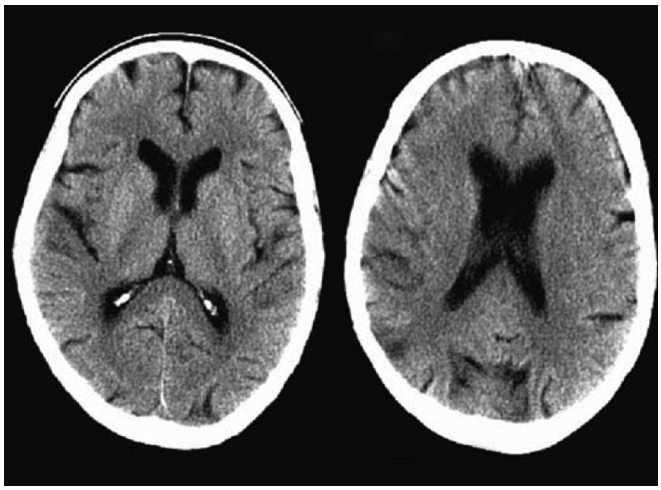

Fig. 5A: Noncontrast CT within 2 hours of stroke showing ill-defined hypodensity in the right parietotemporal region

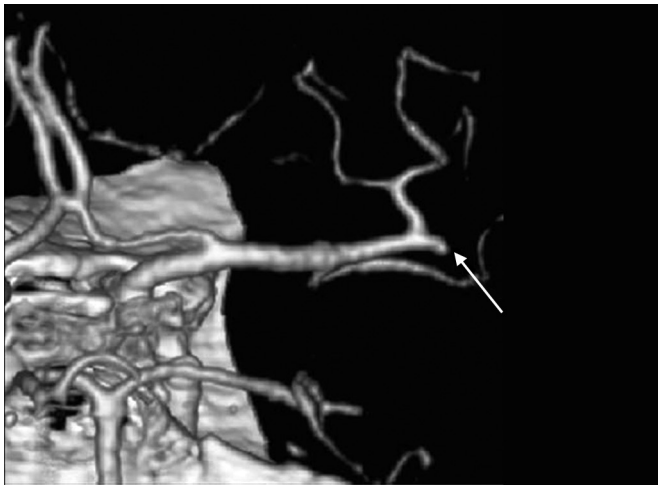

Fig. 5B: Computed tomography angiography in posterosuperior view showing complete occlusion of the inferior division of the right middle cerebral artery (MCA) (arrow)

technique for evaluation of vascular patency in acute stroke by allowing comprehensive evaluation of the intra- and extracranial vasculature. A CTA from the aortic arch to the intracerebral vessels helps to detect carotid plaques as possible causes of the event, distinguishes between proximal and distal occlusions of an intracranial artery, differentiates arterial from venous infarct and provides information about hypoperfusion and collateralization of blood flow. Finally, a CT perfusion scan distinguishes between penumbra of hypoperfused and umbra of nonperfused tissue in order to select patients who would benefit from thrombolytic therapy. The above information provides a rational basis on which to choose the optimal treatment for patients with acute stroke[39] (Figs 5A to C). Due to limited availability of PET, SPECT and Xenon CT, CT and MR perfusion are the two practical

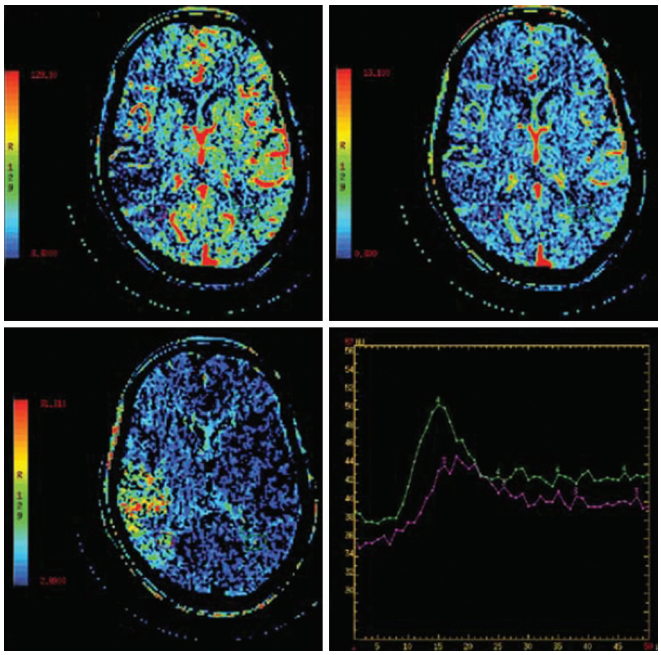

Fig. 5C: Cerebral blood flow, cerebral blood volume and mean transit time maps showing perfusion defect and a large ischemic penumbra. MTT maps shows delayed transit of contrast. Time attenuation curve of penumbra region showing less attenuation compared to normal side

choices. MRI imaging with DWI and PWI is equally powerful alternative and both CT and MR techniques are comparable in evaluating the tissue at risk in acute stroke according to a recent study.[40] However, widespread availability of CT in smaller centers is a big advantage.

Computed Tomography Venography

Computed tomography venography allows visualization of the cerebral venous structures and has high sensitivity for depicting the cerebral veins and sinus compared to DSA.[41-43] MDCT venography is a fast, widely accessible, and cost-effective method for evaluating cerebral sinuses in emergency setting. Dural sinus thrombosis is difficult to diagnose clinically due to varied clinical presentation. The most commonly affected sinuses are the superior sagittal sinus, the transverse sinus and the sigmoid sinus. On CTV, a thrombosed dural sinus is seen as a filling defect and is often associated with contrast enhancement of the walls of the dural sinus as well as abnormal collateral venous drainage and tentorial enhancement (Figs 6A to E). MR venography (MRV) is currently the technique of choice for diagnostic evaluation and follow-up for patient with cerebral sinovenous thrombosis. Studies have shown CTV as comparable to accuracy of MRV in the diagnosis of dural sinovenous thrombosis.[41-43] CT venography overcomes flow-related artifacts (differentiates slow flow from thrombosis) seen on time-of-flight (TOF) MR, takes less time and also

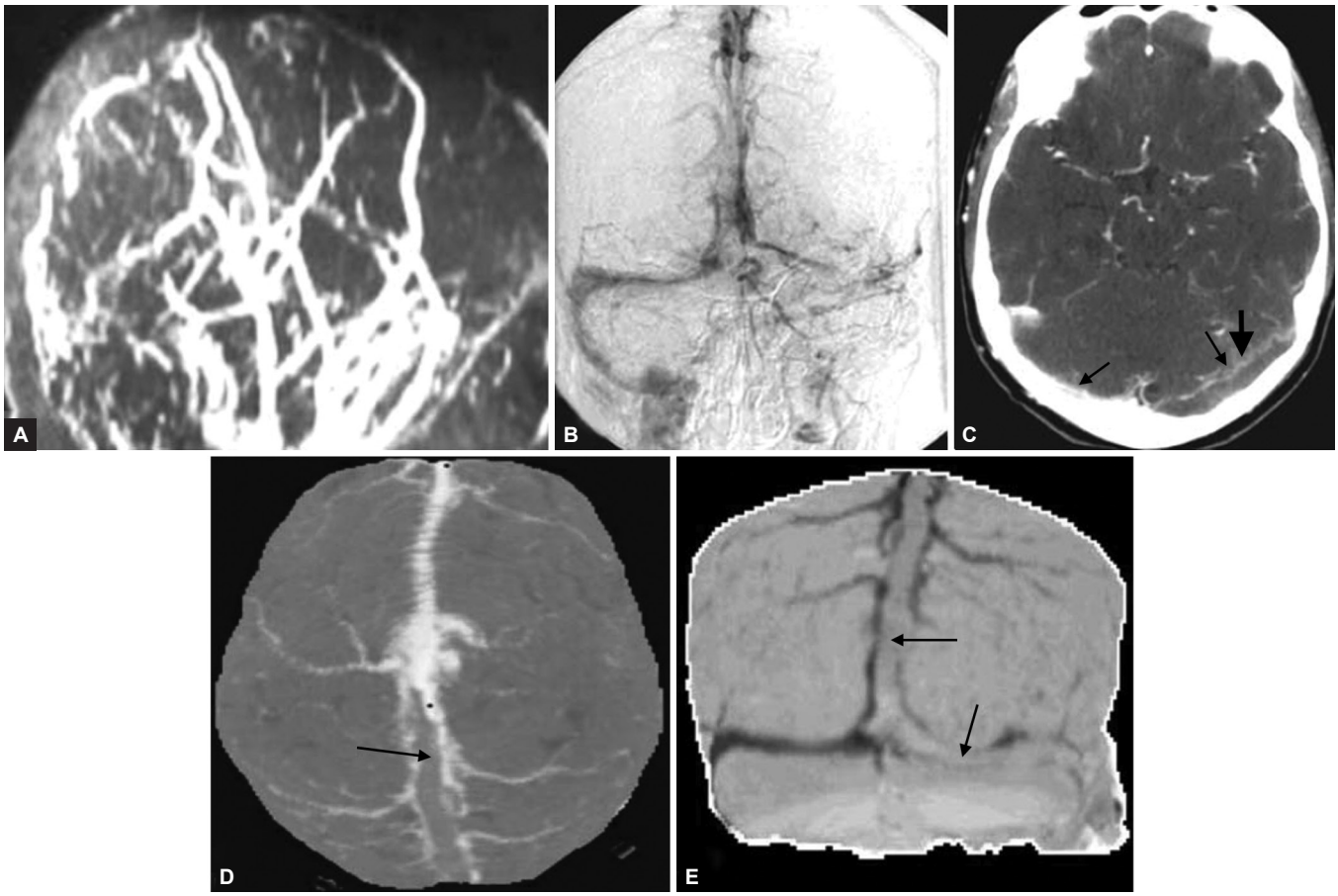

Figs 6A to E: Magnetic resonance angiography (A) and venous phase of DSA (B) show thrombosis of superior sagittal sinus and left transverse sinuses. Base image of CTV (C) shows thrombus in the left transverse sinus (double arrows). CTV (D and E) superior and anteroposterior views showing thrombus within the sinus

helps in distinction of tumors that compress dural sinuses, from those which occlude them. However, CT needs contrast administration and lacks sensitivity of MR in showing venous infarction of brain. Overall, CTV is a reliable alternative to MRV in case MR is contraindicated in such patients or is not diagnostic.

Technique

Computed tomography venography is performed using 100 mL of intravenous contrast injected at the rate of 3 mL/s with power injector. After a scan delay of 40 seconds, 1 mm collimated sections with a pitch of 2:1 are done covering the skull.

MULTIDETECTOR COMPUTED TOMOGRAPHY OF SPINE

Multidetector CT has been a major advancement in imaging of trauma patients to facilitate rapid diagnosis before the patient can be shifted to operation theater. Bony abnormalities are depicted better with MDCT when compared to single slice CT. Current scanners with 16 or more detectors are used to scan from head to below hips using whole body single pass technique. Imaging metallic hardware, which was impossible due to streak artifacts in the single slice helical CT scanning can now be assessed easily with MDCT due to increase in the of detector rows.[44] With improvement of isotropic resolutions, multi-planer reformations now enable diagnosis that are not so apparent on axial images, i.e. transverse fractures and fusions. Understanding of complex spatial relationships of bone becomes easier which translates into increased confidence level of the radiologist. While 3D-CT may not add to diagnostic information achieved by use of 2D reformatted image but it does aid the surgeons to plan reconstructive surgery.

CLINICAL APPLICATIONS

- *Trauma:*
  - *Cervical trauma:* CT is cost effective in patients with closed head injury with high risk of associated